Direct and Inverse Problems of Network Analysis

Dissertation zur Erlangung des akademischen Grades
Dr. rer. nat.

vorgelegt von

Erik Gengel

Institute für Physik and Astronomie,
Mathematisch-Naturwissenschaftliche Fakultät
Universität of Potsdam

1.	Gutachter:	apl. Prof. Dr. Michael Rosenblum	Universität Potsdam
2.	Gutachter:	apl. Prof. Dr. Ulrich Parlitz	Universität Göttingen
3.	Gutachter:	Prof. Dr. Arkady Pikovsky	Universität Potsdam

Dedicated to **My Grandmother**

Aufersteh'n, ja aufersteh'n wirst du,
mein Staub, nach kurzer Ruh!
Unsterblich Leben! Unsterblich Leben
wird, der dich rief, dir geben!

Wieder aufzublüh'n, wirst du gesäht!
Der Herr der Ernte geht
und sammelt Garben
uns ein, die starben!

O glaube, mein Herz! O glaube:
Es geht dir nichts verlohren!
Dein, ist, ja Dein, was du gesehnt!
Dein, was du geliebt, was du gestritten!

O glaube: Du wardst nicht
umsonst gebohren!
Hast nicht umsonst gelebt, gelitten!

Was entstanden ist, das muss vergehen!
Was vergangen, auferstehen!

Hör' auf zu beben!
Bereite dich zu leben!

O Schmerz! Du Alldurchdringer!
Dir bin ich entrungen!
O Tod! Du Allbezwinger!
Nun bist du bezwungen!

Mit Flügeln, die ich mir errungen,
in heißem Liebesstreben
werd' ich entschweben zum Licht, zu dem
kein Aug' gedrungen!

Mit Flügeln, die ich mir errungen,
werde ich entschweben!
Sterben werd' ich um zu leben!
Sterben werd' ich um zu leben!

Aufersteh'n, ja aufersteh'n wirst du,
mein Herz in einem Nu!
Was du geschlagen, Was du geschlagen -
Zu Gott- zu Gott- zu Gott wird es dich
tragen!

Last and final conclusion of the symphony no. 2 in C minor *Resurection* composed by:
Gustav Mahler
Text:
Friedrich Gottlieb Klopstock and
Gustav Mahler

Statement of financial support

These doctoral studies acknowledged support from the grant for doctoral studies of the Friedrich-Ebert-Stiftung from 1st of October 2017 to 1st of October 2020. The Friedrich-Ebert-Stiftung resides among the most influential societal think tanks worldwide. Once founded in 1925 according to the last will of the first president of democratic Germany, Friedrich Ebert, the foundation nowadays is engaged in numerous educational and cultural projects together with other democratic institutions and supports a widespread community of students and young researchers.

The preparation of this monograph and concluding works were supported by a scholarship of the Potsdam Graduate School from 1st of October 2020 to 31st of March 2021.

Statement of authorship

English: I hereby declare that the given dissertation is a sole product of my personal and scientific work. External literature and scientific results of third parties are marked and cited throughout the text and word-for-word passages are marked. Personal scientific publications which contribute significantly to the content of chapters are explicitly mentioned in the beginning of these chapters. I hereby also declare that the given dissertation and the concluding results of my doctoral studies have neither been submitted to an other university nor have they been published in this or a similar form.

Deutsch: Hiermit erkläre ich, dass die vorgelegte Dissertation das alleinige Produkt meiner persönlichen und wissenschaftlichen Arbeit ist. Externe Quellen und wissenschaftliche Resultate Dritter werden in der gesamten Dissertation gekennzeichnet. Eigene wissenschaftliche Publikationen, welche signifikant zum Inhalt von Kapiteln beitragen, werden zu Beginn dieser Kapitel explizit benannt. Ich erkläre hiermit weiterhin, dass die vorliegende Dissertation und die zusammenfassenden Resultate meiner Tätigkeiten im Promotionsstudium weder an einer anderen Universität eingereich, noch in dieser oder einer ähnlichen Form bereits publiziert wurden.

Erik Gengel, Seebad Heringsdorf and Potsdam, Germany

Acknowledgement/Danksagung

- First of all, I would like to express my respectful gratitude to my supervisors, Arkady Pikovsky and Michael Rosenblum. Both have constantly supported me during all stages of my project. Instantly, thoughtful and with faith in my potential. Not only have I been allowed to appreciate the transfer of knowledge on high-level conferences, but I am now allowed, to carry on the scientific spark of curiosity from two leaders of science, and to preserved a scientific heritage of more than half a century of research and exploration.

- I also would like to thank Ulrich Parlitz for his kind and immediate interest in my dissertation. Similarly, I would like to express my thankfulness to Fred Feudel, Achim Feldmeier, Ralf Metzler and Carsten Henkel who all have supported me with quick responses to my requests.

- My scientific life in Potsdam has been made more colourful by my colleagues, Chris, Franzi, Rok, Chunming, Erik, Oleh, Caroline and Marlies; to which I ow many supportive words in the darkest hours and constantly all the time. Moreover I would like to express my thank to Ralf Tönjes for his technical support.

- My deepest gratefulness goes to M. R. without whom I would not have been able to finish this project.

- Finally, I would like to thank all those people, which I do not know in person, but who have made my project possible. This includes: All board members of the Friedrich-Ebert-Stiftung who allowed me to become a fellow of the doctorate programme, and the federal republic of Germany which allowed me to climb up the educational and thus societal stairs as a son of a nurse and a furniture mover.

- How is it possible that I, a child left behind by his classmates and growing up in a region left behind, has made his way? How can it be that, against all the circumstances, I have taken the most unlikely path? The answer encompasses all. It was the warmth of my home, the sun of the beach, the example of my parents and the love of those who have passed away.

- Only due to their support I have been able to accomplish all of this. And on my way I met new people. Many left and only some remained. As such, I, first of all, would like to thank you, Marcus and Frieda for your extraordinary work in reviewing this monograph. It lifted the text to a new level. Moreover, I am glad to know you, Sören and I hope to go on having discussions with you about philosophy...

- But besides my closest friends, there are many others which helped me along with their company. This includes Steffen and the E/KSG, Stamatis and in particular Susanne and Rafael and the many other tangueras in Berlin.

Preface

Philosophy of Science

Bitte beobachten Sie! [...] *Ja, aber was?*[1]

Regarding this conversation, two aspects are of striking importance.

- Two persons communicate with each other. Each of them assumes that the other understands the meaning of their conversation.
- The two persons communicate about the empiric and objective truth; how to describe it and how to perceive – how to observe it.

While the second aspect of the conversation accompanies most of the presented work in the following text, it is a worthy prerequisite to reflect on implications of the upper conversation as both aspects of it together constitute the double-cycle of research[2].

The first, *embedded* cycle of scientific progress has been described by Popper[3] as a cyclic and repetitive three stage process:

- Formulation of theories to describe a phenomenon
- Development of hypotheses
- Experimental test of hypotheses

This means, a theory manifests the paradigm of interpretation for experimental results while an experiment tests hypotheses developed from a theory. Eventually evidence shows that a hypotheses is wrong. Based on the new evidence, the theory is corrected or abandoned in favour of a new one. Three aspects of this philosophic framing are noteworthy:

- Theories are formulated in a language for which the human mind is indispensable.
- Meaning of the first cycle is induced only through communicating individuals.
- It is assumed that written and spoken words have a meaning to the others.

Regarding these dialectic observations, it has been argued by Hösle[4], that the fundamental assumption/agreement of (scientific) communication is *understanding* and that this assumption constitutes a principle who's denial would lead to self contradiction. Finally, Hösle reaches the conclusion that from the usage of language, in itself, an ultimate grounding follows (see [3] p. 152-169). Accordingly, the act of (scientific) communication among subjects is oriented towards a highest point and thus constitutes a second cycle. Namely, the upper communication among

---

[1] p. 19 in [1]: Please observe! [..] Yes, but what?

[2] For an introduction see [1, 2, 3].

[3] Karl R. Popper (1902-1994) [4]

[4] He refers to the works of K. O. Apel in [3].

subjects – as well as this text – assumes *a priori* the existence of an undeniable truth. On the one hand this makes scientific research independent of its outcome. On the other hand it implicitly induces objective truth. Not through the absolute but through the sphere of the human mind.

The human mind in turn, is bound to its existing and finite physical body. At the same time it can explore the infinite, a state of nothingness and develops ideas that are intended to counteract the nature out of which it evolved. Thus, the mind is both, part of a physical world through its brain and at the same time, stands outside and sometimes even in opposition to nature. Classical science implements this two-sided nature of the mind in every experiment: System and observer are mostly assumed to be isolated entities and if they can not be isolated severe problems arise[5].

A theoretical resolution of this tension between subject and experiment will necessarily involve the development of a unified framework for natural phenomena in the universe and ethics[6]. On this endeavour, it is science which guides us, which seeks to gather understanding of the omnipresent mysteries and beauties of the universe, with the only and most fascinating tool to use: the human mind.

Main findings

The following text focusses on specific aspects of oscillatory data analysis relevant for biological and medical research and other disciplines. **The Introduction** is grouped into three complementing parts. The first part presents major examples for non-linear oscillations. These text passages are intended to give a systematic overview of different topics in biomedical research and applications of data analysis for which the findings in this text can be relevant. The oscillatory systems presented in these sections are used to illustrate more advanced problems of analysis in the end of the text. The second part provides an introduction to theoretic concepts for non-linear oscillators, synchronisation and networks with a focus on low-dimensional system reconstructions. In a third part, the relation of observation-based system analysis and theory is discussed with a focus on the transition between them, using the abundant strategy of heuristic modelling.

Chapter two discusses aspects of direct network inference for oscillators. It presents a high-order perturbation theory for the description of irreducible multi-body interactions in networks of oscillators. Such interactions receive more and more attention in recent experimental and theoretic studies as they contribute significantly to the dynamics of networks. In particular, such multi-body interactions are thought to be one major component of neuronal and physiologic functioning in the human body. This chapter also presents numerical methods for the direct inference of such interactions and tests the methods on two paradigmatic oscillatory models.

The remaining Chapters are concerned with topics of inverse oscillatory data analysis with a focus on low-dimensional phase-based methods. **Chapter three** gives a reviews of methods for phase demodulation and related time-frequency analysis with a focus on the Hilbert transform

---

[5] For a sound collection of ontological problems and questions in physics see [5].

[6] See [2] for implications of objective idealism for science and society. See [1] Ch. 2 for a discussion of limitations of reductionism.

and the analytic signal. On the one hand, such approaches are of decisive importance in first-stage heuristic models of oscillatory phenomena. On the other hand, neither of the methods is fully applicable to the problem of phase-dynamics reconstruction. Particularly the Hilbert transform – albeit in widespread use – require special precaution to be reliable. This aspect is introduced in more detail.

Chapter four presents a novel approach for phase demodulation of phase-modulated wideband signals by means of *iterative Hilbert transform embeddings* (IHTEs). A spectral theory for the method is presented and numerical tests are provided that indicate the efficiency of IHTEs. The contributions of this chapter can be regarded as a partial solution to the long-standing problem of wideband demodulation in communication science.

Chapter five addresses the more challenging problem of phase reconstruction for non-linear oscillatory systems by means of a paradigmatic non-linear oscillator and generic observables of its dynamics. In particular, a data-driven reconstruction of the first-order phase dynamics is performed based on IHTE. Moreover, the ability of IHTE to obtain precise phase descriptions of stochastic oscillations is explored with several examples. The remote sensing of such stochastic systems is relevant especially for biological oscillators which operate in noisy environments and often feature essential noisy system components.

Chapter six discusses benefits and limitations of IHTE for phase reconstruction. Generally, the successful reconstruction of a phase dynamics can be hampered if the actual phase dynamics is to complicated and/or if the observed signal is not suitable for phase reconstruction. These two aspects are exemplified by means of several examples. For experimental research this chapter is particularly interesting as it shades light on the actual reliability and validity of the commonly employed Hilbert phase-analysis.

Chapter seven gives an overview of advanced topics regarding potential applications and improvements of the proposed IHTE method, but it also considers the problem of phase-amplitude coupling. A reconstruction of this coupling is already challenging for direct and full observations of a non-linear oscillator. But based on experimental data, it is significantly more complicated. Moreover, due to method-dependent spurious effects, it might not be possible at all to retrieve such valuable information. In the end, further research topics and open questions are formulated in correspondence to the achieved insights and open problems of this work.

Contents

Chapter 1

Introduction

The idea of periodicity and resonance dates back to the very beginning of philosophy in Greece. Namely, the Pythagorean school opted for a harmony of the celestial spheres that would have supported the movement of planets. Accordingly, the mechanic rotation of the spheres against each other would result in vibrations depending on the geometric proportions and would give rise to an omnipresent sound of the cosmos. It was no other than Johannes Kepler[1] more than one and a half millennias later, who still was influenced by this metaphysical idea and who translated the implications of this *harmonia* into a hypothesis for the interpretation of the observational data of early modern astronomy [6].

A century later, one of the first reports on a self-organised non-linear system dates back to Christian Huygens[2]. He observed in 1673 that pendulum clocks on a common wooden beam adjust their rhythms and that the adjustment restores itself after an interruption. Already Huygens concluded that the cause of this *synchronization* was the interaction of the clocks through the tiny movement of the beam [7, 8].

Since then, the understanding of emergent oscillatory phenomena and the experimental and theoretic exploration of the worlds deepest mathematical structures have reached to unseen frontiers. In particular with the dawn of the twentieth century the exploration of non-linear processes has lead to fruitful interrelations among scientific disciplines. For example, in his famous work *On relaxation oscillations*, Balthasar van der Pol[3] hypothesised already in 1926 that the oscillations of the heart and his reported electric-circuit oscillations share a common mechanism of generation [10].

Today, the physics and mathematics of periodic phenomena – in particular synchronization; the simulation and the measurement of oscillating systems has become a central field in research including physics and engineering [11, 12, 13, 14], chemistry [15, 16], biology [17, 18], space science [19], earth system analysis [20, 21, 22, 23], social sciences [24] and physiology (see the forthcoming Sec. 1.1).

In many of these fields, the still existing discrepancy between theory and experimental reality demands for further efforts in the transitional area of signal analysis. A role model in this regard is physiological research where on the bedrock of anatomy and physiology largely new non-linear phenomena are spotted in data and can be related to the theory of non-linear oscillations.

1.1 Biomedical research - a conundrum of complexity

Biomedical research embraces the idea that physiological phenomena are the result of interacting non-linear dynamical systems. The field resides on extensive experimental analysis of physiological data by means of methods ranging from pure statistics to full reconstructions of dynamic models. The obtained insights constitute a modern foundation

---

[1] Johannes Kepler (1571-1630) [4]

[2] Christian Huygens (1629-1695) [4]

[3] Balthasar van der Pol (1889-1959) [9]

for treatment of acute and chronic diseases such as for example ventricular fibrillation [25], spinal cord injury [26], Parkinson's disease[4] [27] or epilepsy [28]. Moreover, research has proven to be able to provide early warning indicators regarding hypertension [29], diabetes [30] and Alzheimer's disease[5] [31]. A central aspect in many of these studies is that the inherent information about the state and functioning of the whole system is provided by the network interactions among subunits [32, 33, 34]. Throughout the introduction, the interplay of dynamical processes, physiology and anatomy for the brain, the kidney and the cardio-respiratory system is presented in more detail with a focus on practical limitations, modelling and analysis.

1.1.1 The human brain

Besides all higher cognitive processes, the brain controls the autonomous nervous system functions of the body and perception. The functional structure of the brain is holistic with only partial separation of single unit dynamics and their network as a whole. An excellent introduction to neurobiology and higher functionality of the brain is provided in [35] and will be presented in brief here.

The basic functional unit in the brain is the neuron. It connects to other cells through vast and complex extrusions of its cell membrane, called axons and synapses[6] (see Fig. 1.1). The emerging network is vast in structural characteristics and functionality: The white matter of a human brain in a 20 year old adult contains synaptic connections with an average length of 150000 - 180000 km and already the neocortext contains up to 2×10^{10} neurons with each having on average 7000 synaptic links [36]! Moreover, the structure of the brain network evolves dynamically in time. This phenomenon, called *neuro plasticity*, allows the brain to learn and adapt to environmental inputs [37, 38, 39]. Brain diseases that counteract a healthy mode of operation affect the whole brain as well as the entire body and are subject of widespread research interests based on non-linear data analysis [40].

Electric properties of neurons

The cell membrane of living cells is perforated by trans-membrane molecules which act as pores for nutrients, messenger molecules and ions. In the nervous system, this functional ability is of vital importance as it enables neurons to efficiently communicate in a highly noisy environment: The neuronal cell membrane incorporates ion channels for Na^+, K^+, Cl^-, Ca^{2+} and other ions (A^-). Due to the inherent molecular fluctuation, some of these channels open and close statistically and result in a passive leakage flux of extracellular and intracellular ions with ionic conductivity g_L. Neurons over-compensate this flux by an active ion pumping which leads to a simultaneous trans-membrane gradient of ionic concentration and electric charge. The resultant flow equilibrium of leakage and active pumping results in a net-negative *membrane potential*[7] $V(t)$ which fluctuates around an *equilibrium potential*. This potential is generally a result of the joint flux equilibria of all

---

[4] James Parkinson (1755-1824) [4]

[5] Alois Alzheimer (1864-1915) [4]

[6] Axons provide signals to other neurons while synapses receive inputs from other neurons. Thus, as the functional mechanisms are of similar type, in the following, both are referred to as *synapses*.

[7] Most notable is the Na^+-K^+ ion pump based on Na^+-K^+-ATPase. It reduces the intracellular concentration of Na^+ while the cell body is enriched with K^+. In each pumping event, three Na^+ ions are transported outward, while only two K^+ ions are pumped inward.

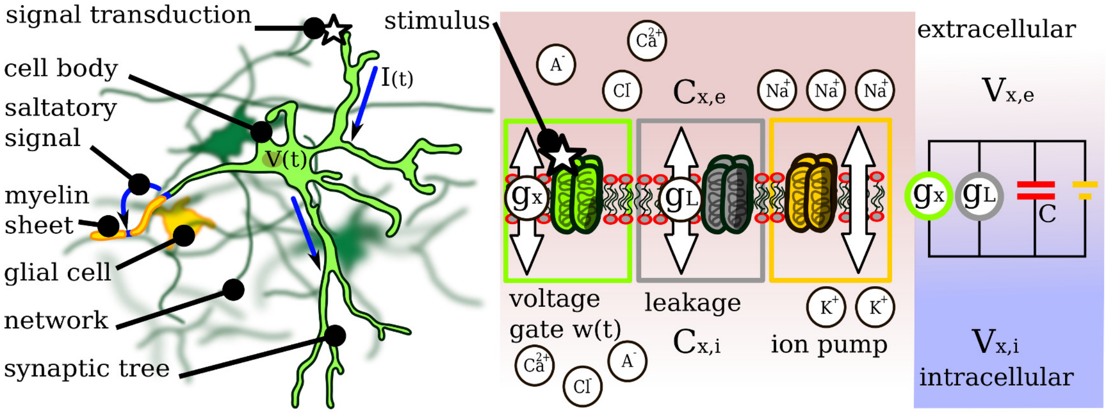

Figure 1.1: Shown on the left is a schematic representation of a pyramidal neuron (green) embedded in a network of neurons (background). The cell's membrane potential $V(t)$ is influenced by synaptic inputs that arrise from signal transduction processes (white star) at the synaptic endings. Signals travel accross the synaptic tree in a saltatory manner due to myelination of synapses (orange). Shown on the right are typical components of a membrane dynamics. Trans-membrane fluxes of ions take place through membrane pores. An active ion pump (orange) maintains gradients of concentration (brown gradient) and electric charge (blue gradient) against passive ionic leakage (grey). The stimuli-dependent ion gate (green) reacts to arriving stimuli (white star). The electric activity of the membrane dynamics can be mapped to an equivalent electric circuit (right). The figure is addapted from [41].

ion species and follows from a non-linear equation. However, the single ionic equilibrium potentials $E_{\mathrm{Na,K,Ca}}$ and others follow in good approximation from the *Nernst equation*[8] which assumes that ionic gating obeys a Boltzmann statistics[9].

Changes of the membrane potential are mainly induced through concerted opening and closing of electro-chemically sensitive ion channels. On a molecular level, this process is realised by conformation changes of the channel molecules. The final state of conformation is approached through non-optimal intermediate stages and occurs more likely if a certain electric or chemical threshold is reached. Additionally, some ion channels can transfer from an opened state into an intermittent inactive state through a second conformation change if the stimulus persists long enough. The average dynamics of many of these channels is modelled by *gating variables* $w(t)$ and conductivities g_x.

The average dynamics of $V(t)$ and $w(t)$ can be described by electric circuit models of varying complexity levels [42, 43, 44]. The essence of these models is that neurons are able to perform limit cycle oscillations and operate in critical states where already small perturbations and parameter shifts can lead to fundamental changes in their dynamics[10].

One such paradigmatic biological model is the Morris-Lecar[11] (ML) oscillator [46]. It describes the dynamics of the membrane potential $V(t)$ generated by non-inactivating slow K^+, fast Ca^{2+} and leakage currents:

$$\begin{aligned} C\dot{V} &= I_0 + \varepsilon p(V,t) - g_L(V - E_L) - g_K w(V - E_K) - g_{Ca} M_\infty(V)(V - E_{Ca}) \\ \dot{w} &= \lambda_w(V)(W_\infty(V) - w) + \zeta(t) \end{aligned} \tag{1.1}$$

---

[8] Walter Nernst (1864-1941) [4]

[9] Ludwig Boltzmann (1844-1906) [4]

[10] This property is reminiscent in biological systems and is referred to as *criticality* [45].

[11] Harold Lecar (1935-2014) [University of California – memoriam]

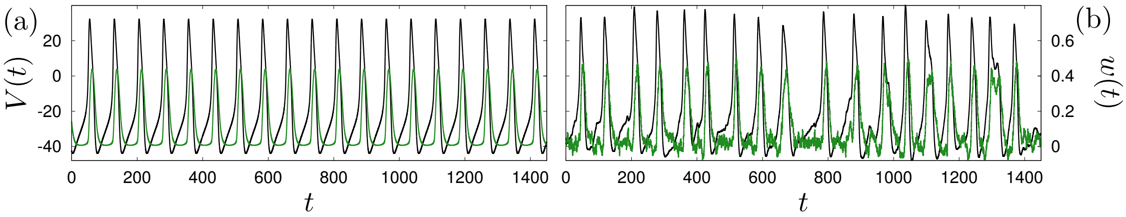

Figure 1.2: Depicted are time series of $V(t)$ (black) and $w(t)$ (green) of the ML neuron model Eq. (1.1). (a): Unperturbed ($\varepsilon = 0$, $\zeta(t) = 0$) system dynamics for $I_0 = 50$ mA. The fast outbursts of action potentials are followed by epochs of recovery where a slow buildup of membrane potential takes place. (b): Same system dynamics as in (a) but subject to Gaussian white noise in the gatting with standart deviation $\sigma = 0.02$ and zero mean.

Here $g_{Ca}M_{\infty}(V)$ is the voltage dependent conductivity of Ca^{2+} ions and $g_K w$ is the conductivity of K^+ ions. The steady-state activation of the K^+ ion gate is denoted as $W_{\infty}(V)$. The strength of the ionic flows is approximated by gradients with respect to the equilibrium potentials $E_{\mathrm{L,K,Ca}}$. I_0 is the synaptic baseline current and $\varepsilon p(V,t)$ is a time varying external stimulus with magnitude ε. For example, $p(V,t)$ models an external current supplied to the neuron in clamp experiments [47] or a synaptic input (see Sec. 7.1). In contrast, $\zeta(t)$ accounts for random fluctuations of the K^+ gating. Details on the model are provided in App. A.1. It can be seen that the dynamics Eq.(1.1) is subject to various sources of noise: External (synaptic) inputs affect the dynamics through $\varepsilon p(V,t)$, the equilibrium potentials $E_{\mathrm{L,K,Ca}}$ are subject to local changes in the trans-membrane gradients of ionic concentration and temperature. Moreover, the gating dynamics depends heavily on temperature through the time constant of activation, $\lambda_w(V)$. As an example, Fig. 1.2 depicts the autonomous and a noise-perturbed dynamics of Eq. (1.1). It can be seen that the oscillation is most sensitive to the random fluctuations in the recovery epoch where already small noise causes a delay of the next spike.

Of decisive importance to achieve the communication among neurons, is the ability of their cell membrane to produce rapid and strong depolarisation events which are called *action potential* (see Fig. 1.2). These events are stereotypical, i. e. their shape and amplitude is largely independent of the initiating stimulus amplitude. Due to its amplitude, the action potentials can excite other gating channels along a synapse. By this, the action potential travels across the membrane until it reaches a dendrite where it initiates neuro-chemical cascades responsible for the transfer of information to the post-synaptic neuron (white stars in Fig. 1.1). In fact, the membrane dynamics allows neurons to perform elementary logical operations[12], such as integration (summation) or frequency dependent passing of inputs (filtering) [49, 50].

Neurons are specialised and organise in multilayer networks of various complexity. A striking example is provided by *glial* cells which couple locally to the primary synaptic network [51, 52]. The membranes of glial cells wrap around synapses and constitute a highly impermeable lipid layer called *myelin sheet*. The isolating sheet allows for an essentially lossless signal transport along a synapse and a *saltatory* conduction of action

---

[12] Theoretical findings suggests that simultaneous oscillatory states in spatially separated synaptic endings of one and the same neuron contribute significantly to the computational abilities in the brain [48](p. 53-70)

potentials what increases the signal speed to up to 100 m/s[13].

As a consequence of this immense structural complexity and simultaneous miniaturisation of single functional units, a mechanistic description of the brain and measurement of brain functions lie at the outermost reaches of scientific capabilities. Therefore, brain models mostly cover the processes of functional brain regions and are in close congruency to recordings of brain activity.

Measurement of brain activity

Measures of brain activity are based on *electroencephalography* (EEG) [55], *magnetoencephalography* (MEG) [56] and structural imaging procedures such as *functional magnetic resonance imaging* (fMRI) [57]. EEG/MEG recordings monitor the electric activity of the neuronal network while fMRI provides a picture of the metabolic activity of certain brain regions.

The recording of brain activity involves many practical issues:

- Non-invasive EEG recordings deal with attenuated signals since the neuronal dynamics is covered by several layers of tissue and the scull. As a consequence, additional spurious statistical effects are present which have to be filtered.
- Highly sensitive electrodes have to be placed in close proximity to each other what can lead to spurious interrelations among signals and thus, to potentially erroneous conclusions about the underlying network state.
- The electrode material can introduce measurement bias.

Unwanted noise might be reduced in extra-cranial MEG recordings or in EEGs measured by implanted electrodes [58, 59, 60]. The remaining random component in itself allows to draw conclusions about the brain network and the deterministic component of neuronal interaction [61].

Epilepsy and Parkinson's disease - functional brain diseases

At the intersection of mechanistic and bio-genetic research epilepsy and Parkinson's disease constitute two main motivations for the development of novel data-analysis tools and computational analysis.

Epilepsy affects nearly 1% of the worlds population. The epileptic brain shows periods of extreme intermittent neuronal activity which are called *seizures* and which can lead to severe convulsion and life-threatening conditions [62]. Two thirds of epileptic patients benefit from an anti-epileptic drug therapy. In an other 8-10% a dissection of the epileptic focus is considered[14] [63]. Statistics of clinical praxis for the latter approach shows that seizures are terminated in 50-80% of patients while for others they reoccur after some time [64].

---

[13] Strong emphasis is put in the understanding and therapy of multiple sclerosis where the myelination is damaged. The improper isolation results in erroneous jumping of action potentials, inflammations and frequently in chronic and successive decline of mental abilities [53, 54].

[14] The onset of a seizure is commonly situated in the temporal lobe.

This suggests that the occurrence of seizures is closely related to structural and functional states of the brain[15]. However, the mechanisms which underlie epilepsy and seizures are still not well understood. In particular, since mutual termination of seizures still constitutes a challenge, a highly active field of research is concerned with the development of seizure predictors to increase the quality of living for medication-resistant epileptic patients [66, 67, 68]. Such predictors necessarily reside on statistical and non-linear methods.

For 25% of patients where neither medication nor dissection is successful, implantation of a pacemaker for deep brain stimulation (DBS) is considered. This approach resides on the idea that the seizure is the result of explosive synchronization which, to be avoided, requires periodic but minimally invasive perturbation of the network state [69].

The current understanding of seizures is based on well established methods of statistics, non-linear dynamics and signal analysis [40]. For example, many studies extract frequency information and signal features by means of the wavelet transform [70, 71] (see Sec. 3.1) or adopt synchronization analysis (see Sec. 1.3.4) which is based on methods for construction of phase variables from signals.

Parkinson's disease is accompanied by a slow and frequently silent decline of the motor control and other nervous system functions. Symptoms affect patients mostly in later stages of life as the brain network is able to compensate disabilities [72, 73]. While in the early stages of the disease a therapy with dopaminergic drugs is possible, in evolved Parkinson's disease this strategy is mostly ineffective [74]. In this stage, significant reduction of life quality arises through the characteristic tremor in the extremities[16] or muscle rigidity. From the perspective of non-linear dynamics however, the involuntary movement is thought to arises from pathological synchronization of motor neurones. This suggests to apply an external driving in the ensemble of neurons to suppresses synchronization.

Indeed, in clinical praxis the tremor and other impairments are significantly reduced by DBS at frequencies around 100Hz. However, there exists consensus that positioning of electrodes as well as parameters of stimulation have to be chosen with caution. It is here, where joint approaches of modelling and oscillatory data analysis can shade light on principal questions: Is a high-frequency forcing responsible for cauterisation of pathological synapses? How should the stimulation be designed to act in a minimally invasive way in the brain [27, 76, 77, 78]? Notably, besides its clinical success, DBS has severe side effects such as depression what has to be treated with secondary therapies [79].

1.1.2 The kidney

The kidney is the main filtration unit for the human blood. It keeps a healthy concentration of ions, removes metabolic waste from the blood, regulates the blood pressure and takes part in the hormone secretion process. Its pathology is influenced by cardiovascular health [80, 81].

The major physiological feature of the kidney is a renal network of finer and finer blood vessels that wire the blood to the basic functional units of filtration which are called

---

[15] For example, a comparative network analysis in [65] indicates differences between the healthy and the epileptic brain

[16] The tremor has a frequency of 3-10Hz [75].

nephrons (see Fig 1.3). In nephrons, the filtration of the blood takes place by osmotic processes in a region of highly convoluted blood capillaries which is called *glomerulus*.

The filtration activity on the level of nephrones involves numerous parameters (see Tab. A.2) but crucially depends on the tubular pressure $P_t(t)$ of the urine and the protein concentration of the filtered efferent blood C_e. Since C_e is not known before the unfiltered blood enters the glomerulus, the nephron tries to adapt its filtration activity in such a way that the difference of glomerular hydrostatic pressure P_g and $P_t(t)$ equilibrates with the osmotic pressure of the filtration. This means, the relation of C_e and P_g is implicit.

The produced urine contains a certain concentration of NaCl and flows to the main duct through highly folded tubules. On its way it is partly reabsorbed with a certain rate F_{reab} and flows through the loop of Henle[17] with a rate $F_h(P_t)$ determined by the gradient of tubular pressure with respect to the main duct. Prior to the main duct, the tubules approach a proximity of the glomerulus and it is in this region, that the NaCl concentration of the liquid is sensed by *macula densa* cells (cyan region in Fig. 1.3) which respond to changes in the NaCl concentration by secretion of messenger molecules. These messengers in turn induce a muscular response of the afferent arteriola walls. The dynamics of the walls affects the resistivity $R_a(t)$ of the capillary. Its dynamics can be modelled by forced damped non-linear oscillations.

The emanating auto-regulative process for the filtration activity $F_g(P_g, P_t, R_a)$ of the glomerulus takes place with a certain characteristic time delay T_t and is called tubulo-glomerular feedback (TGF). The resulting dynamics can have a stable fixed point or harmonic and chaotic oscillatory states with individual average frequency (see Fig. 1.4). There exists substantial effort to describe the nephronic oscillatory dynamics [83, 84]. A model, that captures the described effects is given by the following set of differential equations:

---

[17] Friedrich G. J. Henle (1809-1885) [MPIWG]

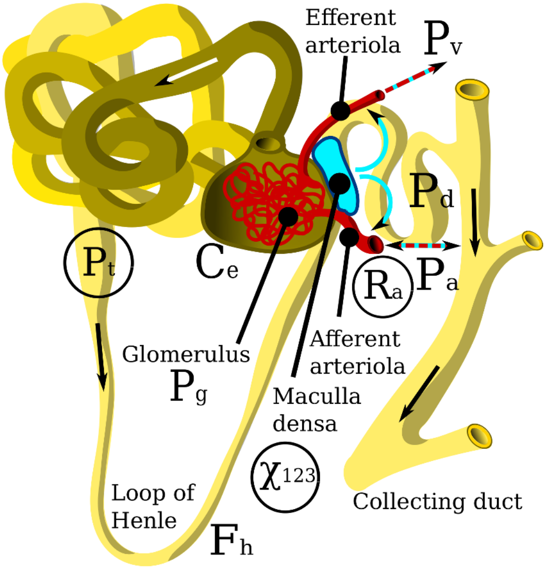

Figure 1.3: Shown is an illustration of a nephron. The maculla densa fills out the space between the arteriolas and the distal tubule. The autoregulative tubologlomerular feedback (TGF) (magenta arrows) arrises due to a multistage cascade process and with a certain time delay due to internal processes of the maculla densa itself and due to the loop of Henle. Coupling between neighbouring nephrons is induced by TGF that travels accross the arteriolas (red-cyan arrows) and hemodynamic coupling (black arrow). The figure is addapted from [82]. Dynamic variables of Eq. (1.2) are encircled.

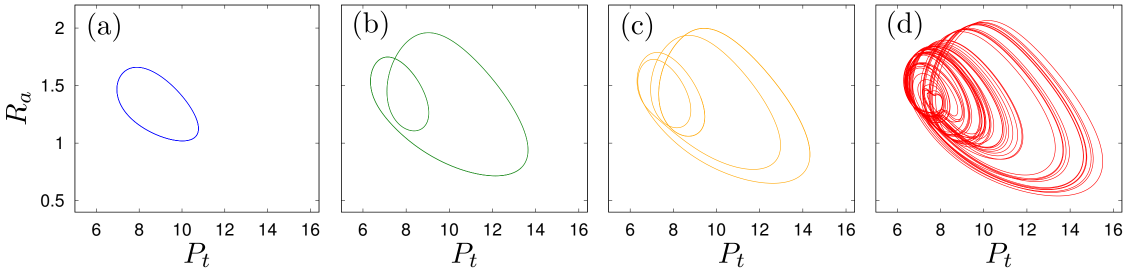

Figure 1.4: Shown are projections of the state space trajectory for the free running nephron model Eq. (1.2) with damping $d = 0.11$. Parameters T_t and c are the main parameters of the autoregulative TGF response which affects the blood inflow to the glomerulus (see Eq.(A.2) in App. A.2). In a pathological state, a nephron loses the ability to respond properly to fluctuations in the blood inflow. In such case, the periodic oscillation (a) is lost and can show period doublings (b,c) ultimately leading to a chaotic oscillation (d). Here, $T_t = 4.5$s is fixed and c is varied to illustrate this behaviour. (a): $c = 2.5$, (b): $c = 7.0$, (c): $c = 8.6$, (d): $c = 12.5$.

$$\begin{aligned}
\dot{P}_t =& [F_g(P_g, P_t, R_a) - F_{\text{reab}} - F_h(P_t)]/C_{\text{tub}}, \qquad F_h(P_t) = (P_t - P_d)/R_h \\
\ddot{R}_a =& -2\omega_a d\sqrt{K(R_a)}\dot{R}_a - \omega_a^2 K(R_a)(R_a - \mathrm{TGF}_c(\chi_3)R_{a,0}) \\
\dot{\chi}_1 =& -\chi_1/T_t + F_h(P_t), \qquad \dot{\chi}_2 = (\chi_1 - \chi_2)/T_t, \qquad \dot{\chi}_3 = (\chi_3 - \chi_2)/T_t \,.
\end{aligned} \tag{1.2}$$

In this model, the heterogeneous response of the macula densa is represented by the third-order delay variables $\chi_{1,2,3}(t)$ and the exerted TGF-activation of the afferent arteriolar resistivity is modelled by a sigmoid transfer function $\mathrm{TGF}_c(\chi_3)$. Further details about the model are given in App. A.2 and originally in [85].

In a healthy operational state, the main response parameters, T_t and c result in a mainly periodic oscillation of nephrons with a distinct frequency. However, there exist other modes of operations – particularly in pathological kidneys – in which nephrons show chaotic oscillations. As an example Fig. 1.4 depicts four such different operational states of nephrons.

1.1.3 The cardio-respiratory system

The overall cardio-vascular-respiratory system is designed to efficiently supply nutrients and oxygenated blood to the cells and to transport metabolic waste in mammals. This is achieved by the self-sustained contraction of the heart muscle which drives the hearts pumping cycle[18].

In terms of dynamical-systems science, heart and lung can be understood as two interacting non-linear oscillators. The interaction between the two oscillators is mediated by the cardio-respiratory centers of the autonomous nervous system and their interaction. Moreover, the cardio-respiratory system receives an independent rhythmic input from the vascular network [87, 88].

The heart's pumping process is based on precise electrical pulses delivered to all compartments of the cardiac muscle by an efficient conduction system that enervates the tissue (green compartments in Fig. 1.5). This tissue consists of specific excitable

---

[18] A broader introduction to the interplay of anatomy and physiology is given in [86] and references therein. In the following, focus is put on the human physiology only.

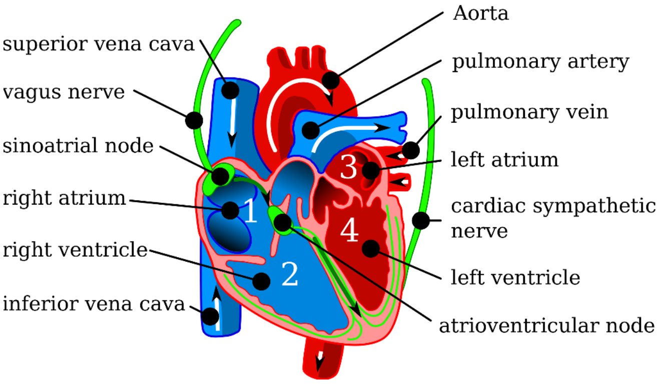

Figure 1.5: Shown is an illustration of a human heart. During a cardiac cycle, blood flows from the right atrium (1) into the right ventricle (2). Due to contraction of the heart muscle, the blood flows to the lungs where it is reoxygenated and enters the left atrium (3). From there it flows to the left ventricle (4) and is pumped with the next contraction into the aorta. The figure is addapted from [93].

cells, the *cardiomyocytes*, which are able to contract due to electric excitation and which have a specific discharge characteristics different from the one observed in neurons. The cells are connected by small protein molecules which act essentially as gap junctions such that action potentials can jump to neighbouring cardiomyocytes. The resultant electro-physiological patterns in the muscle can be modelled as travelling waves in an excitable medium [89, 90, 91, 92].

In a healthy heart, these waves travel in a mostly planar fashion through the muscle, ensuring an optimal cardiac output. The medium however, is highly inhomogeneous as the heart muscle is interspersed by the coronary vasculature, enervating tissue and other supportive structure. Moreover, there can exist scars and other impurities in the muscle at which new excitation waves can be erroneously generated. These patterns correspond to a higher disorder and lower or even terminate the cardiac output in chronic and lethal states of the heart. Their fast and reliable diagnosis, suppression, therapy and understanding is one of the main subjects of cardio-respiratory research[19].

The most widely used signal to monitor the electric activity of the cardiac muscle is the *electrocardiogram* (ECG, see info box)[20]. In clinical praxis, it is interpreted based on long lasting experience [95]. In contrast, there exist comparably fast statistical analysis and theory-based methods which provide reliable data-driven tools for the characterisation of dynamic states of the heart [96, 97]. Moreover, the cardio-respiratory dynamics is reasonably well approximated by a deterministic non-linear model. Its extraction is particularly appealing as it simultaneously provides a paradigm of interpretation, a certain amount of noise reduction and a simplified picture of the numerous physiological effects that influence the hearts beating dynamics [98, 99].

For example, the most widely studied effect of cardiological health is *respiratory sinus arrhythmia* (RSA). It denotes the slowing of the heart beat during expiration and acceleration during inspiration [100]. RSA is caused by electrochemical interactions of the cardio-repiratory centers in the brain [87] and a subsequent interplay of the fast vagal tone and the slow sympathetic tone (see the bold nerve fibres in Fig. 1.5) [101].

---

[19] Medical treatment of cardiac impairment focusses on manipulation of the wave generation in the cardiac muscle. This includes a drug therapy, pace makers or ablation [86](p. 12,13).

[20] The non-invasive ECG is accompanied by ex vivo studies [94]. One goal in these studies is the remote sensing of the three dimensional structure of the excitations from limited data of the cardiac muscle.

ECG signals

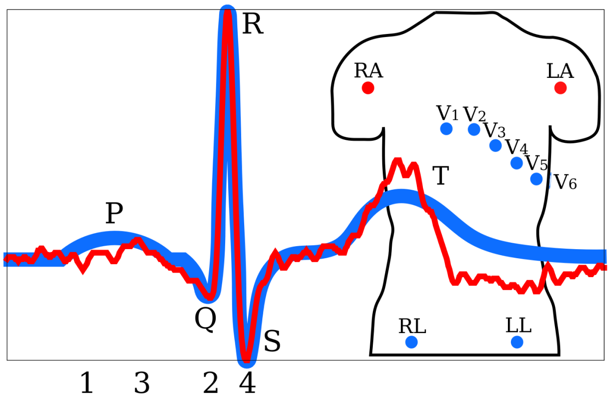

Depicted in red is a period of an ECG measurement taken from lead I ($V_{\mathrm{LA}} - V_{\mathrm{RA}}$) [102]. A schematic representation of standard lead positions V_1 to V_6 as well as RL and LL illustrates the variety of ECG signals to monitor the electric activity of the heart [103, 104]. Time stamps 1 to 4 correspond to the stages of pumping indicated in Fig. 1.5.

The stereotypical excitation cycle of the heart muscle generates a specific shape of the ECG (bold blue line) which is rather prominent even in noisy observations. (P): Polarisation of the right and left atrium. (Q-R-S): Onset and full contraction of the ventricular muscle sheets. (T): Refraction of the muscle and refilling of the atria with blood.

Besides the standard ECG signals, recent developments make extensive use of remote sensing and seek to provide minimally invasive measurement techniques to monitor the cardio-respiratory activity [105, 106].

This interplay is considerably altered in hypertensive or diabetic patients, as a result of stroke [107] or Alzheimer's disease and due to ageing. Thus the analysis of RSA allows to estimate potential silent health risks. The analysis of RSA is based on spectral and statistical methods [108, 109] or model-based data analysis [98, 110, 88]. For all of these methods one has to keep in mind that the variety of different ECG measurements certainly provides different aspects of one and the same dynamical system.

1.2 Nonlinear oscillators

Oscillating behaviour can arise in time-continuous dynamical systems and discrete maps and can be regular and irregular. For example, the voltage oscillation of the ML neuron in Fig. 1.2 arises from a stochastic dynamics while the irregular pressure variations of the nephron model Fig. 1.4 arise from deterministic chaos.

The further text considers only time-continuous dynamical systems. In mathematical terms, such systems are represented by a state $\mathbf{y}(t)$ in an N-dimensional state space which evolves according to the autonomous differential equation

$$\dot{\mathbf{y}} = \mathbf{F}(\mathbf{y}) \; . \tag{1.3}$$

This equation induces a specific state-space geometry which can comprise attractors. The stability of these attractors depends upon the parameters of the model, can change through bifurcations (e. g. see Fig. 1.6) and is characterised by the spectrum of Lyapunov exponents[21] of the system.

---

[21] Aleksandr Lyapunov (1857-1918) [111]

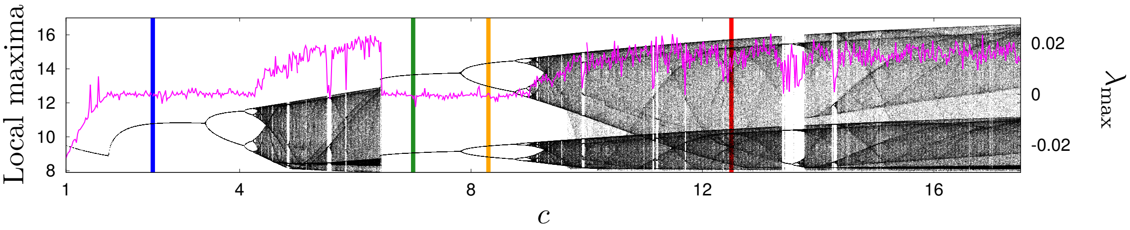

Figure 1.6: Shown is the course of period doubling for the nephron model Eq. (1.2) for $T_t = 4.5$s and $d = 0.11$. Each point in the diagram corresponds to a local maximum of $P_t(t)$ (black). Coloured vertical lines correspond to the snapshots of the projected attractors in Fig. 1.4. The control parameter c determines the response of the TGF (see Eq. (A.2) in App. A.2). Shown as a magenta line is $\lambda_{\max}$.

1.2.1 Types of oscillatory dynamics

According to their dynamical behaviour, oscillators can be grouped into three major classes [112]:

Self-sustained oscillators maintain their periodic motion without external stimuli. Their dynamics is driven by an internal energy source and regulated by feedbacks and dissipation. *Non-chaotic self-sustained oscillators* possess a stable T-periodic limit cycle solution $\mathbf{y}^{(0)}(t) = \mathbf{y}^{(0)}(t+T)$ to which all initial conditions in its basin of attraction converge (see Sec. 1.2.2 for a discussion of stability). *Chaotic self-sustained oscillations* in turn are characterised by an exponential divergence of nearby trajectories $\mathbf{y}(t)$ and $\mathbf{y}(t) + \delta\mathbf{y}(t)$ according to the largest Lyapunov exponent $\lambda_{\max}$:

$$|\delta\mathbf{y}|(t) \simeq |\delta\mathbf{y}|(0)\exp(\lambda_{\max}t) \; .$$

In chaotic systems, this exponent is positive. The resultant divergence is bound to the attractor of the system and results in a finite time-horizon for prediction given by the Lyapunov time $1/\lambda_{\max}$. As an example, the period doubling of the nephron model Eq. (1.2) is presented in Fig. 1.6. It shows how the system for parameter $c \approx 1.7$ develops limit cycle oscillations and undergoes several bifurcations before it reaches a chaotic state. This *route to chaos* is certainly more complicated than for simple dynamic maps or simple chaotic systems due to multi-parameter dependences [84].

Excitable oscillations possess an attractive resting state and an excited state. In absence of external stimuli, they remain quiescent in their resting state. If they receive a sufficient external stimulation, they transfer to the excited state from where they relax back to the resting state. This process usually takes place as a stereotypical event and can be well distinguished from the quiescent state. A simplified example of this behaviour is provided by

$$\dot{\phi} = \omega - \varepsilon\sin(\phi) \; .$$

This dynamics on a ring possesses a pair of fixed points $\phi^\star_\pm \approx \pi/2 \pm \sqrt{1-\omega/\varepsilon}\sqrt{2}$ with eigenvalues $\lambda_\pm = \pm\sqrt{2\varepsilon}\sqrt{\varepsilon-\omega}$ if $\varepsilon \gtrsim \omega$. In fact, the unstable fixed point separates the resting state from the nearby excited state such that already small perturbations across the unstable fixed point cause a full rotation of the system. This mechanism of excitability is reminiscent in biological oscillators as well. There however, with more complex geometries of excitability (e. g. see Fig. 1.7).

Stochastic oscillators combine deterministic dynamics and noise usually by additional random forces in the otherwise deterministic equations of motion. Such forces describe internal statistical fluctuations of the oscillator or external random inputs. In either case such inputs render the dynamics to be essentially non-autonomous and make a prediction of future states difficult or impossible. As an example Fig. 1.2 (b) depicts the ML neuron subject to random fluctuations in the K^+ gating variable $w(t)$.

1.2.2 Stability of limit cycles

The stability properties of limit cycles deserve further discussion: Their asymptotic behaviour follows from the linearised time evolution

$$\dot{\delta\mathbf{y}} = \mathbf{F}'\Big(\mathbf{y}^{(0)}(t)\Big)\delta\mathbf{y}, \qquad \delta\mathbf{y}(t) = \mathbf{D}(t)\delta\mathbf{y}(0), \qquad \mathbf{D}(t) = \exp\left(\int_0^t \mathbf{F}'(\mathbf{y}^{(0)}(\tau))d\tau\right)$$

of a perturbation

$$\delta\mathbf{y}(t) = \mathbf{y}(t) - \mathbf{y}^{(0)}(t) \tag{1.4}$$

for states close to the periodic orbit. Since the cycle is T-periodic, such evolution can be quantified by a stroboscopic observation of the perturbed state trajectory:

$$\delta\mathbf{y}(mT) = \mathbf{D}(mT)\delta\mathbf{y}(0) = \mathbf{D}^m(T)\delta\mathbf{y}(0) \ .$$

Indeed, this equation has a fixed point at $\mathbf{y}^{(0)}(T)$ if the $N-1$ second-largest eigenvalues $\Lambda_k = \exp(\lambda_k T)$ of $\mathbf{D}(T)$ have amplitudes smaller than unity[22]. These eigenvalues are called *Floquet multipliers*[23] and the λ_k are the complex *Floquet exponents.* The ordered set $\{\Re[\lambda_1] > \Re[\lambda_2] > \ldots > \Re[\lambda_N]\}$ resembles the respective Lyapunov spectrum and $\Re[\lambda_1]$ is the largest Lyapunov exponent $\lambda_{\max}$ (see [113] p. 211-217).

Most notably, for stable limit cycles, the largest Lyapunov exponent is zero while all other exponents are negative. This means that eventual perturbations in the direction of the cycle accumulate. Thus, the dynamics in direction of the cycle carries most information while in other degrees of freedom this information degrades according to the negative Lyapunov exponents.

1.2.3 Phase of an oscillator

The stability theory of limit cycles gives at hand a generic *phase-amplitude reduction* of coordinates $\mathbf{y}(t) \mapsto \{\varphi(t), \mathbf{r}(t)\}$ in which the *asymptotic phase* $\varphi(t)$ corresponds to the dominating, neutrally stable dynamics along the limit cycle and all components of $\mathbf{r}(t)$ represent the dynamics of deviations $\delta\mathbf{y}(t)$ from the limit cycle in the dissipative degrees of freedom[24].

The outstanding importance of the phase dynamics is evident: An unperturbed oscillator finally relaxes to the limit cycle. There, the state is solely determined by $\varphi(t)$ no matter how complicated and high-dimensional the dynamics Eq. (1.3) is. Moreover, in the basin of attraction a value of $\varphi(t)$ can be assigned to each state $\mathbf{y}(t)$ that propagates under the unperturbed dynamics towards a state $\mathbf{y}^{(0)}(\varphi)$ on the limit cycle. The corresponding surfaces $\Phi[\mathbf{y}] = \varphi$ of states that all have the same point of convergence on the cycle and thus, the same value of φ are called *isochrones*[25].

---

[22] $D(mT) = D^m(T)$ since $\mathbf{y}^{(0)}(t)$ and $\mathbf{F}'(\mathbf{y}^{(0)}(t))$ are T-periodic. Accordingly, the eigenvalues obey $\Lambda_k(mT) = \Lambda_k^m(T)$.

[23] Achille M. G. Floquet (1847 - 1920) [UStAndrews]

[24] A proof can be found in [114].

[25] In more general terms they are the dominant eigen-solutions of the state-space flow Eq. (1.3) [115, 116, 114].

Isochrones provide the most natural generalisation of the phase to states in the basin of attraction. They link the dynamics of $\varphi(t)$ to the dynamics in state space according to

$$\dot{\varphi} = \Phi'[\mathbf{y}](t)\dot{\mathbf{y}} = \omega = \frac{2\pi}{T}\,. \tag{1.5}$$

Thus, if the full state-space dynamics is available, the dynamics of $\varphi(t)$ can be reconstructed (see Sec. 2.4.1). The opposite, however, is not true: To reconstruct $\mathbf{y}(t)$, also amplitude degrees of freedom are needed in addition to $\varphi(t)$. Construction of the latter however, has lead to a variety of approaches in which the most natural choice is to define amplitude degrees of freedom by surfaces of constant relaxation rate to the cycle. In that case the dynamics of amplitudes is linear. An introduction to the problem is provided in [114, 117] and makes extensive use of the standardised Koopman-operator theory[26].

Noteworthy, Eq. (1.5) describes the dynamics of the asymptotic phase in the whole basin of attraction. However, the inference of it based on data has only recently been studied in detail [119]. If the free running system relaxes in the basin of attraction to the limit cycle, the phase dynamics is nevertheless given by Eq. (1.5) what defines the isochrones implicitly for nearly all non-linear oscillators (see Sec. 2.4.1 for further details). It is this deeply rooted fact, which poses significant demands for a mathematical description of the phase dynamics in oscillators and further demands for an experimental inference of the isochronic structure.

1.2.4 Weakly perturbed phase dynamics and isochrones

The density and form of isochrones characterises the response of an oscillator to perturbation and its internal perception of time. Namely, if isochrones are spars, the phase changes slowly on a trajectory $\mathbf{y}(t)$. In contrast, if their density is larger, the phase changes more rapidly. As an example, Fig. 1.7 depicts the highly inhomogeneous isochronic structure of the ML neuron: In the lower left part of the cycle, already small perturbations $\delta\mathbf{y}(t)$ will cross over many isochrones. Thus, the response of the phase will be large. In contrast, in most other regions of the state space, the response will be significantly smaller.

The relation of phase dynamics and isochrones can be further examplified: If an oscillator is continuously perturbed from its limit cycle by an additive, weak and non-parametric perturbation $\varepsilon\mathbf{p}(t)$, the phase dynamics is

$$\dot{\varphi} = \omega + \varepsilon\mathbf{Z}(\varphi)\cdot\mathbf{p}(t), \qquad \mathbf{Z}(\varphi) = \Phi'[\mathbf{y}^{(0)}(\varphi)], \tag{1.6}$$

where the isochrone gradient $\mathbf{Z}(\varphi)$ is called phase sensitivity function or *infinitesimal phase response curve* (iPRC). It must be noted that this equation is a first-order approximation in ε since the perturbed state trajectory is approximated by the limit cycle solution. Such an assumption is indeed justified if an introduced perturbation degrades essentially in one period of oscillation. Instead, if the system has not relaxed sufficiently, a new phase response depends on the shape of isochrones at a generic state $\mathbf{y}(t) \neq \mathbf{y}^{(0)}(t)$ and on the recent input. Such phase dynamics however, is not completely described by Eq. (1.6).

Nevertheless, if $Z(\varphi)$ is strictly positive $\dot{\varphi}$ increases throughout a period. Thus, the perturbed oscillator[27] completes one revelation close to the limit cycle always in a

---

[26] Bernard O. Koopman (1900-1981) [118]

[27] Here and in the following, $Z(\varphi)$ is a scalar function, corresponding to perturbations in one direction of the state space.

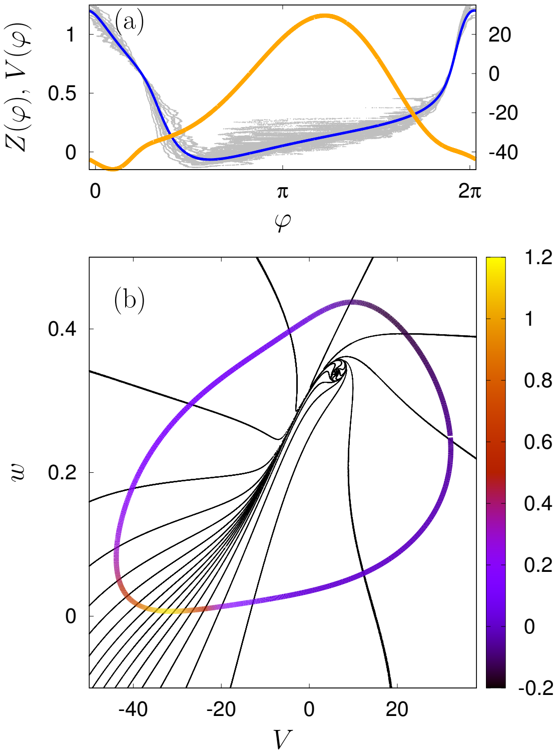

Figure 1.7: Shown in (a) is the function $V(\varphi)$ for the unperturbed (blue) and for the noisy (grey background) ML neuron Eq. (1.1) (see Fig. 1.2) and the phase sensitivity function $Z(\varphi)$ (orange). The state trajectory of the noisy system undergoes massive fluctuations in the regions of high phase sensitivity. Moreover, it is indicated that these fluctuations cause an essentially non-monotonous phase dynamics. Shown in (b) is the state space plot of the same unpertubed ML neuron. The bold colured line is the limit cycle solution and the line colour indicates the amplitude of $Z(\varphi)$ in (a). Black curves show exemplary isochrones $\Phi[\mathbf{y}] = \pi k/10$, $k \in [1, 20]$. Further details of iPRC construction are provided in App. A.3. The Isochrones are obtained using the relaxation method discussed in Sec. 2.4.1.

shorter amount of time. In contrast, if $Z(\varphi)$ changes sign in a period, proper timing of a perturbation results in phase delay ($Z(\varphi) < 0$) or advance ($Z(\varphi) > 0$). Thus, it can be readily seen that the phase sensitivity is of great importance, for example, in DBS where the goal is to perturb whole populations of neuronal oscillators by an optimal and non-destructive input.

The experimental inference of the iPRC thus, is a major topic in neurological data analysis. An overview of the field is provided in [48] and an example for a neuronal iPRC is given in Fig. 1.7. Indeed, it can be seen that the region of highest isochronic density coincides with the region of highest phase sensitivity.

1.2.5 Synchronization

Synchronization is the process of rhythmic adjustment due to small interaction among oscillating units. The phenomenon is reminiscent in non-linear systems and underlies emergent patterns, reaching all the way up to the integrated dynamics present in biological oscillators.

The process of synchronization can be described in statistical or topological terms. This is to say that the adjustment of rhythmic behaviour causes a (partial) collapse of the state distribution in an ensemble of interacting units or that single units tend to converge to a common attractor in the joint state space [8]. In either case, the state of synchrony is characterised by generic collective variables of the ensemble of oscillators. In the following, emphasis is put only on the notion of *phase synchronization*, i. e. the adjustment of phases and frequencies in an ensemble of oscillators.

The idea of collective variables can be best understood in the Kuramoto-Daido model[28]. It is based on two major assumptions:

---

[28] A societal application of modified Kuramoto-Daido models is found in power-grid analysis [14].

- Perturbations to the oscillators are small such that each unit is well described by a scalar phases dynamics on the limit cycle.
- The oscillators are coupled to each other and this coupling can be pairwise or non-pairwise; it can be local or all-to-all with a coupling strength ε.

In its basic formulation of pairwise all-to-all coupling in an ensemble of M oscillators, it is further assumed that the coupling functions are well presented by slow (resonant) phase interactions

$$\dot{\varphi}_k = \omega_k + \frac{\varepsilon}{M} \sum_{j=1}^{M} h(\varphi_j - \varphi_k) \ . \tag{1.7}$$

Here, ω_k reflects the individual autonomous dynamics of each oscillator [120, 121].

Neural synchronization and communication

Synchronization generally plays a key role in neuronal communication since it allows groups of neurons to act in unison and against the omnipresent statistical fluctuations [61, 122]. Its data-based detection among sensors thus, constitutes a way to measure interactions among brain regions.

From the viewpoint of signal analysis, generic synchronization effects correspond to characteristic frequency bands in the spectra of signals [58]. This view is complemented by mathematical modelling where it is hypothesised that the emergent oscillatory dynamics arises due to a generalised synchronization of the noisy neuronal oscillators. Neural synchronization is highly intertwined with the state of the evolving brain network and characterises different modes of its operation such as neuronal avalanches, brainwaves and chimera-like states [123, 124, 125, 126].

The coupling function $h(\varphi_j - \varphi_k)$ can generally be represented by a Fourier-series[29]. For example, if the term $\sim \exp(i(\varphi_j - \varphi_k))$ dominates, the coupling function might be well approximated by the first harmonics. Then, the dynamics effectively decouples in the mean-field representation

$$\mathcal{R} \exp(i\Psi) = \frac{1}{M} \sum_{j=1}^{M} \exp(i\varphi_j)$$

to obtain

$$\dot{\varphi}_k = \omega_k + \mathcal{R} \sin(\Psi - \varphi_k) \ .$$

Here, Ψ is the phase of the mean field.

The *order parameter* $\mathcal{R}$ approaches unity if all phase differences $\varphi_j - \varphi_k = 0$. In this case one speaks of *full phase synchrony*. If $\mathcal{R}$ fluctuates close to zero, the oscillators are essentially *asynchronous*[30] what means that the phases are not locked. In states of *partial phase synchrony*, the value of $\mathcal{R}$ varies between zero and unity. A generalised measure to quantify this locking is for two oscillators given by

$$\mathcal{R}_{n,m} = \langle \exp(i(n\varphi_j - m\varphi_k)) \rangle_t \ . \tag{1.8}$$

---

[29] Joseph Fourier (1768-1830)[4]

[30] These fluctuations are a result of finite size effects while in the limit $M \mapsto \infty$ they eventually vanish [127].

It is called *phase-locking value*[31] and finds application, for example, in the analysis of neurological data.

Renal synchronization and filtration

A healthy human kidney contains 10^6 nephrons while its average total kidney volume is $1.34 \times 10^{-4}\text{m}^3$ what results in roughly 7.5×10^9 functional units per m^3 and stresses the tremendous complexity of the system [82, 128].

A healthy operational state of kidneys is characterised by a certain amount of partial synchrony induced by a heterogeneous coupling with two major mechanisms: First, hemodynamic coupling due to pressure changes that travel backwards in the vascular tree and second, an electrochemical response of the TGF that travels the muscle walls of the arteriolas. While the first leads to out-of-phase synchrony, the latter can lead to partial phase synchrony and states of higher synchrony [83, 129, 130].

The balance of both effects depends on a plethora of factors which are yet not fully explored. Noteworthy, the whole renal network, maintains a throughput of $0.2 - 0.3\text{l}$ per minute in humans while the average blood flow in a single nephron is not higher than $200 - 300\text{nl}$ per minute. Such an orchestrated performance is enabled by the self-organised synchronization in the heterogeneous renal network.

The combinations of integers n and m correspond to higher modes of coupling in which also phase differences $n\varphi_j - m\varphi_k$ can be resonant. An even further expansion of the notion of synchrony arises if not only two but a generic combination of oscillator phases enters in Eq. (1.8). Such locking corresponds to generic phase-dynamics effects beyond the weak-coupling limit and can be described by generalised phase-dynamics equations. It is a hallmark of high-order oscillatory phenomena [131]. In Ch. 2 such a high-order phase reduction theory is presented and exemplified.

1.3 Heuristic analysis of non-linear oscillations

In contrast to settings in which a description of phenomena based on first principles is possible – in which the governing equations of motion are known a priori – oscillation phenomena in non-linear systems commonly arise from heterogeneous sources. Most prominently in biological systems, interactions among functional subunits become more and more divers while at the same time, single compartments shrink to a microscopic size.

As a consequence:

- Disintegration of the system into its single compartments to isolate single processes omits the holistic nature of the dynamics present in the systems.
- The amount of information needed to characterise the systems full state exceeds available computational means.
- The necessity for ethical treatment of individuals demands a non-invasive measurement or therapy. At the same time, available sensors mostly do not fit the degree of miniaturisation and complexity present in the system.

---

[31] $\langle . \rangle_t$ denotes an averaging over time.

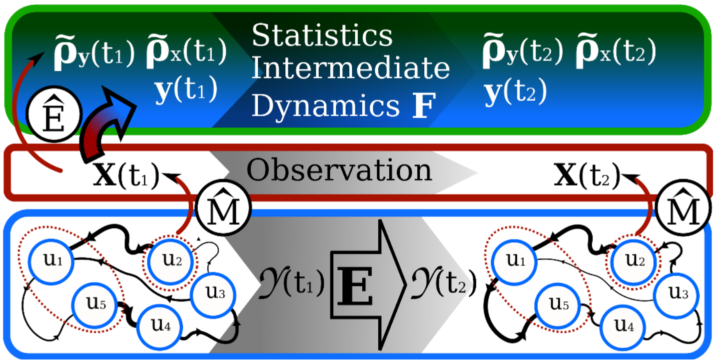

Figure 1.8: Schematic overview of heuristic analysis and modelling. The actual system $\mathcal{Y}(t)$ evolves in time (gray scale) according to the operator $\mathbf{E}[\mathcal{Y}]$. Non-invasive observations $\hat{M}$ (red) and/or embeddings $\hat{E}$ transfer the information to the analysis level (green).

Consequently, a *heuristic* analysis is needed. This is to say, the actual dynamics exits but instead of reconstructing it in full detail, one pursues the strategy to employ a generic mathematical frameworks (see Fig. 1.8) with two main goals:

- Inference of system properties such as for example, network structure, response properties and geometric features of the state-space dynamics.
- Prediction of the future of the observed systems based on the available data[32].

Available analysis makes use of *statistical methods*, *state-space methods* and *model reconstruction techniques* which each focuses on specific aspects of system theory and data analysis.

1.3.1 Model-based analysis

The goal of model-based data analysis is the reconstruction of the original dynamics as close as possible. This means an equation of motion Eq. (1.3) is assumed to underlie the deterministic component of the actual time evolution $\mathbf{E}(\mathcal{Y})$. This dynamics can be inherently noisy such that the reconstruction of a model represents a specific form of noise filtering.

In accordance to infer the original dynamics, the existence of a smooth generic coordinate transformation is assumed. This transformation, which is called *measurement*, projects the original M-dimensional state-space trajectory $\mathcal{Y}(t)$ to a signal

$$\begin{aligned} \hat{M} : \mathbb{R}^M &\to \mathbb{R}^m \\ \mathcal{Y}(t) &\mapsto \hat{M}[\mathcal{Y}](t) =: \mathbf{X}(t) \ . \end{aligned} \tag{1.9}$$

Here, $\mathbf{X}(t)$ is the observed multivariate signal.

The data-based reconstruction of the dynamics is achieved in two steps:

(I) Construction of the heuristic state $\mathbf{y}(t)$ from $\mathbf{X}(t)$

(II) Extraction of its dynamics $\mathbf{F}(\mathbf{y})$.

This approach is particularly appealing as it allows to draw conclusions about the geometric and dynamic properties of the underlying system dynamics $\mathbf{E}(\mathcal{Y})$ from the reconstructed dynamics $\mathbf{F}(\mathbf{y})$ which would otherwise be hard to achieve.

---

[32] An introduction to this topic of forecasting can be found in [132].

Step (I) in this procedure, definition of a mapping

$$\begin{aligned} \hat{E} &: \mathbb{R}^m \to \mathbb{R}^N \\ \mathbf{X}(t) &\mapsto \hat{E}[\mathbf{X}](t) = \mathbf{y}(t) \ , \end{aligned} \tag{1.10}$$

relates the heuristic state $\mathbf{y}(t)$ to the experimental data. The mapping $\hat{E}[\mathbf{X}](t)$ is called *embedding* [133] (see Sec. 4.1.1 and in particular Fig. 1.9).

Step (II), reconstruction of the dynamics, is achieved by a numerical fitting procedure, if the form of the dynamics is known [134, 135]. In other cases, a generic model dynamics $\mathbf{F}(\mathbf{y})$ is needed. The drawback of such an approach is that the reconstructed model receives legitimacy only through its predictive power while single terms in a dynamics not necessarily have a physical meaning[33].

The transition

$$\mathcal{Y}(t) \overset{\hat{M}}{\to} \mathbf{X}(t) \overset{\hat{E}}{\to} \mathbf{y}(t)$$

faces two main problems:

- Determination of $\hat{E}[\mathbf{X}](t)$ constitutes a mathematically under-determined problem. If the number of available measurements is smaller than the dimension of the actual system, degrees of freedom have to be reconstructed according to some generic rule. For example, an univariate time series $X(t)$ which shows oscillations needs to be embedded at least into a two-dimensional space to ensure uniqueness of the solution. What is the most natural way to construct additional degrees of freedom from $\mathbf{X}(t)$?
- The information content of $\mathbf{X}(t)$ can be to low. First, some features of the original state trajectory can be underrepresented in the data [137]. Second, a finite observation keeps track of only a specific portion of the state space. Thus, specific features of the dynamics are potentially not even measured.

Regarding step (II), meaning of the model reconstruction can be ensured by inference of the phase dynamics equation: On the one hand, the phase-reduction theory induces a clear meaning of the reconstructed phase. On the other hand, the phase of a signal can be readily obtained using phase reconstruction techniques. These techniques are generally more stable than standard embedding methods [138, 133] (see Ch. 4).

What remains to be clarified is the transition (red-blue gradient in Fig. 1.8) from phases of signals to *the* asymptotic phase of an underlying system. This transition in itself is based on assumptions and gives rise to other methodological problems as discussed in Ch. 3. Quite generally, it is not possible to reconstruct the asymptotic phase from incomplete observations ($m < M$). The reason for this is the definition of $\varphi(t)$ according to isochrones. However, there can exist specific circumstances in which a reconstruction yields reasonably good agreement [139].

1.3.2 State-space methods

A more generic approach to oscillatory data is provided by general state-space methods based on the delay embedding

$$\begin{aligned} &\hat{E}_{\tau_e,N} : \mathbb{R}^m \to \mathbb{R}^N \\ &\qquad \mathbf{X}(t) \mapsto \hat{E}_{\tau_e,N}[\mathbf{X}](t) = [x_1(t), \ldots, x_1(t - n_1\tau_e), \ldots, x_m(t), \ldots, x_m(t - n_m\tau_e)] \ . \end{aligned}$$

---

[33] This is one of the aspects of machine learning techniques and there, attracts specific attention [136].

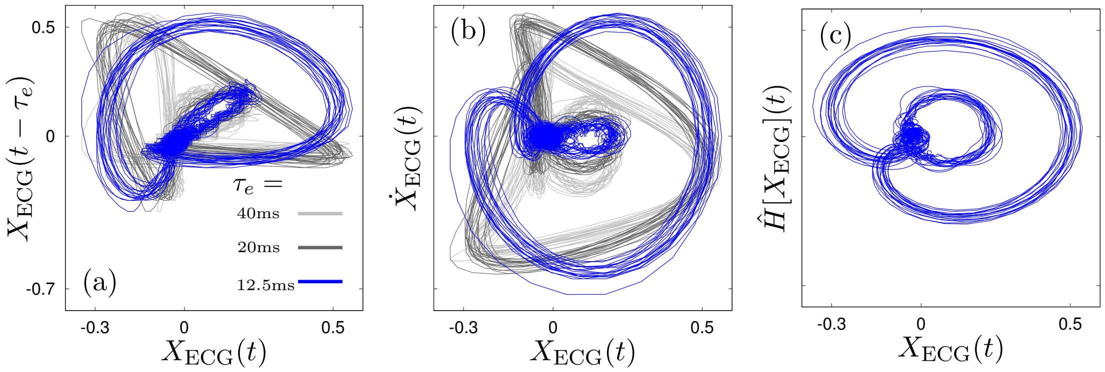

Figure 1.9: Shown are exemplary embeddings of the lead 1 ECG data of Fig. 3.1(b). (a): Delay embeddings of the detrended ECG data. For a delay time of $\tau_e = 12.5$ ms (●) the attractor unfolds whereas for delays of $\tau_e = 40$ ms (●) and $\tau_e = 20$ ms (●) the attractor geometry complicates. (b): Derivative embeddings of the same data. The derivative is obtained with a high-order polynomial filter (see Sec. 5.2.3). The embedding unfolds the attractor for a calculation window of 28 ms (●) whereas larger windows of 80 ms (●) and 60 ms (●) cause the embedding to gradually collapse. The derivative was normalised to the amplitude of the signal. (c): Instead, the Hilbert transform (see Ch. 3) unfolds the large and smaller main loops mutually without parameter adjustments needed.

Its construction depends on the embedding dimension N and the delay time τ_e. This embedding method faces two major problems:

- No unique way of estimation for the embedding dimension and the delay time is known. However, since the embedding should preserve deterministic features of the dynamics, one strategy is to chose N in such a way that the embedding dynamics remains continuous and smooth[34]. The delay time τ_e in turn has to be selected such that the redundant correlations in the embedding are reduced[35]
- For unperturbed systems, Taken's embedding[36] theorem ensures the existence of mappings $\mathcal{Y}(t) \mapsto \mathbf{y}(t)$ [142]. However, no such mapping is guaranteed to exist for perturbed systems.

A special type of delay embedding is the derivative embedding.

$$\begin{aligned}&\hat{E}_N : \mathbb{R}^m \to \mathbb{R}^N\\ &\qquad \mathbf{X}(t) \mapsto \hat{E}_N[\mathbf{X}](t) = \mathbf{y}(t) = [x_1(t), \ldots, x_1^{(n_1)}(t), \ldots, x_m(t), \ldots, x_m^{(n_m)}(t)] \; .\end{aligned}$$

Here $x_j^{(n)}(t)$ is the nth-order derivative of the jth component of data. Its estimation from noisy data demands for additional smoothing procedures or a high-order estimation scheme for the derivative (see Sec. 5.2.3).

Despite these obstacles, the delay embedding is the foundation of numerous analysis procedures. It allows to study generic invariants of the original dynamical system such as the geometry and dimension of the attractor and its stability properties, it is employed

---

[34] This approach is called false nearest neighbour statistics [140].

[35] A similar situation occurs for multi-channel EEG measurements where the distance of electrodes plays the role of τ_e.

[36] Floris Takens (1940-2010) [141]

in forecasting and in statistical analysis to identify deterministic dynamical components [132].

1.3.3 Statistical analysis

The most generic approach to interprete data is provided by statistical methods which can be deployed as part of the former deterministic analysis or in a stand-alone mode. In either case, the analysis assumes some stationarity of the data what in turn allows to test for non-stationarity. For example, a binned analysis of mean, variance and autocorrelation can be performed. More sophisticated tests involve *surrogates* which eventually rule out specific statistical properties of data [143, 59].

To some extend, statistical analysis can also lead to prediction if the true state dynamics of a system is observed. Then, the estimation of the evolving systems statistics can be achieved from data by fitting of the Fokker-Planck equation. However, generally it is not possible to embed a stochastic process.

1.3.4 Network inference

The preliminarily discussed biological oscillation phenomena of the brain, the kidney and the heart (see Sec. 1.1) all arise from heterogeneous network interactions. Thus, a heuristic model for these systems needs to *infer* not only the dynamics of single units but also their *connectivity.*

First, this task deals with the same problems as heuristic modelling in general. Second, the conclusion that two nodes are connected derives from different data-based criteria. Generally, oscillators in a network are connected by some physical links. These links can be realised for example by synapses in the brain (see Fig. 1.1) or the arteriola-tublar connections in the kidney (see Fig. 1.3). The abstracted mathematical network of such connections thus, defines the *structural coupling.*

Strutural coupling in the kidney and inference

The interactions of nephrones have been inferred using in-vivo oscillatory data analysis [144]. Direct measurement of surface-nephron activity is based on laser-speckle flowmetry [145] which allows to determine the velocity of red blood cells and thus the arteriolas resistivity in surface nephrons. However, reconstruction of the deep renal network relies on invasive experimental techniques and evidence-based mathematical modelling [146]. The evident problem here is that inference of the connectivity in the free running system is not possible. Either one disintegrates the whole organ to characterise the structural connectivity but terminates the dynamics or one observes the undisturbed oscillations without perception of the deep network structure. In the latter case however, crucial features of the network state are neglected.

In particular, this means that an interaction of two units exists structurally only if a link is physically present. As an illustration, Fig. 1.10 depicts a triplet of oscillators. In this triplet, oscillator ① and ② are structurally connected to each other with coupling strength $c_{1,2}$ and $c_{2,1}$. In contrast, oscillator ③ is connected unidirectionally to oscillator ② with strength $c_{2,3}$.

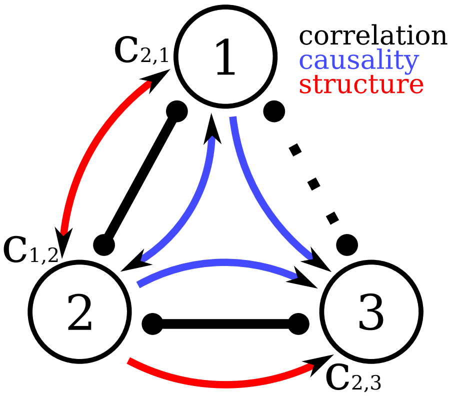

Figure 1.10: Schematic representation of a triplet of oscillators. Oscillator 1 and 2 are structurally connected (red arrows). In contrast, oscillator 3 is forced by oscillator 2 only. The undirected functional connection (black links) indicate potential structural connections between all oscillators although oscillator 1 receives no information from 3. A causality measure or a model based analysis allow for inference of the directionality of coupling and all effective coupling links (blue arrows).

Due to the structural links oscillator ① receives information from ② and vice versa. Moreover, oscillator ③ receives information about the state of oscillator ②. The latter inherits some information about the state of oscillator ① as well. As a consequence, there arises an *effective functional coupling* link from oscillator ① to ③. This coupling link is by no means present in the structural network and is a genuine result of the non-linearity of single oscillators.

The inference of the connectivity can be based on model-free statistical analysis using the *cross-correlation* between signals. Correlations are a measure for the similarity of signals. Thus, such analysis provides no conclusions about causation. For example, the cross-correlation detects coupling for all pairs of oscillators (black lines in Fig. 1.10) with no discrimination of structural (bold) and effective links (dashed). Moreover, it is possible to think of a situation in which the coupling constant $c_{1,2}$ vanishes. Then, oscillator ② forces oscillators ① and ③. The resulting correlation among these units thus, will be very strong although they do not interact at all.

A stricter analysis can be carried out by means of *causality* measures. In contrast to correlation, these methods involve some asymmetry in the calculation and thus are able to monitor causal relations among units [97, 40]. An illustration is given in Fig. 1.10: Again, the effective coupling link is identified but this time with information on causation (blue arrows).

Correlation and causality can be parameter free methods of estimation what makes them a good tool for the study of generic signals. However, both methods do not allow to distinguish the qualitative difference of structural and effective coupling. To achieve this goal one is forced to reconstruct a *heuristic model* of the network dynamics. The advantage of such an approach is its descriptive and predictive power. Its drawback is that results are meaningful only for a certain range of model parameters and that the model reconstruction itself involves several sophisticated steps related to the projections Eqs. (1.9) and (1.10). The method of Ch. 2 implements a heuristic model reconstruction. It is based on the notion of asymptotic phase.

The statistical and model-based inference of network links is complemented by estimation of the phase synchronization among network units using the phase locking value. The reason for this is that synchrony most likely implies interaction[37]. Again, this analysis is heavily based on an accurate determination of the respective true phases $\varphi(t)$ for each unit.

---

[37] A novel field of research examines effects of quantum synchronization which is in close correspondence to the well studied phenomenon of entanglement [147].

Finally, an important aspect in networks is the *directionality of coupling* as it measures the relative strength of coupling links which is often readily computable based on signal analysis techniques alone or based on a reduced phase model [148, 149]. Similarly statistical and mixed techniques can be employed as well [150, 151].

Chapter 2

High-order phase reduction for coupled oscillators

Bibliographic information

The main results in this chapter have been published in:

Erik Gengel, Erik Teichmann, Michael Rosenblum and Arkady Pikovsky
High-order phase reduction for coupled oscillators
Journal of Physics: Complexity 2.1 (2020): 015005

Main findings:

- Presentation of an analytic high-order phase reduction method
- Development of a numerical method for phase and frequency estimation in oscillatory models
- Development and application of a numerical method for multivariate network reconstruction based on the asymptotic phases and comparison to mathematical results

2.1 High-order phase coupling

In the introduction the phase dynamics Eq. (1.6) is derived for the limit of small perturbations what leads to a clear separation of system response and external stimulus. In the more general circumstance where the perturbation $\delta\mathbf{y}(t)$ integrates up, a high-order phase reduction becomes necessary. This aspect of phase-reduction theory is analysed here in detail for a network of three coupled Stuart-Landau[1] (SL) oscillators and a network of van-der-Pol (VdP) oscillators. The essence of this analysis shows that the phase-dynamics network possesses irreducible hyper-network structures in which oscillators act as a group and which gain importance in networks of strongly coupled non-linear oscillators [153, 154, 155].

2.1.1 Phase reduction hierarchy

The starting point for a mechanistic description of hyper-network structures is the state dynamics of many oscillators:

$$\dot{\mathbf{y}}_k = \mathbf{F}_k(\mathbf{y}_k) + \varepsilon \mathbf{G}_k(\mathbf{y}_1, \mathbf{y}_2, ...)\ . \tag{2.1}$$

---

[1] Lew D. Landau (1908-1968) [152]

Here, the units are coupled by functions $\mathbf{G}_k(\mathbf{y}_1, \mathbf{y}_2, ...)$ which are scaled by a small common coupling strength ε. Then, according to Eq. (1.5), each phase dynamics is given by

$$\dot{\varphi}_k = \omega_k + \varepsilon \Phi_k'[\mathbf{y}_k] \cdot \mathbf{G}_k(\mathbf{y}_1, \mathbf{y}_2, ...) \ . \tag{2.2}$$

It can be seen that each phase relies on information about the generally unknown functions $\Phi_k[\mathbf{y}_k]$ and all state space trajectories $\mathbf{y}_j(t)$ through the coupling function $\mathbf{G}(.)$.

Indeed, in the linear approximation it thus follows:

$$\dot{\varphi}_k = \omega_k + \varepsilon \Phi_k'[\mathbf{y}_k^{(0)}(\varphi_k)] \cdot \mathbf{G}_k(\mathbf{y}_1^{(0)}(\varphi_1), \mathbf{y}_2^{(0)}(\varphi_2), ...) = \omega_k + \varepsilon Q_k^{(1)}(\boldsymbol{\varphi}) \ . \tag{2.3}$$

Here, $\boldsymbol{\varphi} = [\varphi_1, \varphi_2, ..., \varphi_M]$ and $Q_k^{(1)}(\boldsymbol{\varphi})$ is the first-order phase coupling function. It is equivalent to Eq. (1.6) and illustrates the tremendous reduction of the $N \times M$-dimensional dynamics of the network units to a set of only M scalar equations for the phases $\varphi_k(t)$!

Additional features of the dynamics arise due to perturbations $\delta\mathbf{y}_j(t)$ (see Eq. (1.4)): Since the perturbation depends on states of all oscillators, the phase of each oscillator couples – through the isochronic dependence on amplitudes – to all other oscillators in higher orders of ε. Ultimately, this leads to a hierarchy of high-order phase coupling functions:

$$\dot{\varphi}_k = \omega_k + \varepsilon Q_k^{(1)}(\boldsymbol{\varphi}) + \varepsilon^2 Q_k^{(2)}(\boldsymbol{\varphi}) + \varepsilon^3 Q_k^{(3)}(\boldsymbol{\varphi}) + ... = \omega_k + Q(\boldsymbol{\varphi}) \ . \tag{2.4}$$

Such an expansion, assumes that the relation of amplitude and phases $\boldsymbol{\varphi}$ is algebraic, i. e. the amplitudes are enslaved to the phases. In geometrical terms this means that the torus, spanned by $\boldsymbol{\varphi}$, stays intact under perturbation. Beyond this limit, a generalised phase-amplitude reduction becomes necessary and results in at least M differential equations for phase and M differential equations for the amplitudes [117, 115].

2.1.2 Consequences of high-order phase coupling

The theoretic consequences of the phase-reduction hierarchy are significant for network reconstruction: While measures of statistics, keep track of mere appearances of interaction instead of true mechanisms, the phase dynamics Eq. (2.4) mutually incorporates the structural as well as the functional coupling links! Most importantly, it allows to distinguish the latter from the first by their scaling behaviour in ε. For example, if a coupling link is structurally present it scales $\sim \varepsilon$. In contrast, if the link is functional, the largest non-vanishing interaction term scales $\sim \varepsilon^2$.

First, this means that the high-order phase model Eq. (2.4) can be utilised to identify complete chains of interaction among oscillators that arise due to effective coupling. (For example, in Fig. 1.10 such a chain is directed from oscillator ① to oscillator ③.) In turn, in a data-based application of a first-order phase-model Eq. (2.3) the functional link would be erroneously identified as a weak structural link.

Second, a viable benefit of high-order phase coupling reconstruction is the ability to analyse high-order states of synchronization in computationally less costly models based on phase. For example, in quadruple synchronous states, the phase differences $m_1\varphi_1 + m_2\varphi_2 + m_3\varphi_3 + m_4\varphi_4 =$const. (Here all $m_j \in \mathbb{Z}$ whereas in Eq. (1.8) $n, m \in \mathbb{N}$.) While in experiments these states are detectable using the generalised version of the phase locking value Eq. (1.8), an offline analytic examination of such effects would be beneficial once a phase model is reconstructed from data [156].

This conquest however, relies on a determination of the phase dynamics. Moreover, while the interaction chains in a model can be infinitely long, experimental shortcomings prevent a complete reconstruction. Effectively this means that a finite horizon of interaction is present behind which influences are not detectable. For example, in a triplet phase model ① ↔ Ⓐ ↔ ② the interaction between oscillators ① and ② arises either directly or through all possible two-link combinations over an intermediate oscillator Ⓐ. Instead, in a quadruplet analysis, chains ① ↔ Ⓐ ↔ Ⓑ ↔ ② with an additional oscillator Ⓑ are considered. It can be readily seen that such analysis soon faces combinatorial divergences such that lowest high-order chains are practically considered [157, 158, 159].

2.2 A network of Stuart-Landau oscillators

A standard model for non-linear oscillations close to a Hopf[2] bifurcation is the SL system. In dimensional form it is given by

$$\tilde{a}_k' = (\mu_k + i\nu_k)\tilde{a}_k - (\tilde{\beta}_k + i\gamma_k)|\tilde{a}_k|^2\tilde{a}_k + \epsilon G_k(\tilde{a}_k, \tilde{a}_1, \ldots) \ , \tag{2.5}$$

where $G_k(\tilde{a}_k, \tilde{a}_1, \ldots)$ is the coupling function of each individual unit depending on the states of other elements in the network. A dimensionless form of Eq. (2.5) derives from local parameters: First, all amplitudes $a_k = \sqrt{\tilde{\beta}_k/\mu_k}\tilde{a}_k$ are normalised such that on the limit cycle their modulus is $|a_k| = 1$ (see Eq. (2.14)). Second, for the scaling of time it appears convenient to assume that the growth rate of linear oscillations, μ, is the same for all oscillators as this scaling acts on all units: $t = \mu\tau$. The resulting equation is

$$\dot{a}_k = (1 + i\omega_k)a_k - |a_k|^2 a_k - i\alpha_k a_k(|a_k|^2 - 1) + \varepsilon G_k(a_k, a_1, \ldots) \ . \tag{2.6}$$

Here $\omega_k = \nu_k/\mu - \gamma_k/\tilde{\beta}_k$ is the dimensionless frequency of the oscillation. The parameter $\alpha_k = \gamma_k/\tilde{\beta}_k$ determines the inclination of isochrones at the limit cycle and is a measure of non-isochronicity. The dimensionless coupling parameter ε depends on the scaling of the functions $G_k(\tilde{a}_k, \tilde{a}_1, \ldots)$: If only first powers of the amplitudes $\tilde{a}_j(t)$ enter the coupling functions, then $\varepsilon = \epsilon/\mu$.

In polar notation, $a_k(t) = r_k(t)\exp(i\theta_k(t))$, the dynamics is given by

$$\begin{aligned} \dot{r}_k &= r_k - r_k^3 + \varepsilon\Re[\exp(-i\theta_k)G_k(r_k, \theta_k, r_1, \theta_1, \ldots)] \ , & (2.7) \\ \dot{\theta}_k &= \omega_k - \alpha_k(r_k^2 - 1) + \varepsilon r_k^{-1}\Im[\exp(-i\theta_k)G_k(r_k, \theta_k, r_1, \theta_1, \ldots)] \ . & (2.8) \end{aligned}$$

From this representation, it can be seen that, $\theta_k(t)$ in the unperturbed system grows not uniformly. However, a phase

$$\varphi_k(t) = \theta_k(t) - \alpha_k \ln[r_k(t)] \tag{2.9}$$

can be derived that takes explicitly into account the form of isochrones, given by logarithmic curves. Using this relation, the dynamic Eq. (2.7) and (2.8) in terms of $r(t), \varphi(t)$ is:

$$\begin{aligned} \dot{r}_k &= r_k - r_k^3 + \varepsilon\Re[\exp(-i(\varphi_k + \alpha_k\ln[r_k]))G_k(r_k, \varphi_k, r_1, \varphi_1, \ldots)] \ , & (2.10) \\ \dot{\varphi}_k &= \omega_k + \frac{\varepsilon}{r_k}\Big[\Im[\exp(-i(\varphi_k + \alpha\ln[r_k]))G_k(r_k, \varphi_k, r_1, \varphi_1, \ldots)] \\ &\qquad -\alpha\Re[\exp(-i(\varphi_k + \alpha\ln[r_k]))G(r_k, \varphi_k, r_1, \varphi_1, \ldots)]\Big] \ . & (2.11) \end{aligned}$$

Here and in the following, it is $\alpha_k = \alpha$ the same for all units.

---

[2] Eberhard F. F. Hopf (1902-1983) [160]

2.3 High-order reduction and perturbation method - an example

In the following, the perturbation procedure for determination of a phase-only representation Eq. (2.4) of a network of SL oscillators is discussed. The coupling structure of the network is 1 ↔ 2 ↔ 3 what leads to dynamical equations in the form (2.6):

$$\begin{aligned}
\dot{a}_1 &= (1+i\omega_1)a_1 - |a_1|^2 a_1 - i\alpha a_1(|a_1|^2-1) + \varepsilon c_{2,1}\exp(i\beta_{2,1})a_2 \ , \\
\dot{a}_2 &= (1+i\omega_2)a_2 - |a_2|^2 a_2 - i\alpha a_2(|a_2|^2-1) + \varepsilon\Big[c_{1,2}\exp(i\beta_{1,2})a_1 + c_{3,2}\exp(i\beta_{3,2})a_3\Big] \ , \\
\dot{a}_3 &= (1+i\omega_3)a_3 - |a_3|^2 a_3 - i\alpha a_3(|a_3|^2-1) + \varepsilon c_{2,3}\exp(i\beta_{2,3})a_2 \ .
\end{aligned} \tag{2.12}$$

Here, additive coupling is considered with phase lag parameters $\beta_{j,k}$. Using polar coordinates and the phase definition Eq. (2.9), it follows

$$\begin{aligned}
\dot{r}_1 &= r_1 - r_1^3 + \varepsilon c_{2,1} r_2\cos(\theta_2-\theta_1+\beta_{2,1}) \ , \\
\dot{r}_2 &= r_2 - r_2^3 + \varepsilon c_{1,2} r_1\cos(\theta_1-\theta_2+\beta_{1,2}) + \varepsilon c_{3,2} r_3\cos(\theta_3-\theta_2+\beta_{3,2}) \ , \\
\dot{r}_3 &= r_3 - r_3^3 + \varepsilon c_{2,3} r_2\cos(\theta_2-\theta_3+\beta_{2,3}) \ , \\
\dot{\varphi}_1 &= \omega_1 + \varepsilon c_{2,1}\frac{r_2}{r_1}[\sin(\theta_2-\theta_1+\beta_{2,1}) - \alpha\cos(\theta_2-\theta_1+\beta_{2,1})] \ , \\
\dot{\varphi}_2 &= \omega_2 + \varepsilon c_{1,2}\frac{r_1}{r_2}[\sin(\theta_1-\theta_2+\beta_{1,2}) - \alpha\cos(\theta_1-\theta_2+\beta_{1,2})] \\
&\quad + \varepsilon c_{3,2}\frac{r_3}{r_2}[\sin(\theta_3-\theta_2+\beta_{3,2}) - \alpha\cos(\theta_3-\theta_2+\beta_{3,2})] \ , \\
\dot{\varphi}_3 &= \omega_3 + \varepsilon c_{2,3}\frac{r_2}{r_3}[\sin(\theta_2-\theta_3+\beta_{2,3}) - \alpha\cos(\theta_2-\theta_3+\beta_{2,3})] \ .
\end{aligned} \tag{2.13}$$

It can be seen that this dynamics is invariant under phase shifts as there appear only phase differences in the interaction terms. It represents a natural generalisation of the Kuramoto-Daido-type model Eq. (1.7) for dynamics off the limit cycle. Similarly, the additive coupling might be replaced by diffusive coupling. In this case however, the resultant phase dynamics overcomplicates significantly and will contain terms of self-coupling.

2.3.1 General perturbation approach

The algebraic approximation of the high-order phase coupling hierarchy Eq. (2.4) is complemented by a perturbative series

$$r(\boldsymbol{\varphi}) = 1 + \varepsilon r^{(1)}(\boldsymbol{\varphi}) + \varepsilon^2 r^{(2)}(\boldsymbol{\varphi}) + \dots \tag{2.14}$$

for the amplitude. Herein $r^{(1,2,\dots)}(\boldsymbol{\varphi})$ are the high-order corrections of the amplitude. The approach exploits the idea that the perturbation $\delta\mathbf{y}(t)$ should remain enslaved to the phase dynamics in a certain range of coupling strength.

Inserting both, Eq. (2.4) and Eq. (2.14) into Eqs. (2.10) and (2.11) allows to determine the full dependence of the phase dynamics on system parameters for each power of ε and the functional dependence of the coupling function on phases. For illustration, the first two steps of the perturbation method are shown here in full detail for the SL system while third and fourth order couplings are discussed only partly due to the rapid increase of computational complexity.

In Eq. (2.11), the first-order approximation $Q_k^{(1)}(\boldsymbol{\varphi})$, follows from leading order terms in Eq. (2.14):

$$Q_k^{(1)}(\boldsymbol{\varphi}) = \Im[\exp(-i\varphi_k)G_k(\varphi_k, 1, \varphi_1, 1, \ldots)] - \alpha\Re[\exp(-i\varphi_k)G_k(\varphi_k, 1, \varphi_1, 1, \ldots)] \ .$$

This result is equivalent to the phase model Eq. (1.6) (see also Sec. 5.1 where it is reconstructed from data).

Next, the first-order correction of the amplitude is obtained by substitution of Eq. (2.14) into Eq. (2.10):

$$\dot{r}_k^{(1)} = -2r_k^{(1)} + \Re[\exp(-i\varphi_k)Q_k^{(1)}(\boldsymbol{\varphi})] \ ,$$

where the time derivative of $r_k^{(1)}(\boldsymbol{\varphi})$ follows from

$$\dot{r}_k^{(1)} = \frac{\partial r_k^{(1)}}{\partial \varphi_k}\dot{\varphi}_k + \frac{\partial r_k^{(1)}}{\partial \varphi_1}\dot{\varphi}_1 + \ldots \approx \frac{\partial r_k^{(1)}}{\partial \varphi_k}\omega_k + \frac{\partial r_k^{(1)}}{\partial \varphi_1}\omega_1 + \ldots \ . \tag{2.15}$$

Thus, the problem of determining first-order corrections to the amplitude reduces to the partial differential equation

$$\begin{aligned} &2r_k^{(1)} + \frac{\partial r_k^{(1)}}{\partial \varphi_k}\omega_k + \frac{\partial r_k^{(1)}}{\partial \varphi_1}\omega_1 + \ldots = \Re[\exp(-i\varphi_k)Q_k^{(1)}(\boldsymbol{\varphi})] \\ &= \sum_{m_k, m_1, \ldots} g_{k;m_k m_1 \ldots} \exp(i(m_k\varphi_k + m_1\varphi_1 + \ldots)) \ . \end{aligned} \tag{2.16}$$

The second equality exploits the fact that all coupling functions are periodic on the $\boldsymbol{\varphi}$-torus. The same holds for $r_k^{(1)}(\boldsymbol{\varphi})$:

$$r_k^{(1)}(\boldsymbol{\varphi}) = \sum_{m_k, m_1, \ldots} \rho_{k;m_k m_1 \ldots} \exp(i(m_k\varphi_k + m_1\varphi_1 + \ldots)) \ .$$

Both series expansions yield an expression for the Fourier coefficients of $r_k^{(1)}(\boldsymbol{\varphi})$

$$\rho_{k;m_k m_1 \ldots} = \frac{g_{k;m_k m_1 \ldots}}{2 + i(m_k\omega_k + m_1\omega_1 + \ldots)} \ . \tag{2.17}$$

In the next step, $Q^{(2)}(\boldsymbol{\varphi})$ emanates from substitution of the expressions for $r_k^{(1)}(\boldsymbol{\varphi}), r_1^{(1)}(\boldsymbol{\varphi})$, … into Eq. (2.11) and in even further stages of expansion, the equations for $r_k^{(2)}(\boldsymbol{\varphi})$ are partial differential equations of type (2.16) and contain also first order corrections of amplitudes and phases.

2.3.2 Small parameter expansion.

To suppress the explicit dependence of the coupling function on radii in Eq. (2.13), angles $\theta_k(t)$ and the ratios $r_j(t)/r_k(t)$ have to be expressed in terms of $\varphi_k(t)$ and the amplitude corrections to radii $r_{k,j}(t)$ using Eqs. (2.9) and (2.14) [161]. The resulting phase-dynamics equations up to third order ε^3 are

$$\begin{aligned}
\dot{\varphi}_1 &= \omega_1 + \varepsilon c_{2,1}[\sin(\varphi_2 - \varphi_1 + \beta_{2,1}) - \alpha\cos(\varphi_2 - \varphi_1 + \beta_{2,1})] \\
&\quad + \varepsilon^2 c_{2,1}(1+\alpha^2)\sin(\varphi_2 - \varphi_1 + \beta_{2,1})(r_2^{(1)} - r_1^{(1)}) \\
&\quad + \varepsilon^3 c_{2,1}(1+\alpha^2)\Big[\Big(r_2^{(2)} - r_1^{(2)} - r_2^{(1)}r_1^{(1)} + (r_1^{(1)})^2\Big)\sin(\varphi_2 - \varphi_1 + \beta_{2,1}) \\
&\quad + \alpha\Big((r_1^{(1)})^2/2 + (r_2^{(1)})^2/2 - r_2^{(1)}r_1^{(1)}\Big)\cos(\varphi_2 - \varphi_1 + \beta_{2,1})\Big] + \dots\ , \\
\dot{\varphi}_2 &= \omega_2 + \varepsilon c_{1,2}[\sin(\varphi_1 - \varphi_2 + \beta_{1,2}) - \alpha\cos(\varphi_1 - \varphi_2 + \beta_{1,2})] \\
&\quad + \varepsilon c_{3,2}[\sin(\varphi_3 - \varphi_2 + \beta_{3,2}) - \alpha\cos(\varphi_3 - \varphi_2 + \beta_{3,2})] \\
&\quad + \varepsilon^2 c_{1,2}(1+\alpha^2)\sin(\varphi_1 - \varphi_2 + \beta_{1,2})(r_1^{(1)} - r_2^{(1)}) \\
&\quad + \varepsilon^2 c_{3,2}(1+\alpha^2)\sin(\varphi_3 - \varphi_2 + \beta_{3,2})(r_3^{(1)} - r_2^{(1)}) \\
&\quad + \varepsilon^3 c_{1,2}(1+\alpha^2)\Big[\Big(r_1^{(2)} - r_2^{(2)} - r_1^{(1)}r_2^{(1)} + (r_2^{(1)})^2\Big)\sin(\varphi_1 - \varphi_2 + \beta_{1,2}) \\
&\quad + \alpha\Big((r_2^{(1)})^2/2 + (r_1^{(1)})^2/2 - r_1^{(1)}r_2^{(1)}\Big)\cos(\varphi_1 - \varphi_2 + \beta_{1,2})\Big] \\
&\quad + \varepsilon^3 c_{3,2}(1+\alpha^2)\Big[\Big(r_3^{(2)} - r_2^{(2)} - r_3^{(1)}r_2^{(1)} + (r_2^{(1)})^2\Big)\sin(\varphi_3 - \varphi_2 + \beta_{3,2}) \\
&\quad + \alpha\Big((r_2^{(1)})^2/2 + (r_3^{(1)})^2/2 - r_3^{(1)}r_2^{(1)}\Big)\cos(\varphi_3 - \varphi_2 + \beta_{3,2})\Big] + \dots\ , \\
\dot{\varphi}_3 &= \omega_3 + \varepsilon c_{2,3}[\sin(\varphi_2 - \varphi_3 + \beta_{2,3}) - \alpha\cos(\varphi_2 - \varphi_3 + \beta_{2,3})] \\
&\quad + \varepsilon^2 c_{2,3}(1+\alpha^2)\sin(\varphi_2 - \varphi_3 + \beta_{2,3})(r_2^{(1)} - r_3^{(1)}) \\
&\quad + \varepsilon^3 c_{2,3}(1+\alpha^2)\Big[\Big(r_2^{(2)} - r_3^{(2)} - r_2^{(1)}r_3^{(1)} + (r_3^{(1)})^2\Big)\sin(\varphi_2 - \varphi_3 + \beta_{2,3}) \\
&\quad + \alpha\Big((r_3^{(1)})^2/2 + (r_2^{(1)})^2/2 - r_2^{(1)}r_3^{(1)}\Big)\cos(\varphi_2 - \varphi_3 + \beta_{2,3})\Big] + \dots\ .
\end{aligned} \tag{2.18}$$

These equations already correspond to the representation given in Eq. (2.4) but they still depend on radial corrections $r_{k,j}^{(1,2)}(\boldsymbol{\varphi})$ which have to be obtained from the perturbed radius equations. As an example, for $r_1^{(1,2)}(\boldsymbol{\varphi})$:

$$\begin{aligned}
\dot{r}_1^{(1)} &= \omega_1\frac{\partial r_1^{(1)}}{\partial\varphi_1} + \omega_2\frac{\partial r_1^{(1)}}{\partial\varphi_2} + \omega_3\frac{\partial r_1^{(1)}}{\partial\varphi_3} + 2r_1^{(1)} = c_{2,1}\cos(\varphi_2 - \varphi_1 + \beta_{2,1})\ , \\
\dot{r}_1^{(2)} &= \omega_1\frac{\partial r_1^{(2)}}{\partial\varphi_1} + \omega_2\frac{\partial r_1^{(2)}}{\partial\varphi_2} + \omega_3\frac{\partial r_1^{(2)}}{\partial\varphi_3} + 2r_1^{(2)} = -3(r_1^{(1)})^2 \\
&- \alpha c_{2,1}(r_2^{(1)} - r_1^{(1)})\sin(\varphi_2 - \varphi_1 + \beta_{2,1}) + c_{2,1}r_2^{(1)}\cos(\varphi_2 - \varphi_1 + \beta_{2,1}) \\
&+ c_{2,1}[\sin(\varphi_2 - \varphi_1 + \beta_{2,1}) - \alpha\cos(\varphi_2 - \varphi_1 + \beta_{2,1})]\frac{\partial r_1^{(1)}}{\partial\varphi_1} \\
&+ \Big[c_{1,2}[\sin(\varphi_1 - \varphi_2 + \beta_{1,2}) - \alpha\cos(\varphi_1 - \varphi_2 + \beta_{1,2})] \\
&+ c_{3,2}[\sin(\varphi_3 - \varphi_2 + \beta_{3,2}) - \alpha\cos(\varphi_3 - \varphi_2 + \beta_{3,2})]\Big]\frac{\partial r_1^{(1)}}{\partial\varphi_2} \\
&+ c_{2,3}[\sin(\varphi_2 - \varphi_3 + \beta_{2,3}) - \alpha\cos(\varphi_2 - \varphi_3 + \beta_{2,3})]\frac{\partial r_1^{(1)}}{\partial\varphi_3}\ .
\end{aligned} \tag{2.19}$$

Qualitatively similar results are obtained for the other two oscillators.

A solution to the radial equations for $r^{(1,2)}_{k,j}(\boldsymbol{\varphi})$ exploits the 2π-periodicity of radii and $Q^{(1,2,\dots)}_{k,j}(\boldsymbol{\varphi})$. Thus, application of Eq. (2.17) results in the first-order radial corrections:

$$\begin{aligned}
r^{(1)}_1 &= \frac{2c_{2,1}}{4+(\omega_2-\omega_1)^2}\cos(\varphi_2-\varphi_1+\beta_{2,1}) + \frac{(\omega_2-\omega_1)c_{2,1}}{4+(\omega_2-\omega_1)^2}\sin(\varphi_2-\varphi_1+\beta_{2,1}) \ , \\
r^{(1)}_2 &= \frac{2c_{1,2}}{4+(\omega_1-\omega_2)^2}\cos(\varphi_1-\varphi_2+\beta_{1,2}) + \frac{(\omega_1-\omega_2)c_{1,2}}{4+(\omega_1-\omega_2)^2}\sin(\varphi_1-\varphi_2+\beta_{1,2}) \\
&+ \frac{2c_{3,2}}{4+(\omega_3-\omega_2)^2}\cos(\varphi_3-\varphi_2+\beta_{3,2}) + \frac{(\omega_3-\omega_2)c_{3,2}}{4+(\omega_3-\omega_2)^2}\sin(\varphi_3-\varphi_2+\beta_{3,2}) \ , \\
r^{(1)}_3 &= \frac{2c_{2,3}}{4+(\omega_2-\omega_3)^2}\cos(\varphi_2-\varphi_3+\beta_{2,3}) + \frac{(\omega_2-\omega_3)c_{2,3}}{4+(\omega_2-\omega_3)^2}\sin(\varphi_2-\varphi_3+\beta_{2,3}) \ .
\end{aligned} \tag{2.20}$$

Finally, substitution into Eq. (2.18) defines the second-order phase reduction and yields a phase-only representation of the coupling:

$$\begin{aligned}
\dot{\varphi}_1 &= \omega_1 + \varepsilon c_{2,1}[\sin(\varphi_2-\varphi_1+\beta_{2,1}) - \alpha\cos(\varphi_2-\varphi_1+\beta_{2,1})] \\
&+ \varepsilon^2\Big[a^{(2)}_{1;0,0,0} + a^{(2)}_{1;-2,2,0}\cos(2\varphi_2-2\varphi_1) + b^{(2)}_{1;-2,2,0}\sin(2\varphi_2-2\varphi_1) \\
&+ a^{(2)}_{1;-1,2,-1}\cos(2\varphi_2-\varphi_1-\varphi_3) + b^{(2)}_{1;-1,2,-1}\sin(2\varphi_2-\varphi_1-\varphi_3) \\
&+ a^{(2)}_{1;-1,0,1}\cos(\varphi_3-\varphi_1) + b^{(2)}_{1;-1,0,1}\sin(\varphi_3-\varphi_1)\Big] \ ,
\end{aligned} \tag{2.21}$$

$$\begin{aligned}
\dot{\varphi}_2 &= \omega_2 + \varepsilon c_{1,2}[\sin(\varphi_1-\varphi_2+\beta_{1,2}) - \alpha\cos(\varphi_1-\varphi_2+\beta_{1,2})] \\
&+ \varepsilon c_{3,2}[\sin(\varphi_3-\varphi_2+\beta_{3,2}) - \alpha\cos(\varphi_3-\varphi_2+\beta_{3,2})] \\
&+ \varepsilon^2\Big[a^{(2)}_{2;0,0,0} + a^{(2)}_{2;2,-2,0}\cos(2\varphi_1-2\varphi_2) + b^{(2)}_{2;2,-2,0}\sin(2\varphi_1-2\varphi_2) \\
&+ a^{(2)}_{2;0,-2,2}\cos(2\varphi_3-2\varphi_2) + b^{(2)}_{2;0,-2,2}\sin(2\varphi_3-2\varphi_2) \\
&+ a^{(2)}_{2;-1,2,-1}\cos(2\varphi_2-\varphi_1-\varphi_3) + b^{(2)}_{2;-1,2,-1}\sin(2\varphi_2-\varphi_1-\varphi_3) \\
&+ a^{(2)}_{2;1,0,-1}\cos(\varphi_1-\varphi_3) + b^{(2)}_{2;1,0,-1}\sin(\varphi_1-\varphi_3)\Big] \ ,
\end{aligned} \tag{2.22}$$

$$\begin{aligned}
\dot{\varphi}_3 &= \omega_3 + \varepsilon c_{2,3}[\sin(\varphi_2-\varphi_3+\beta_{2,3}) - \alpha\cos(\varphi_2-\varphi_3+\beta_{2,3})] \\
&+ \varepsilon^2\Big[a^{(2)}_{3;0,0,0} + a^{(2)}_{3;0,2,-2}\cos(2\varphi_2-2\varphi_3) + b^{(2)}_{3;0,2,-2}\sin(2\varphi_2-2\varphi_3) \\
&+ a^{(2)}_{3;-1,2,-1}\cos(2\varphi_2-\varphi_3-\varphi_1) + b^{(2)}_{3;-1,2,-1}\sin(2\varphi_2-\varphi_3-\varphi_1) \\
&+ a^{(2)}_{3;1,0,-1}\cos(\varphi_1-\varphi_3) + b^{(2)}_{3;1,0,-1}\sin(\varphi_1-\varphi_3)\Big] \ .
\end{aligned} \tag{2.23}$$

These equations are the main result of the perturbative phase-reduction. The coefficients of the second-order coupling terms, denoted in Eqs. (2.21-2.23) by $a^{(2)}_{k;\mathbf{l}}, b^{(2)}_{k;\mathbf{l}}$, are listed in Tab. A.3, A.4 and A.5. Here, $\mathbf{l} = (l_1, l_2, l_3)$ denotes terms with the combination of the phases $l_1\varphi_1 + l_2\varphi_2 + l_3\varphi_3$. Phase dependence of order ε^3 and ε^4 of the coupling are listed in in Tab. A.6 (without coupling coefficients)[3].

It can be readily seen that indeed, the phase coupled networks has specific properties that reach beyond the first-order phase dynamics and beyond the structural coupling formulation Eq. (2.12). The physical meaning of the obtained terms is as follows:

---

[3] For estimation of these modes it suffices to consider the perturbative orders in a generic form. Then, using a generic trigonometric function $g(\varphi_j - \varphi_k)$ of the phase differences gives the result. For example: $g(\varphi_2-\varphi_3)r^{(1)}(\varphi_1,\varphi_2) \mapsto (-1,2,-1) \cup (1,0,-1)$.

- Corrections to the first-order coupling modes appears in order ε^3. Similarly, the second order contributes to a correction of the natural frequency. The performed coupling estimation up to ε^4 suggests that generally odd coupling orders contribute to correction of first-order modes and that even coupling orders contribute to the correction of the base frequency.

- There appear pairwise terms similar to the well known Kuramoto-Daido coupling, having frequency differences as a multiple of the coupling order. For φ_1: $\varepsilon \to \varphi_2 - \varphi_1$, $\varepsilon^2 \to 2\varphi_2 - 2\varphi_1$, $\varepsilon^3 \to 3\varphi_2 - 3\varphi_1$, etc. . These high-order resonant terms appear also in a pair of coupled oscillators and the first harmonics resembles the basic Kuramoto-coupling term.

- Terms containing combinations of all three phases, e.g., $\sim \sin(2\varphi_2 - \varphi_1 - \varphi_3)$, mean that an effective hyper-network with non-pairwise coupling appears already in the second-order reduction. These terms become more complicated in higher order of the coupling.

- Terms containing phase differences for not directly coupled oscillators (e.g., the term $\sim \sin(\varphi_3 - \varphi_1)$ on the r.h.s. of the equation for $\dot{\varphi}_1$) indicate that connections in the network of phases do not coincide with the structural connections in the state-space formulation Eq. (2.12).

- While the first-order coupling terms are frequency-independent, the second-order terms (and presumably all higher order terms) depend explicitly on frequency differences. In a more general setting the coupling depends on the frequencies themselves (see results for the VdP system in Sec. 2.4.3).

2.4 Numerical high-order phase reduction for a network

The SL oscillator represents an exceptional case, where the isochrones are known and thus, a full phase reduction is formally possible. However, the upper analysis for the relatively simple SL dynamics underlines that such an analysis might become very complicated. Furthermore, for most of the other oscillators, phase equations in a tractable closed form do not exist and have to be obtained numerically based on accurate estimates of phases $\boldsymbol{\varphi}(t)$ and frequencies $\dot{\boldsymbol{\varphi}}(t)$.

In such generic situations, by exploiting the 2π-periodicity of the phase coupling functions and the phase derivative $\dot{\varphi}_k(\boldsymbol{\varphi})$, it is possible to implement a powerful network-inference tool based on a M-dimensional Fourier series representation:

$$\dot{\varphi}_k(\boldsymbol{\varphi}) = \dot{\varphi}_k^{(f)}(\boldsymbol{\varphi}) := A_{k;\mathbf{0}} + \sum_{|\mathbf{l}|=1}^{\infty} \left[A_{k;\mathbf{l}} \cos(\boldsymbol{\varphi} \cdot \mathbf{l}) + B_{k;\mathbf{l}} \sin(\boldsymbol{\varphi} \cdot \mathbf{l})\right] \; . \tag{2.24}$$

Here $\mathbf{l} = (l_1, l_2, \ldots, l_N)$ is the M-dimensional vector of modes present in the phase derivative, $\dot{\varphi}_k^{(f)}(\boldsymbol{\varphi})$. The latter is obtained from optimal fit of Eq. (2.24) through a minimization

$$\left\langle \left(\dot{\varphi}_k(\boldsymbol{\varphi}) - \dot{\varphi}_k^{(f)}(\boldsymbol{\varphi})\right)^2 \right\rangle \to \min \; . \tag{2.25}$$

The given theoretic analysis illustrates that one and the same mode contains corrections from many perturbation orders. Generally this means that the optimal coefficients of the series Eq. (2.24) are related to the true, theoretic model coefficients through

$$A_{k;\mathbf{l}}(\varepsilon) = a^{(0)}_{k;\mathbf{l}} + \varepsilon a^{(1)}_{k;\mathbf{l}} + \varepsilon^2 a^{(2)}_{k;\mathbf{l}} \dots , \qquad B_{k;\mathbf{l}}(\varepsilon) = \varepsilon b^{(1)}_{k;\mathbf{l}} + \varepsilon^2 b^{(2)}_{k;\mathbf{l}} \dots . \tag{2.26}$$

This allows to reconstruct the different coupling orders from polynomial fitting over a range of values ε.

Thus, direct numerical reconstruction of the phase-network interactions is achieved in three steps here:

(I) Calculation of the true phases $\boldsymbol{\varphi}(t)$ and the frequencies $\dot{\boldsymbol{\varphi}}(t)$ from the full model

(II) Reconstruction of the coupling coefficients $A_{k;\mathbf{l}}$ and $B_{k;\mathbf{l}}$ based on optimal numerical fitting

(III) Polynomial fit of $A_{k;\mathbf{l}}(\varepsilon)$ and $B_{k;\mathbf{l}}(\varepsilon)$ or $\mathcal{H}_{k;\mathbf{l}}(\varepsilon) = \sqrt{A^2_{k;\mathbf{l}}(\varepsilon) + B^2_{k;\mathbf{l}}(\varepsilon)}$ for many values of ε to obtain the model coefficients $a^{(1,2,\dots)}_{k;\mathbf{l}}$ and $b^{(1,2,\dots)}_{k;\mathbf{l}}$

Notably, the three upper steps can be performed for data driven estimates of the phases as well. Thus, a question of great practical relevance is, whether the procedure is actually able to reconstruct high-order terms at all, i. e. in the optimal situation, where true phase and frequency are known (see for an example Sec. 7.1).

2.4.1 Direct numerical phase estimation

In the following, the procedure for phase and frequency estimation based on full knowledge of a state space trajectory $\mathbf{y}_k(t)$ and its time evolution Eq. (2.1) is presented.

The approach makes use of the autonomous period T of the unperturbed system ($\varepsilon = 0$). For estimation of T, the (unperturbed) system is started from an arbitrary point $\mathbf{Y}$ on the limit cycle to which a phase of $\varphi = 0$ is assigned; the return time to this point is T. Thus, for any other point on the cycle the time $\tau_l(\mathbf{Y}(t))$ required to reach $\varphi(T) = 2\pi$ defines the true phase as on the cycle, $\varphi(t) = \varphi(\mathbf{Y}(t)) = 2\pi(T - \tau_l(\mathbf{Y}(t)))/T$.

To find the phase and its derivative also for an arbitrary point $\mathbf{u} = \mathbf{y}(t)$ and derivatives $\mathbf{v} = \dot{\mathbf{u}}$ in the basin of attraction, an unperturbed auxiliary system

$$\dot{\mathbf{w}} = \mathbf{F}(\mathbf{w}) , \tag{2.27}$$

is started from the initial conditions $\mathbf{w}(0) = \mathbf{u}$ and evolved for nT time units such that the state $\mathbf{w}(nT) = \bar{\mathbf{w}}$ is very close to the limit cycle of the system. As a consequence of the stroboscopic observation only at full periods, all the points, including $\bar{\mathbf{w}}$ will have the same value of phase. This means $\varphi(\mathbf{u})$ can be easily computed as described before and is given by $\varphi(\mathbf{u}) = \varphi(\mathbf{w}(0)) = \varphi(\bar{\mathbf{w}}) = 2\pi(T - \tau_l(\bar{\mathbf{w}}))/T$.

Similarly, the phase derivative is computed from autonomous evolution of the initial condition $\mathbf{u}+\mathbf{v}dt$: Since the time step, dt, is (infinitely) small, this can be done by tracing the linearised dynamics of $\mathbf{v}dt$ to $\bar{\mathbf{v}}dt$ within time interval nT. This linear dynamics derives from the Jacobian of the original equations (2.27). Thus, after relaxation, the systems states are given by $\bar{\mathbf{w}}$ and $\bar{\mathbf{w}} + \bar{\mathbf{v}}dt$ on the cycle of the autonomous dynamics Eq. (2.27) with phases φ and $\varphi + d\varphi$ respectively.

In contrast, starting the autonomous system at a state $\bar{\mathbf{w}}$ on the cycle and evolving it to $\bar{\mathbf{w}} + \bar{\mathbf{v}}dt = \bar{\mathbf{w}} + \mathbf{F}(\bar{\mathbf{w}})\bar{d}t$, it takes a time $\bar{d}t \neq dt$ to reach the new state. This yields a relation between both time steps: $\bar{d}t = dt\,(\bar{\mathbf{v}} \cdot \mathbf{F}(\bar{\mathbf{w}}))\,/||\mathbf{F}(\bar{\mathbf{w}})||^2$. Finally, since on the cycle, phase growth is given by the natural frequency $\omega = 2\pi/T$, $d\varphi = \omega d\bar{t}$ and the true phase derivative follows:

$$\frac{d\varphi}{dt} = \omega \frac{\bar{\mathbf{v}} \cdot \mathbf{F}(\bar{\mathbf{w}})}{\|\mathbf{F}(\bar{\mathbf{w}})\|^2} \,. \tag{2.28}$$

2.4.2 Comparison of numerics and analytic results

Here, an exemplary numerical analysis for an asynchronous SL dynamics Eq. (2.12) is presented and results are compared to the phase reduction theory of Sec. 2.3. The parameter values in the following example are: $\alpha = 0.1$, $\omega_1 = -\sqrt{5}/2$, $\omega_2 = (\sqrt{2}-1)/10$ and $\omega_3 = 0.8$. The coupling is specified by coupling constants $c_{j,k} = 1$ for $(j,k) \in \{(1,2),(2,1),(2,3),(3,2)\}$ and phase lags $\beta_{1,2} = 0.32$, $\beta_{2,1} = 0.44$, $\beta_{2,3} = 0.43$ and $\beta_{3,2} = 0.18$. These parameter ensure that the three oscillators remain asynchronous. An analysis for synchronous oscillators with a long transient is performed in [161].

The phase-frequency data is generated from Eq. (2.9). For this, 10^6 initial conditions with amplitude $r(\boldsymbol{\varphi}(0)) = 1$ (on the limit cycle) and uniformly distributed angles θ are generated. To ensure that the systems have settled to the invariant torus, an initial transient of 20 time units is chosen. This relaxation procedure is repeated for several coupling amplitudes ε.

Estimation of the mode coefficients in the Fourier representation of the coupling function is realised by least square fitting based on the singular-value decomposition routine of the `C++` library `EIGEN`. Modes with $|l_j| \le m = 4$ are determined here what accounts for an overall number of 729 fit parameters for each oscillators or 364 coupling constants $\mathcal{H}_{k;\mathbf{l}}(\varepsilon)$ and $A_{k;0}$. Similarly, since the considered SL system is invariant under phase shifts $\varphi_k \to \varphi_k + \delta\varphi$, only resonant modes with $l_1 + l_2 + \ldots + l_M = 0$ can exist. An analysis that takes just these modes into account is discussed in detail in [161] as well.

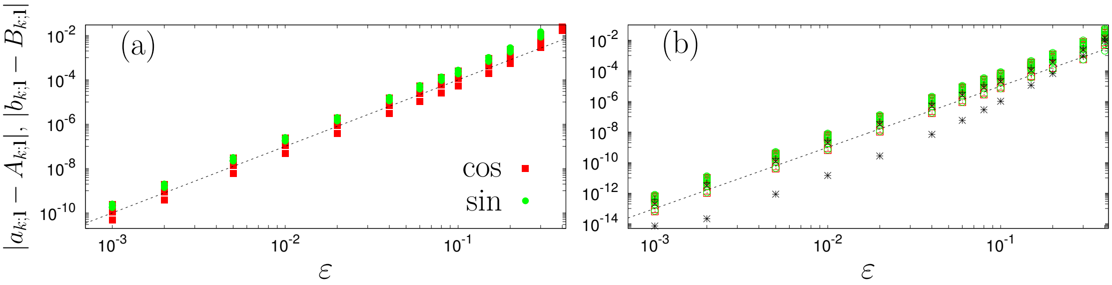

Figure 2.1: Shown are differences between numerical coupling coefficients and their theoretic predictions as a function of the coupling strength. Panel (a) depicts the residue for terms appearing in the first order of ε; the black dashed line here corresponds to $\sim \varepsilon^3$. Panel (b) presents the terms of second order in ε. Here the dashed line corresponds to $\sim \varepsilon^4$. Additional black markers indicate the difference of zero-order terms $A_{k;\mathbf{0}}$, $k = 1,2,3$ and their second-order correction.

In Fig. 2.1, differences of the second and first order coefficients in Eqs. (2.21-2.23) are shown (see Tabs. A.3 to A.5). It appears that for weak coupling the difference settles to the level of numerical precision while it rises to $\mathcal{O}(1)$ only for such strong coupling as $\varepsilon = 0.4$. Moreover, the difference for the first-order terms grows proportional to ε^3, in correspondence with the theoretical conclusion that no second-order correction to the

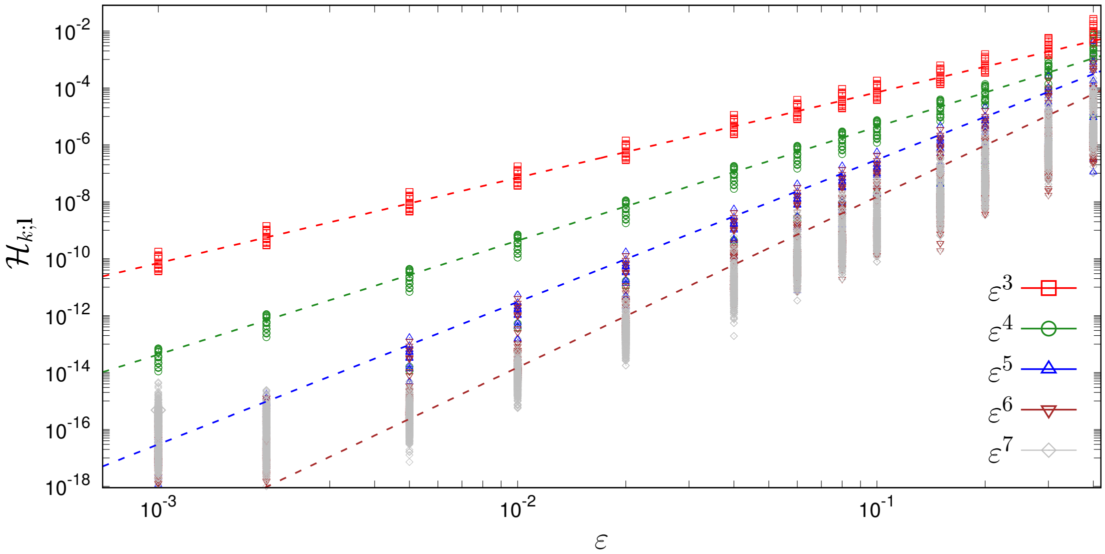

Figure 2.2: Shown are amplitudes for all coupling coefficients of orders larger than two for all three SL oscillators (Eq. (2.13)) in the asynchronous configuration. The dashed lines, from top to bottom, have slopes 3, 4, 5, and 6 in log-log coordinates. All coupling coefficients which scale at least as $\sim \varepsilon^7$ or higher are indicated with gray diamonds.

first-order terms exist. In summary, the numerical fitting indeed is able to regain the actual second-order phase dynamics model from phase-frequency data.

In Fig. 2.2 all other reconstructed Fourier coefficients are shown (see also Tab. A.6). For these modes no theoretic expression exists yet, but can be derived from perturbation theory in Sec. 2.3. In fact, it can be readily seen that many of these modes scale as ε^3, ε^4, ε^5 and ε^6 respectively and that their scaling laws are well separated. Only in sixths and higher orders, separation of different scalings is marginal.

2.4.3 Coupling reconstruction for a network of van-der-Pol oscillators

In this section a network of three non-identical VdP oscillators

$$\begin{aligned} \ddot{y}_1 - \mu(1-y_1^2)\dot{y}_1 + \omega_1^2 y_1 &= \varepsilon y_2 \\ \ddot{y}_2 - \mu(1-y_2^2)\dot{y}_2 + \omega_2^2 y_2 &= \varepsilon(y_1+y_3) \\ \ddot{y}_3 - \mu(1-y_3^2)\dot{y}_3 + \omega_3^2 y_3 &= \varepsilon y_2 \end{aligned} \tag{2.29}$$

illustrates the network reconstruction in a model where isochrones are defined implicitly. In such situation it still might be possible to find an explicit analytic approximation of the isochrones. However, such conquest is significantly more challenging such that at this point only a numerical analysis is performed.

Throughout this section, model parameters are fixed to $\mu = 1$ and $\omega_1 = 1$, $\omega_2 = 1.324715957$, $\omega_3 = \omega_2^2$. The time series of $\varphi_{1,2,3}(t)$ and $\dot{\varphi}_{1,2,3}(t)$ is obtained from a single trajectory of the network by means of the numerical procedure outlined in Sec. 2.4.1. The numerical integration of the system is performed for coupling strength up to $\varepsilon = 0.3$. For this coupling strength the network units are asynchronous. For each coupling parameter, 10^6 data points are collected. The Fourier series Eq. (2.24) is truncated at $|\mathbf{l}| \leq 4$.

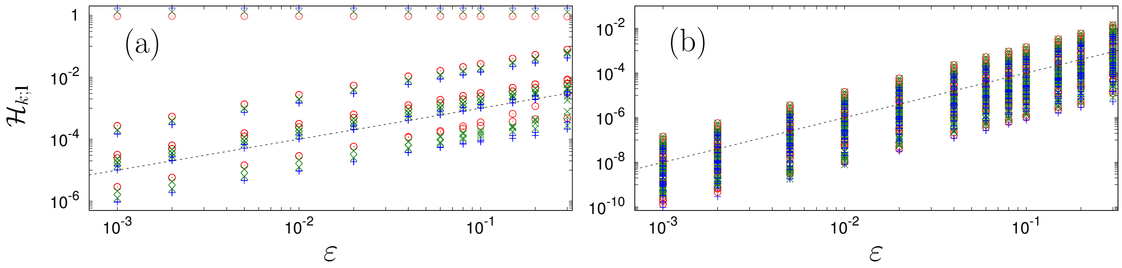

Figure 2.3: Coupling coefficients $\mathcal{H}_{k,1}$ for all three oscillators are shown by red circles, green crosses, and blue pluses, respectively, versus coupling strength ε. (a): Terms $\sim \varepsilon^0$, $\sim \varepsilon^1$; (b): Terms $\sim \varepsilon^2$. Dashed black lines correspond to the scaling $\sim \varepsilon$ and $\sim \varepsilon^2$ respectively.

According to the presented analysis above, coupling terms possess a leading dependence $\sim \varepsilon^q$, with $q = 0, 1, 2, \ldots$. Thus, in a preliminary step toward, visual analysis, a power law $\sim \varepsilon^q$ is fitted to the coefficients $\mathcal{H}_{k,1}(\varepsilon)$ to determine the order of coupling. If the fitted value q is close to an integer and the coefficient of determination is high the corresponding power is attributed to the coupling term. Moreover, for $\varepsilon^0, \varepsilon^1, \varepsilon^2$, the analysis is based on the five small values of $\varepsilon \in [0.001, 0.002, 0.005, 0.01, 0.02]$, while for powers ε^3 and ε^4 coupling constants at $\varepsilon \in [0.04, 0.06, 0.08, 0.1, 0.15]$ are considered.

Figure 2.3 illustrates the validity of the high-order phase reduction for the VdP oscillatory network. Coupling modes that appear in power of ε and ε^2 are listed in order of their amplitudes in Tab. A.9. Here, central observations about the related coupling are presented:

- It appears that in the first order, terms with phase differences and the terms with phase sums have effectively similar amplitudes and are thus indistinguishable in Fig. 2.3. This means that the coupling terms $\sim \varepsilon$ have nearly the Winfree-form[4] (Eqs. (2.3) and (1.6)). They are in full agreement with first-order theory.
- Because the variable $y_{1,2,3}(t)$ of the VdP network possess odd powers, terms with the third harmonics appear already in the first order coupling term.
- The number of terms listed in Tab. A.9 varies depending on the natural frequency of the oscillator. This is in clear contrast to the SL phase dynamics where only the differences of frequencies enter the coupling constants and the number of terms remains symmetric. This underlines that the coupling in the VdP system depends explicitly on frequency as it is also reported in [163].
- The higher orders of coupling depicted in Fig. 2.4 include many more modes. Within the explored size of the time series scaling behaviour up to ε^4 can be observed. Beyond this limit a separation of terms is hampered due to numerical inaccuracies.

Finally, some emphasis has to be put on a discussion of the reproducibility of the analysis results: Despite the fact that the theoretically expected scaling behaviour is found in coupling orders up to ε^6 (SL, see Fig. 2.2) and ε^4 (VdP, see Fig. 2.4(a,b)) respectively, the results in higher orders of coupling depend weakly on the numerical

---

[4] Arthur T. Winfree (1942-2002) [162]

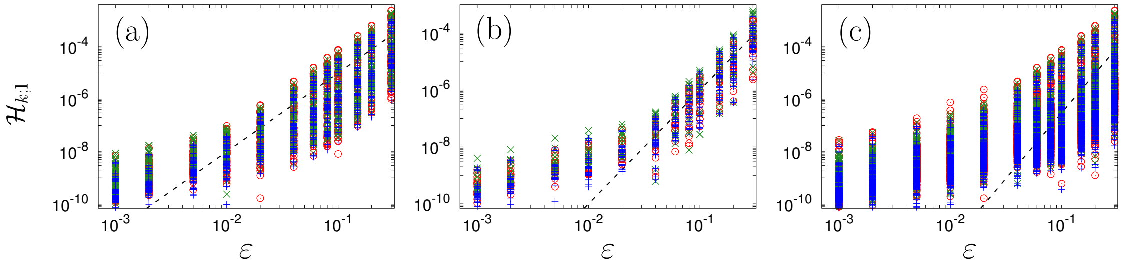

Figure 2.4: Coupling coefficients for powers 3 (a) and 4 (b). Panel (c) presents all other coefficients. Dashed black lines show powers 3, 4, and 5, respectively.

implementation of fitting. For example, in [161] the existence of spurious terms is reported while essentially no such terms are found in the analysis presented here. The only essential difference between the study and this text is the implementation of the minimisation Eq. (2.25). Moreover, a close inspection of Figs. 2.2 and 2.4 reveals some minor differences in the reconstructed coupling constants. All of these differences appear in already small terms and are most presumably unavoidable results of finite-size effects and numerical inaccuracies. Nevertheless, coupling reconstruction up to ε^2 shows good agreement in both models.

Chapter 3

Dynamic phase reconstruction

Heuristic modelling and mixed data-analysis methods based on a phase are in numerous studies realised by generic demodulation techniques for signals [164, 165, 138, 23]. These techniques are closely related to a spectral time-frequency analysis and are applicable to a wide range of oscillatory signals. In particular, for non-linear systems such methods deliver valuable insights as they are able to capture the time-varying complexity of observations.

In contrast, the specific task of *dynamic phase reconstruction*, i. e. reconstructing the asymptotic phase $\varphi(t)$ from an oscillatory signal demands for *dynamic* assumptions which take the theory outlined in Sec. 1.2 and Ch. 2 into account [166, 161]. However, while on the one hand, signals of limit cycle oscillations can still be non-stationary, on the other hand, generic data analysis methods, suitable for non-stationary signals, lead to erroneous results in terms of the theory of dynamical systems. Mainly, this is due to the fact that dynamic assumptions are not incorporated or due to generic shortcomings of a method.

3.1 Generic signal analysis

The oscillatory behaviour of a stationary signal[1] can be characterised in a meaningful way by its Fourier transform $\mathcal{F}_X(\omega)$ and its spectrum $|\mathcal{F}_X(\omega)|^2$. Thus, any 2π-periodic signal can be represented in the time domain by a linear combination of model functions that lead to the Fourier series. Frequency in terms of the Fourier transform thus, is defined as a functional argument related to the power of a given frequency, constant over time.

For non-stationary signals, a more general time-frequency analysis by means of the *windowed Fourier transform* (WFT)

$$\mathcal{F}_X(\omega, t) = \frac{1}{\sqrt{2\pi}} \int_{-\infty}^{\infty} X(\tau) W_{\delta t}(\tau - t) \exp[-i\omega\tau] d\tau \ . \tag{3.1}$$

or the *wavelet transform* (WT)

$$\mathcal{W}_X(\omega, t) = \int_{-\infty}^{\infty} X(\tau) \mathbb{W}(\tau - t, \omega) d\tau \ . \tag{3.2}$$

might be necessary. In both of these transformations, frequency becomes local in time through the introduction of a window function $W_{\delta t}(\tau - t)$ which selects only a portion of the whole time series. In both transformations, δt determines the width of the window and thus, how localised the spectral content is in time and frequency. Notably, for the WFT, δt is independent of the frequency what leads to a non-optimal resolution of the spectral content. In contrast, in the WT, δt is a function of frequency. It is chosen such that a WT has a convenient resolution in different frequency bands. The related

---

[1] The following work focusses on univariate data if not stated otherwise.

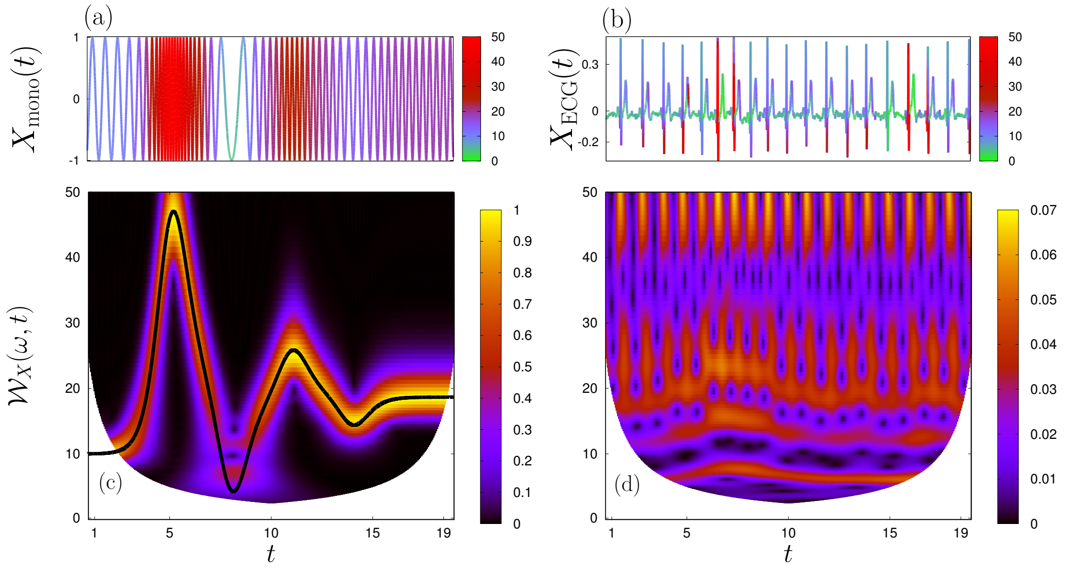

Figure 3.1: Depicted are two comparative examples for WT analysis based on the Gabor wavelet Eq. (3.3) with $f_c = 8$ and the Hilbert transform Eq. (3.8). Shown in (a) is the monocomponent signal $X_{\rm mono}(t) = \cos(\phi(t))$ where $\phi(t) = [0.03t + 2 + 3(1 + \tanh(2(t - 20))) + 3(1 + \tanh(2(t - 40))) + 5(1 + \tanh(2(t - 60)))]t/2 + 30\sin(0.02\sqrt{2}t)$. The corresponding frequency specrum in (c) shows a clear single-band double-spike structure with a roughly constant amplitude. The black line following the main ridge of the spectrum is the instantaneous frequency of $\theta^{(a)}$ Eq. (3.6) obtianed by the Hilbert transform of $X_{\rm mono}(t)$. The magnitude of $\dot{\theta}^{(a)}(t)$ is indicated by the colour code in (a) and is in clear correspondence to the periodicity of the signal. Shown in (b,d) are similar results for the ECG signal discussed in Sec. 1.1.3. The WT of the ECG shows a rich structure with three characteristic low-frequency bands between 1Hz and 3Hz corresponding to the cardiac beating cycle. In clear contrast, to (a,c), the Hilbert phase-analysis is unable to cover the spectral complexity of the full ECG. This is also indicated by the colour code in (b). This signal correspond to the embedding in Fig. 1.9 (c).

convolution kernel $\mathrm{W}(\tau - t, \omega)$ is termed *wavelet*. As an example, Fig. 3.1 shows the WT using the complex Gabor wavelet

$$\mathrm{W}(\tau - t, \omega) = W_{\delta t}(\tau - t)\exp(-i\omega\tau), \quad W_{\delta t(\omega)}(\tau - t) = \sqrt{\pi}\exp\left[(\tau - t)^2/\delta t^2(\omega)\right] . \quad (3.3)$$

For this type of wavelet, scale and frequencies are related through[2] $\omega = 2\pi f_c/\delta t$, where f_c determines the number of full oscillation periods under the window function [164].

For the spectral representation of $X_{\rm ECG}(t)$ in Fig. 3.1 (d) it is actually possible to represent the rather complicated ECG signal by several linearly independent model functions $s_k(t)$. In general terms:

$$X(t) = \sum_{k=0}^{\infty} s_k(t) . \quad (3.4)$$

Then, each model function $s_k(t)$ should relate to one of the well defined spectral ridges

---

[2] This scaling ensures high time resolution for fast oscillations and high frequency resolution for slow oscillations.

in the signals wavelet spectrum and thus, to a dominant and time dependent frequency content.

Hilbert-Huang transformation

A particular filtering method which yields a decomposition of the form Eq. (3.4) is the *Hilbert-Huang transformation*. The method pursues a procedure called *sifting* to reconstruct each single $s_k(t)$. In the process, the signal is iteratively demodulated using envelopes and thus, amplitude information. The resultant model functions have zero mean and can be further analysed using the Hilbert transform Eq. (3.8). Although this method is applicable to a wide range of experimental signals, several drawbacks exist:

- If spectral ridges come close to each other, cross or merge, the decomposition becomes ambiguous
- The construction/definition of model functions $s_k(t)$ is based on a highly method-dependent and thus, problematic separation of amplitude and phase modulation.
- While mathematically, a representation by several $s_k(t)$ is valid, such a decomposition has no obvious connection to the asymptotic phase $\varphi(t)$ of nonlinear oscillators.

Despite these well known fact, the approach finds successful application in a wide range of research areas [165, 167, 168].

3.2 Hilbert transforms and quadratures

The time-varying frequency content of a signal might be captured by means of the true phase $\phi(t)$ of a signal. Then, a straight forward approach to define an *instantaneous frequency* is:

$$\Omega(t) = \dot{\phi}(t) \rightarrow \phi(t) = \phi_0 + \int_0^t \Omega(\tau) d\tau \ . \tag{3.5}$$

Eventually, the true phase of the signal $\phi(t)$ is in close connection to the asymptotic phase $\varphi(t)$ but not necessarily under all circumstances.

A particular example where a phase $\phi(t)$ is meaningful, is the monocomponent signal $X_{\text{mono}}(t) = s_1(t) = A(t)\cos(\phi(t))$. It is defined by a single model function $s_1(t)$ of amplitude $A(t)$ and who's frequency is $\Omega(t)$. However, generally such a definition leads to erroneous results:

- An instantaneous frequency defined through Eq. (3.5) has no obvious meaning if a signal $X(t)$ is composed of several base functions (see Eq. (3.4)). In this case, one speaks of a *multicomponent signal*. For example, if $s_1(t) = \cos(\phi_1(t))$ and $s_2(t) = \cos(\phi_2(t))$, $\Omega_{1,2}(t)$ represent the rhythm of $s_{1,2}(t)$. However, no simple frequency law exists for $X(t)$ (for an illustration see Fig. 3.1).
- For dynamical systems, the asymptotic phase $\varphi(t)$ and amplitude-like deviation $\delta\mathbf{y}(t)$ are not independent due to isochronic coupling in the underlying dynamical system. A decomposition of (observed) amplitude and phase dynamics thus,

requires additional information which usually is not accessible. This aspect of oscillatory data analysis is touched in Ch. 5 and 6

A mathematical definition of amplitude, phase and instantaneous frequency for generic signals was put forward by Denis Gabor[3]: Given $X(t)$, a decomposition into a pair of amplitude and phase is provided by the *analytic signal*, $z(t) = A_z(t)\exp(i\theta^{(a)}(t))$ where amplitude $A_z^2(t) = \Re[z]^2(t) + \Im[z]^2(t)$ and the *analytic* phase is

$$\theta^{(a)} = \arg[z](t) \ . \tag{3.6}$$

The analytic signal is defined through the spectral relation

$$z(t) = \mathcal{F}^{-1}[\mathcal{F}_z(\omega)], \qquad \mathcal{F}_z(\omega) = \begin{cases} 2\mathcal{F}_X(\omega) & ,\text{if } \omega \geq 0 \\ 0 & ,\text{if } \omega < 0 \end{cases} \ . \tag{3.7}$$

Thus, effectively the suppression of $\mathcal{F}_X(\omega)$ at negative frequencies and backward transformation suffices to construct an amplitude-phase representation of $X(t)$. This construction allows a determination of all moments[4] of the frequency $\langle\omega^n\rangle$.

Further examination of the analytic signal shows that $\mathcal{F}_z(\omega) = (1 + \text{sgn}(\omega))\mathcal{F}_X(\omega)$. Thus, $\Re[z](t) = X(t)$ while $\Im[z](t) = -\mathcal{F}^{-1}[i\text{sgn}(\omega)\mathcal{F}_X(\omega)]$. The latter construction results in a time-domain convolution of the form

$$\Im[z](t) = \frac{1}{\pi t} * X(t) = \frac{\text{p.v.}}{\pi}\int_{-\infty}^{\infty}\frac{X(\tau)}{t-\tau}d\tau =: \hat{H}[X](t) \tag{3.8}$$

which is known as the *Hilbert transform*[5]. In spectral notation:

$$\mathcal{F}_{\hat{H}[X]}(\omega) = -i\text{sgn}(\omega)\mathcal{F}_X(\omega) \ . \tag{3.9}$$

From this, it can be seen how well behaved the Hilbert transform embedding actually is: Since $\langle X, \hat{H}[X]\rangle = 0$ for all smooth $X(t)$, loops are always unfold and the existence of a pair of phase $\theta^{(a)}(t)$ and amplitude $A_z(t)$ is guaranteed[6] (compare Fig. 1.9 (a,b) where the delay embedding unfolds for specific parameters only).

However, a phase reconstruction by means of the Hilbert transform and the analytic signal faces several problems:

- If more than one maximum is present in a signal period (e.g. see Figs. 4.3 and 5.1), the Hilbert transform embedding possesses several loops. Thus, the frequency $\dot{\theta}^{(a)}(t)$ can be negative, in clear contrast to the phase reduction theory Sec. 1.2 and Ch. 2.

- In situations where a signal phase $\phi(t)$ is meaningful, a reconstruction of it by means of the analytic signal does not yield a proper reconstruction of $\phi(t)$ if phase modulations are faster than the average frequency of oscillation. This problem is particularly discussed in Ch. 4.

---

[3] Denis Gabor, (1900-1979) [4]

[4] Moments of frequency are defined by $\langle\omega^n\rangle = \int_{-\infty}^{\infty}\omega^n|\mathcal{F}_z|^2(\omega)d\omega/\int_{-\infty}^{\infty}|\mathcal{F}_z|^2(\omega)d\omega$. In contrast, for the spectrum of a real signal all odd moments vanish since $|\mathcal{F}_X|^2(\omega)$ is an even function.

[5] David Hilbert (1862-1943) [4]

[6] Using the equivalence of scalar products in time and frequency domain, it is $\int_{-\infty}^{\infty}\mathcal{F}_X(\omega)\mathcal{F}^*_{\hat{H}[X]}(\omega)d\omega = i\int_{-\infty}^{\infty}\text{sgn}(\omega)|F_X|^2(\omega)d\omega = 0$.

While the first point can be readily solved using an other parametrisation of the embedding curve (see Sec. 4.1.2), the second problem constitutes a main obstacle for a reconstruction of the true signal phases $\phi(t)$ from the analytic signal.

Generally, a function $\Im[z](t) = X^{(q)}(t)$, which leads to an immediate/mutual construction of $\phi(t)$ and $A(t)$ is called *quadrature*. The Hilbert transform for generic signals is actually an approximation for such a function (see App. A.4 for an example by means of $X_{\text{mono}}(t)$). However, generally a construction of the quadrature for generic signals is not known or not meaningful at all while an asymptotic phase $\varphi(t)$ might still be existent.

The discrepancy of quadrature and Hilbert transform is reflected in

- **Bedrosian's theorem**: The Hilbert transform of two function $q_l(t)$ and $q_h(t)$ with non-overlapping spectra $\mathcal{F}_{q_l}(\omega) \neq 0$ for $|\omega| < C$ and $\mathcal{F}_{q_h}(\omega) \neq 0$ for $|\omega| > C$, $C > 0$ is

$$\hat{H}[q_l q_h](t) = q_l(t)\hat{H}[q_h](t) \ . \tag{3.10}$$

For example, given a modulated amplitude[7] $A(t) = A_0 + \varepsilon\tilde{A}(t)$ and phase $\phi(t) = t + \varepsilon q(t)$, a mono-component signal signal $X_{\text{mono}}(t) = A(t)\cos(\phi(t))$ is a *narrowband signal* if $\mathcal{F}_A(\omega)$ and $\mathcal{F}_\phi(\omega)$ are zero for $|\omega| > \langle\dot{\varphi}\rangle_t$ - and thus obey the Bedrosian theorem. Otherwise a signal $X_{\text{mono}}(t)$ is a *wideband signal* [169, 170].

For narrowband signals, the Hilbert transform can be a rather good approximation of the quadrature such that $\phi(t)$ can be retrieved from data. In contrast, for wideband signals, the assertion[8] $\hat{H}[X](t) = X^{(q)}(t)$ is not true (see Ch. 4).

In conclusion, neither the mainly spectral methods in Sec. 3.1 nor the purely signal based Hilbert transform analysis in this chapter are fully suitable for a reconstruction of the asymptotic phase $\varphi(t)$.

3.3 Asymptotic phase and signal

In a data driven phase reconstruction for dynamical systems, the asymptotic phase $\varphi(t)$ needs to be reconstructed from measurements of the actual state dynamics $\mathcal{Y}(t)$.

Generally, such a measurement $X(t) = \hat{M}[\mathcal{Y}](t)$ is a function of all degrees of freedom present in the system (see Eqs. (1.9) and (1.4)). While such dynamics can be practically infinite-dimensional, a description by means of dominant degrees of freedom $\mathbf{y}(t)$ might be possible. In particular, for a weakly perturbed self-sustained oscillator, the asymptotic phase contains most dynamic information (see Eq. 2.2). In such situations, a representation

$$X(t) = \hat{M}[\mathbf{y}^{(0)}(\varphi(t)) + \delta\mathbf{y}(t)] \approx \hat{M}[\mathbf{y}^{(0)}](\varphi(t)) + \hat{M}'[\mathbf{y}^{(0)}](\varphi(t))\delta\mathbf{y}(t) \tag{3.11}$$

of the generic signal in terms of a purely phase modulated component and a (small) perturbation is justified. It can be seen that the purely phase modulated component corresponds to the dynamics on the limit cycle, while the perturbation depends on the deviation of the underlying system from the cycle.

---

[7] For simplicity of the following argumentation, it is assumed that amplitude and phase modulation share the same strength ε.

[8] This property is also called *harmonic correspondence* [171].

Accordingly, the task of phase estimation for non-linear oscillators reduces in leading order to the problem of finding a decomposition for

$$X(t) = \hat{M}[\mathbf{y}^{(0)}](\varphi(t)) =: S(\varphi(t)), \qquad S(\varphi) = \hat{M}[\mathbf{y}^{(0)}](\varphi), \qquad S(\varphi+2\pi) = S(\varphi) \tag{3.12}$$

in terms of a *waveform* $S(\varphi)$ and $\varphi(t)$. (Similarly, if a purely phase-modulated signal is observed, $S(\phi)$ and $\phi(t)$ have to be reconstructed.) In either case, this is accomplished by *phase demodulation* for which the novel approach of iterative Hilbert transform embeddings (IHTE) will be introduced in Ch. 4.

The applicability of demodulation in case of generic signals, waveforms and phase-amplitude modulation is discussed in more detail in Ch. 6. Generally, signal variations due to the amplitude dynamics in the original state space can not be neglected. But their influence on the reconstruction is potentially small if the limit cycle is sufficiently stable (see Ch. 5 for an application). In all such cases, a generalised waveform is provided by

$$X(\varphi) = X(t(\varphi)) \approx \hat{M}[\mathbf{y}^{(0)}](\varphi) + \hat{M}'[\mathbf{y}^{(0)}](\varphi)\delta\mathbf{y}(t(\varphi)) \ . \tag{3.13}$$

It can be seen that this quantity is similar to $S(\varphi)$ for vanishing amplitude perturbations while for weak amplitude perturbation it contains a weak non-2π-periodic component. In either case, $X(t)$ might be well approximated as a purely phase-modulated signal such that the true phase $\phi(t)$ Eq.(3.5) provides a data-based approximation of the asymptotic phase $\varphi(t)$.

3.4 Phase and protophase for phase modulated signals

Decompositions of a phase modulated signal $X(t)$ into a waveform and a phase are not unique. Indeed, it is possible to define a *phase-to-protophase transformation*

$$\theta = \Theta(\phi), \qquad \Theta(\phi + 2\pi) = \Theta(\phi) + 2\pi \tag{3.14}$$

such that $X(t)$ remains the same under change of variables:

$$X(t) = S(\phi(t)) = S(\Theta^{-1}(\theta(t))) = \tilde{S}(\theta(t)), \qquad \tilde{S}(\theta) = S(\Theta^{-1}(\theta)) \ . \tag{3.15}$$

Here, $\tilde{S}(\theta)$ is a *proto-waveform* and its argument, $\theta(t)$, is called *protophase* (e. g. $\theta^{(a)}(t)$ Eq. (3.6)). Exploiting this definition, the frequency of the protophase is given by

$$\dot{\theta} = \Theta'(\Theta^{-1}(\theta))\omega =: f(\theta) \ . \tag{3.16}$$

Thus, $f(\theta)$ depends on θ such that $\theta(t)$ contains 2π-periodic modulations and is not a proper phase. This analysis is valid, as long as $\Theta(\phi)$ is monotonous.

Generally, demodulation provides a decomposition into $\tilde{S}(\theta)$ and $\theta(t)$ rather than $S(\phi)$ and $\phi(t)$. All the possible decompositions differ in 2π-periodic modulations of the waveform and the argument. Since such modulations change the shape of $\tilde{S}(\theta)$ and $\theta(t)$ simultaneously, it is impossible to decide which representation of the signal $X(t)$ is preferable. Thus, it is generally not possible to find $S(\phi)$ and $\phi(t)$ from demodulation alone.

To select from all possible results a preferable waveform $S(\phi)$ and phase $\phi(t)$, additional criteria can be utilised. Notably, these criteria are based on the assumption that a mapping exists while determination of the mapping might not be possible under all circumstances.

If the actual phase dynamics of $\phi(t)$ is known, an ideal phase-to-protophase mapping $\Theta(\phi)$ can be found by a direct numerical fitting procedure (see Sec. 6.3). In situations where the mapping has to be estimated solely from data of non-linear oscillators, a criterion follows from the dynamic assumption that the phase-probability-distribution density $\rho(\phi)$ should be flat. In other words, $\dot{\phi}$ should be independent of $\phi(t)$ what means that all 2π-periodic modulations are shifted to the waveform only. A phase approximation fulfilling this criterion is denoted by $\psi(t)$ and $\dot{\psi}(t) \approx \dot{\phi}(t)$. In particular, if a phase obeys a model similar to Eq. (2.4), it is given by

$$\psi(t) = \omega t + \varepsilon \tilde{q}(t) \ . \tag{3.17}$$

Practically, a data driven *protophase-to-phase transformation* is accomplished by inversion of Eq. (3.14) in all situations where $\Theta^{-1}(\theta)$ exists.

Summarising the upper discussion, the task of phase reconstruction for phase modulated signals is accomplished in two steps:

(i) Phase demodulation

(ii) Protophase-to-phase transformation

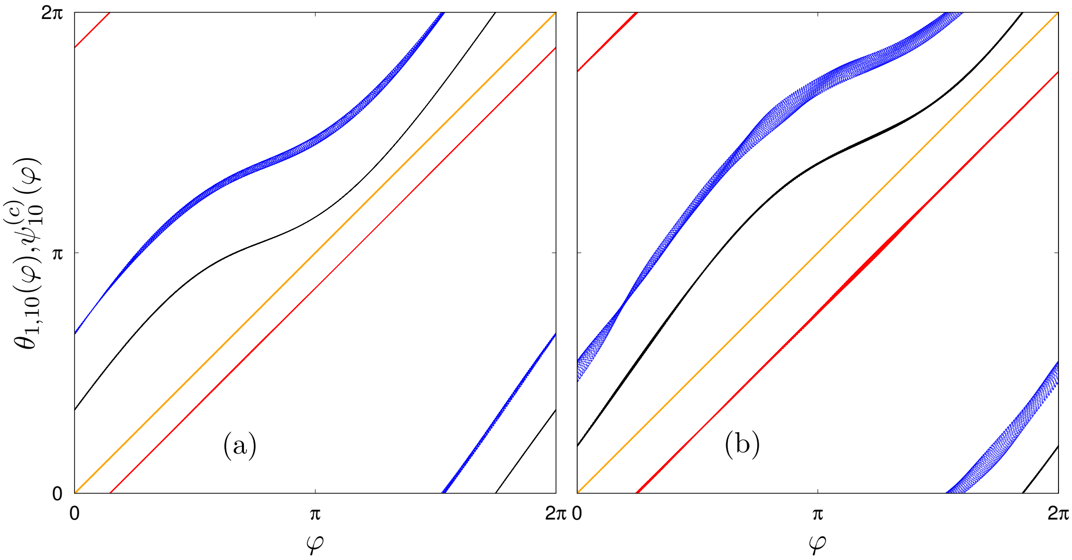

Figure 3.2: Depicted are the phase-to-protophase maps Eq. (3.23) for reconstruction of the SL phase dynamics. The system is observed by multicomponent signals $X_{5,6}(t)$ Eq. (5.2) (see Sec. 5.2.1). Both observables contain amplitude modulations which are small and result from perturbations of the dynamics from the limit cycle. Demodulation was accomplished by means of IHTE (see Sec. 4.1.3) making use of a spline based protophase $\theta^{(c)}(t)$ (see Sec. 4.1.2). Panel (a) shows results for the cosine-like signal $X_5(t)$ with only weakly 2π-periodic modulations of the protophase. Similarly, panel (b) depicts results for the signal $X_6(t)$ having an additional maximum in each period. For this signal, 2π-periodic modulations are much more pronounced. The transformations correspond to waveforms depicted in Fig. 5.1 and results shown in Figs. 5.2 and 5.3. Colours correspond to $\Theta_1^{(c)}(\varphi)$ (blue; this data forms a rather wide band what indicates that commonly obtained protophases are not precise), $\Theta_{10}^{(c)}(\varphi)$ (black; this data is the result of IHTE and forms a narrow line what indicates for a good protophase reconstruction), $\psi_{10}^{(c)}(\varphi)$ (red; this narrow line is straight thus, a good approximation of the original phase is achieved). The orange line is the diagonal. For better visibility the curves are shifted vertically.

Phase demodulation is achieved, if

$$\text{(I): } \tilde{S}(\theta+2\pi)=\tilde{S}(\theta), \qquad \text{(II): } \forall t : \dot{\theta}(t)>0 \ , \tag{3.18}$$

and a protophase-to-phase transformation is considered to be a success, if

$$\text{(III): } \rho(\psi)=\text{const.} \ . \tag{3.19}$$

Chapter 4 focusses on steps (i) for purely phase modulated signals and discusses optimal demodulation with examples. Step (ii) is discussed in more detail in Ch. 5 and 6. In these chapters, the generally more challenging task of reconstructing $\varphi(t)$ for dynamical system from observation is discussed. In particular, for dynamical systems, the mapping $\Theta^{-1}(\theta)$ gives rise to a generalised proto-waveform $X(\theta)=X(t(\theta))$ similar to Eq. (3.13).

3.5 Data-driven protophase-to-phase transformation

For a non-modulated phase $\phi(t)=\omega t$, an inversion of the protophase-to-phase mapping Eq. (3.14)

$$\frac{d\phi}{d\theta}=\frac{\omega}{f(\theta)}, \qquad \phi(t)=\omega\int_0^{\theta(t)}\frac{d\tilde{\theta}}{f(\tilde{\theta})} \ . \tag{3.20}$$

mutually yields $\psi(t)=\phi(t)$ and is always possible if the protophase increases monotonously ($f(\theta)>0$).

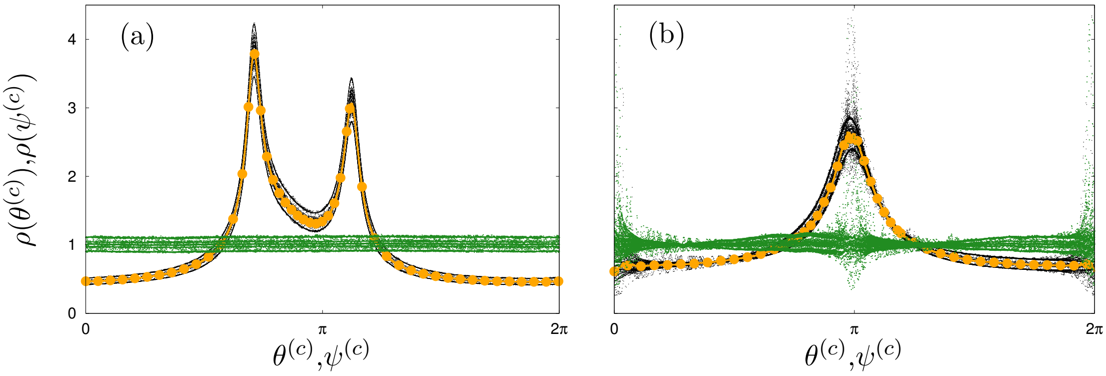

Figure 3.3: Depicted are two examples of phase-densitiy estimation corresponding to Fig. 5.8 of Sec. 5.2.3, where the phase moduation emanates from a telegraph process. The empirical phase densities $\rho(\theta^{(c)})$ (black) are approximated by a Fourier series Eq. (3.22) (orange). While the protophase densities are inhomogeneous, after protophase-to-phase transformation Eq. (3.23) the phase density for $\psi^{(c)}(t)$ (green) is essentially flat. Depicted in (a) are results for the phase modulated signal $X_3(t)$ here 300 Fourier modes are calculated. In (b) results for the observalbe $X_6(t)$ and 50 Fourier modes are shown. The overall shape of $\rho(\theta^{(c)})$ in (b) corresponds to phase-to-protophase mappings in Fig. 3.2(b).

A more challenging situation occurs, if a phase is modulated as is usually the case for perturbed oscillator. Then, $\dot{\theta}(t)$ contains information about the signal waveform *and* the system dynamics. Therefore, one is interested in removal of 2π-periodic modulations while one wants to keep the actual modulation $q(t)$ hidden in the protophase. To achieve this, the phase probability distribution $\rho(\theta)$ of the respective protophase has to be estimated from $\langle \omega/f(\theta)\rangle_\theta$ in Eq. (3.20). This density is inhomogeneous for protophases while in an optimal result it is flat and thus independent of its argument. It follows

$$\frac{d\psi}{d\theta} = \rho(\theta), \qquad \psi(t) = \int_0^{\theta(t)} \rho(\tilde{\theta})d\tilde{\theta}\ . \tag{3.21}$$

By assumption (see condition (3.18), (I)), $\rho(\theta)$ is 2π-periodic. Thus it is reasonable to use a Fourier representation[9]

$$\rho(\theta) = \sum_{k=-\infty}^{\infty} F_k \exp(ik\theta), \qquad F_k = \frac{1}{2\pi}\int_0^{2\pi} \rho(\tilde{\theta})\exp(-ik\tilde{\theta})d\tilde{\theta}\ . \tag{3.22}$$

Then, integration in Eq. (3.21) yields the protophase-to-phase transformation for modulated phases[10]:

$$\psi(t) = \theta(t) + \sum_{\substack{k=-\infty \\ k\neq 0}}^{\infty} \frac{F_k}{ik}[\exp(ik\theta(t)) - 1]\ . \tag{3.23}$$

To determine the coefficients F_k in Eq. (3.22), an elegant approach follows from the definition of the density function as a representation of infinitely small histograms:

$$\rho(\tilde{\theta}) = 2\pi\langle \delta(\theta(t) - \tilde{\theta})\rangle_t\ . \tag{3.24}$$

Inserting this representation into Eq. (3.22) yields

$$F_k = \frac{1}{t_m - t_0}\int_{t_0}^{t_m} \exp(-ik\theta(t))dt\ . \tag{3.25}$$

In the following this procedure is called *density-based protophase-to-phase transform* (DPT) [166]. Although the DPT is not a filter, there exists almost certainly a discrepancy between $\psi(t)$ and the asymptotic phase $\varphi(t)$ of a dynamical system:

- The estimation of F_k involves the reconstructed protophase what stresses the need for a protophase in agreement with the criteria Eqs. (3.18) and (3.19).
- The DPT by construction yields an optimally uniform density of $\psi(t)$ as it assumes a uniform target density corresponding to a non-modulated phase $\varphi(t)$. Although this assumption removes almost all inhomogeneity in $\rho(\psi)$ there can exist small distortions in the actual phase density $\rho(\varphi)$ which are not taken into account.
- The statistical estimation of F_k has a rather slow convergence $\sim 1/\sqrt{t_m - t_0}$ since it is estimated from $\langle(\psi(t) - \varphi(t))^2\rangle_t \mapsto \min$.

As an example for possible problems, Fig. 3.3 presents the empirical phase densities for $\theta^{(c)}(t)$ and for $\psi^{(c)}(t)$ obtained from phase demodulation of two multi-component signals ($X_{3,6}(t)$ in Chs. 4, 5). In both cases, the transform yields an essentially flat phase distribution for the phase estimate $\psi(t)$. However, local distortions in case of the generic observable $X_6(t)$ are significant and indicate that the microscopic phase dynamics of the system is recovered only in parts. This problem is further discussed in Ch. 6.

---

[9] In principle, other function basins are equally valid. For example, one can perform an optimal kernel-density fit on $[0, 2\pi]$.

[10] Due to normalization $1 = (2\pi)^{-1}\int_0^{2\pi} \rho(\tilde{\theta})d\tilde{\theta}$ it follows $F_0 = 1$

Chapter 4

Phase demodulation with iterative Hilbert transform embeddings

Bibliographic information

This chapter is based on the publication:

Erik Gengel and Arkady Pikovsky
Phase demodulation with iterative Hilbert transform embeddings
Signal Processing 165 (2019): 115-127

Main findings:

- Definition of iterated Hilbert transform embeddings for phase modulated signals
- Theoretical analysis of spectral convergence for the proposed method
- Proof of concept by means of several examples

4.1 Phase demodulation

4.1.1 Embeddings revisited

The construction of analytic signal and delay embedding are similar geometric techniques for phase demodulation (see Secs. 3.3 and 3.4). The main idea in both cases is the following: Given the specific case of two signals[1] $X(t)$ and $Y(t)$, one constructs the complex-valued function $z(t) = X(t) + iY(t)$. A monotonous parametrisation

$$\theta(t) = \hat{P}[X, Y](t) \tag{4.1}$$

of its trajectory in $\mathbb{R}^2$ defines a protophase $\theta(t)$. In this relation, the non-linear operator $\hat{P}[X, Y]$ is defined through the way of protophase calculation (see Sec. 4.1.2).

If the two signals $X(t)$ and $Y(t)$ are simultaneously measured in an experiment, the calculation of a protophase is straight forward as the trajectory of $z(t)$ resembles an embedding. The intrinsically challenging problem occurs if only one signal $X(t)$ is observed. In this case, the operator $\hat{P}[X] = \hat{P}[X, Y[X]]$ depends on $X(t)$ and the assumptions which are used to construct the function $Y(t)$ from $X(t)$. The construction of $Y(t)$ is achieved by a time delay ($Y(t) = X(t - \tau_e)$), differentiation ($Y(t) = \dot{X}(t)$) or the Hilbert transform ($Y(t) = \hat{H}[X](t)$).

Similar to the Hilbert transform, the delay and derivative embeddings are linear operators in the spectral domain. However, their transfer functions $\exp(-i\tau_e\omega)$ and $-i\omega$

---

[1] $X(t)$ and $Y(t)$ should be at least partially linearly independent.

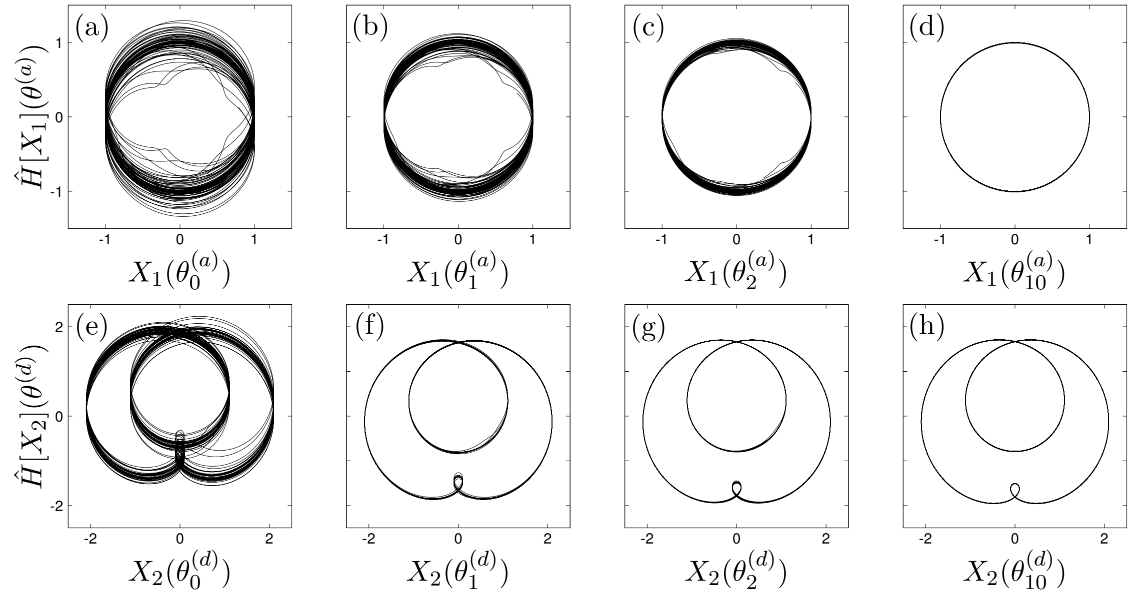

Figure 4.1: (Iterated) Hilbert transform embeddings for the phase-modulated signals $X_1(t) = S_1(\phi(t)) = \cos(\phi(t))$ and $X_2(t) = S_2(\phi(t)) = \cos(\phi(t)) - 0.7\sin(2\phi(t)) + \cos(3\phi(t))$ with phase $\phi(t) = t + 1.2(\sin(0.25\sqrt{2}t) + \cos(0.25\sqrt{3}t))$. Panels (a-d) show the simple embedding for $X_1(t)$, here the analytic protophase approximation was adopted. Panels (e-h) show the complex embedding $X_2(t)$, here the length-based protophase approximation $\theta^{(d)}(t)$ is used. Iteration steps: (a, e): $n = 0$; (b, f): $n = 1$; (c, g): $n = 2$, and (d, h): $n = 10$. Here $n = 0$ corresponds to the common Hilbert embedding over time. It can be seen that this embedding resembles a band what indicates that the demodulation result does not obey constraints Eq. (3.18).

result in different stability properties and extraction success (compare as an example results in Fig. 1.9 and see the info box in Sec. 4.2.2). Delay and derivative embedding are relatively close to the physical intuition: Low-dimensional non-linear oscillations are described by coordinates $y(t)$ and $\dot{y}(t)$ which find an analogue in $X(t)$ and $\dot{X}(t)$. Complementing is the idea that in a periodic system, the history of an observation $X(t)$ repeats itself after a specific delay. Moreover, numerical implementation of both methods is rather simple. In more general terms, the usage of delay and derivative embedding follows from generic mathematical analysis of measurement process and state space dynamics [133].

In contrast, the Hilbert transform is mutually defined as a global transformation[2] what opposes the physical intuition that the asymptotic phase $\varphi(t)$ – first of all – depends on the state of a system at time t only. However, the Hilbert transform results in a parameter-free demodulation and its mathematical definition guarantees the existence of a well behaved embedding and a protophase.

The great disadvantage of the Hilbert transform embedding, is that its results are meaningful for narrowband signals while for signal with wideband components, an eventually possible separation into waveform $S(\phi)$ and phases $\phi(t)$ is inaccurate (see Sec. 3.1 and Fig. 4.1). As a consequence, also the Hilbert transform embedding of a limit cycle generally does not preserve the dynamics of $\varphi(t)$.

A common cure for this problem involves additional filtering prior to signal demodulation. By this, the spectrum of $X(t)$ is truncated such that the Hilbert transform yields

---

[2] For data, the integration is confined to the finite time interval $[t_0, t_m]$ rather than $[-\infty, \infty]$.

reliable results. The corresponding phase reconstruction however, omits viable information about the phase dynamics on fast time scales. In contrast, smoothing is not needed at all if an oscillator is influenced by a slow input. For example, in the resting state an average human heart beats four times in one breathing cycle [172]. The respiratory forcing is thus slow.

4.1.2 The art of phase reconstruction

In experimental and theoretic literature different phase calculation approaches exists. Many of them are based on the analytic phase $\theta^{(a)}(t)$ Eq. (3.6). However, this protophase definition is limited to circular embeddings, while for embeddings that contain additional loops, $\theta^{(a)}(t)$ evidently leads to a negative phase derivative, in conflict with Eq. (3.18,(II)).

Less common in application – though more convenient – are methods based on marker-events and the arc length of the embedding

$$L(t) = \int_{t_0}^{t} \sqrt{dX^2 + dY^2}\,. \tag{4.2}$$

These procedures have been developed as ad-hoc approaches in the analysis of physiological data such as the ECG, where embeddings contain many smaller loops due to the different characteristic wave complexes[3]. The methods of calculation usually involve two steps:

(I) Determination of marker events t_j and

(II) Projection of $L(t)$ to multiples of 2π.

To accomplish step (I), one chooses a Poincaré section[4] in the $\{X, Y\}$ plane that corresponds to a major feature of $X(t)$ such as a main maximum. The marker t_j then is defined as the time of crossing. The periods of the signal then, are estimated[5] as $T_j = t_{j+1} - t_j$. Step (II) is achieved by projection of $L(t)$ in each period T_j to the interval $[2\pi j, 2\pi(j+1)]$.

An example for this is the linear interpolation[6]

$$\theta^{(b)}(t) = 2\pi j + \frac{L(t) - L(t_j)}{L(t_{j+1}) - L(t_j)}\,. \tag{4.3}$$

Calculated in this way, the protophase is a continuous but non-differentiable function of time having jumps in the phase derivative at times t_j (see Fig. 4.2) [166, 98]. For a smoother protophase definition, two novel approaches are discussed next. In Tab. 4.1 main aspects of the different approaches are compared.

---

[3] The procedures are robust in the sense that a protophase always grows monotonous since $\dot{L}(t) > 0$.

[4] Henri Poincaré (1854-1912) [4]

[5] In practice, accurate determination of T_j is achieved by polynomial interpolation on a symmetric set of points around t_j.

[6] Actually, the simplest calculation method uses T_j instead of $L(t)$: $\theta(t) = 2\pi(t - t_j)/T_j$. However, this protophase omits any additional information about the signal in between markers and thus is only a zero-order approximation of the dynamics.

Protophase	Complexity	Smoothness	Loops	Theory	Stability	Periodic
$\theta^{(a)}(t)$	simple	$\in C^{\infty}(\mathbb{R},\mathbb{R})$	X	✓	✓, (X)	✓
$\theta^{(b)}(t)$	medium	$\in C^{1}(\mathbb{R},\mathbb{R})$	✓	X	✓	✓
$\theta^{(c)}(t)$	advanced	$\in C^{2}(\mathbb{R},\mathbb{R})$	✓	X	✓	✓
$\theta^{(d)}(t)$	advanced	$\in C^{\infty}(\mathbb{R},\mathbb{R})$	✓	✓	✓	X

Table 4.1: Listing of major characteristics of the discussed phase calculation methods. Columns refer to *complexity* of the numerical implementation, *smoothness* of the phase derivative, *Loop*-demodulation for multi-component signals, *theory* development in this work and in general context, *stability* of the approach according to practical hind side with regard to changes in the waveform and robustness of iteration, and whether the protophase is 2π-*periodic*.

Spline interpolation and protophase

The first improvement of protophase calculation is based on cubic-spline interpolation. In this approach, the linear interpolation Eq. (4.3) is replaced by a cubic spline what leads to a well defined first derivative of $\theta(t)$ at markers t_j:

$$\theta^{(c)}(t) = \mathrm{SPL}(L(t)) \ . \tag{4.4}$$

The only additional effort here, is the determination of second-order derivatives $d^2\mathrm{SPL}/dL^2$ at points $L(t_j)$. These coefficients are a priori unknown but can be obtained from continuity assumption on the first derivatives $d\mathrm{SPL}/dL$ between intervals $[L(t_{j-1}), L(t_j)]$ and $[L(t_j), L(t_{j+1})]$ (see Fig. 4.2)

$$\frac{d\mathrm{SPL}}{dL}(L(t_j))\Big|_{[L(t_{j-1}),L(t_j)]} \overset{!}{=} \frac{d\mathrm{SPL}}{dL}(L(t_j))\Big|_{[L(t_j),L(t_{j+1})]} \ .$$

The resulting matrix equation for all j can be solved by imposing proper boundary conditions[7].

Phase calculation based on splines represents in several ways an intermediate and convenient approach to phase extraction for experimental signals: It is – in contradistinction to $\theta^{(a)}(t)$ – a non-local and thus, more robust method while it still is 2π-periodic by construction. Moreover, it provides a continuous instantaneous frequency.

Noteworthy, the use of splines to maintain smoothness of the protophase results in a small additional distortion of $\theta^{(c)}(t)$. Potentially, these distortions cause the protophase to violate Eq. (3.18,(II)). However, in most of the practical applications the amplitude of additional distortions changes slowly enough to ensure monotonicity.

Optimal length protophase

Finally, an elegant approach arises from the idea that $L(t)$ can be normalized by a common factor. Namely, if the length growth with a common frequency $\omega_L = L^\star/T$, the original base frequency of the phase is $\omega = 2\pi\omega_L/L^\star$. A slightly different situation occurs if the signal is modulated. Then, each period T_j results in periodicity lengths

---

[7] In this work, the natural boundary condition is applied, where $d^2\mathrm{SPL}/dL^2 = 0$ at t_0 and t_m. The method can be found in Sec. 3.3 in [173].

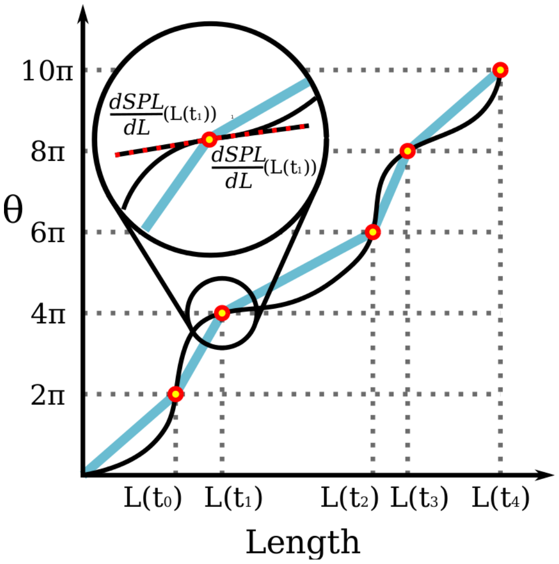

Figure 4.2: Depicted are the phases $\theta^{(b)}(L)$ (blue straight lines) and $\theta^{(c)}(L)$ (black curves) up to inbetween marker events t_4 (red-yellow dots). Due to changes of the periodicity, (while phases increase by 2π) the derivative of $\theta^{(b)}(L)$ is not defined at t_j. In contrast, $\theta^{(c)}(L)$ is differentiabe at the cost of additional distortions. The actual magnitude of the distortions is exagerated here due to large variations in the periodicity.

$L_j^\star = L(t_{j+1}) - L(t_j)$ from which an optimal periodicity length $L^\star$ has to be calculated. In either case, a protophase is defined by

$$\theta^{(d)}(t) = \frac{2\pi}{L^\star} L(t) \; . \tag{4.5}$$

A reliable method to estimate $L^\star$ is based on minimisation of the *periodicity error*

$$\mathrm{Err}^2_{\mathbf{q}}(\ell) = \frac{1}{\hat{N}} \int_{\mathbf{q}(t_0)}^{\mathbf{q}(t_m)} [X(\mathbf{q}+\ell) - X(\mathbf{q})]^2 d\mathbf{q}, \qquad \hat{N} = \int_{\mathbf{q}(t_0)}^{\mathbf{q}(t_m)} X^2(\mathbf{q}) d\mathbf{q} \; . \tag{4.6}$$

Quite generally, $\mathbf{q}(t)$ can be any monotonous function of time. Here, $\mathbf{q}(t) = L(t)$ and minimization[8] is carried out for the free parameter ℓ. The optimal periodicity is then given by

$$L^\star = \mathrm{argmin}\ \mathrm{Err}_L(\ell) \; , \qquad \mathrm{Err}^\star_L = \min_\ell \mathrm{Err}_L(\ell) \; . \tag{4.7}$$

$\mathrm{Err}^\star_{\mathbf{q}}$ converges to zero only if $X(\mathbf{q})$ is perfectly $L^\star$-periodic and purely phase modulated. In case of 2π-periodic protophases $\mathbf{q}(t) = \theta^{(a,b,c)}(t)$, the minimization with respect to ℓ is not needed.

Noteworthy, for the calculation of $\theta^{(d)}(t)$ no active determination of markers t_j is needed what provides a perfectly smooth protophase. However, $\theta^{(d)}(t)$ is not 2π-periodic what violates the assumptions of protophase-to-phase transformation.

4.1.3 Iterated Hilbert transform embeddings

In the common procedure making use of the Hilbert transform Eq. (3.8), a protophase is calculated from the embedding of $z(t)$ using Eqs. (3.6), (4.3), (4.4) or (4.5). Then, the obtained proto-waveform resembles in many cases a band[9] due to the inconvenience of the Hilbert transform to yield the mutual quadrature of a signal (see Sec. 3.1 and Fig. 4.3).

---

[8] In this work , bisection is used for minimisation as the considered signals result in a single minimum of $\mathrm{Err}^2_L(\ell)$ in $[L^\star/2, 3L^\star/2]$.

[9] Such an outcome is clear for signals with large amplitude variation but it is reminiscent also for purely phase modulated wideband signals.

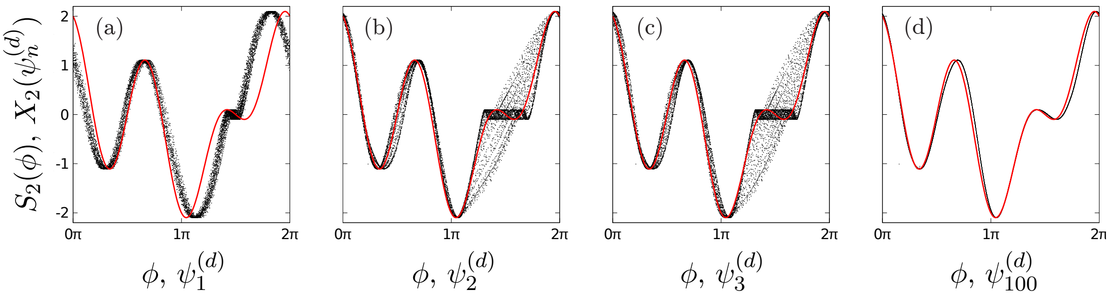

Figure 4.3: Depicted are the reconstructed waveforms (black dots: $S_2(\psi_n^{(d)})$) and the actual wave form $S_2(\phi)$ from Sec. 4.2 (red lines). Shown are iterations: (a): $n = 1$, (b): $n = 2$, (c): $n = 3$, (d): $n = 100$. The depicted protowaveforms correspond to embeddings in Fig. 4.1 cases (e-h). Note that a protophase-to-phase transformation Eq. (3.23) is applied here to shift 2π-periodic modulations from the protophases to the proto-waveforms.

An optimal Hilbert-transform embedding follows from iteration, motivated by the following observation: While the signal $X(t)$ definitely is not periodic, the waveform $X(\theta)$ shows already less modulation and is closer to 2π-periodicity. A natural extension is to proceed with integration of $X(\theta)$ in the variable θ! Introducing an index that labels the step of iteration and letting $t = \theta_0$ and $\theta(t) = \theta_1(\theta_0)$, the next approximation of protophase is given by $\theta_2(\theta_1)$. As an example, Fig. 4.3 depicts the multicomponent waveform $X_2(\psi^{(d)})$. Continuation of the procedure to $\theta_n(t)$ is straight forward and leads to the definition of the iterated Hilbert transform:

$$\hat{H}[X](\theta_n) := \frac{\text{p.v.}}{\pi} \int_{\theta_n(t_0)}^{\theta_n(t_m)} \frac{X(\tilde{\theta}_n)}{\theta_n - \tilde{\theta}_n} d\tilde{\theta}_n \; . \tag{4.8}$$

Defined in this way, each iterative step is given by

$$\theta_{n+1}(\theta_n) = \hat{P}[X](\theta_n) \; . \tag{4.9}$$

Here the operator $\hat{P}[X](\theta_n)$ is defined for all four protophases through the algorithmic scheme Fig. 4.4 and the described numerical procedures in Sec. 4.1.2. Moreover, since the phase-to-protophase mapping $\theta_n = \Theta_n(\phi)$ is invertible, an iterated (generalised) proto-waveform is always given by $X(\theta_n) = X(\Theta_n^{-1}(\theta_n))$. Noteworthy, due to the differences of phase-to-protophase maps in each iterative step, the functions $X(\theta_n)$ are all different. This difference is indicated by the index of protophases. As an example, Fig. 4.4 presents the iterative procedure for $\theta^{(c,d)}(t)$.

The numerical calculation of the integral Eq. (4.8) comprises two major challenges:

- Due to the reuse of the protophase proxis θ_n in the iterative procedure, integration has to be performed on non-uniform grids
- The singularity of integration at $\tilde{\theta}_n = \theta_n$ has to be treated with special caution.

Further details are provided in [161].

4.2 Theory of convergence

While IHTE permits quite general waveforms and phase models (see Sec. 4.4), in the following the analytically tractable example with

$$X_1(t) = S_1(\phi(t)), \qquad S_1(\phi) = \cos(\phi), \qquad \phi(t) = t + \varepsilon q(t) \tag{4.10}$$

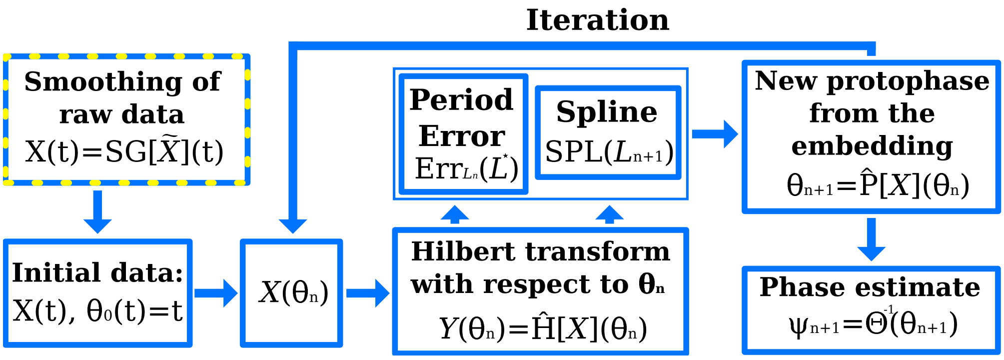

Figure 4.4: Depicted is the iterative procedure based on length and protophases $\theta^{(c,d)}$. As a preliminary step, the raw data $\tilde{X}(t)$ is smoothed if needed by means of a Savitzky-Golay filter (blue-yellow box). Usually, only one iteration (with θ_0) is performed calculating $\theta^{(a,b)}(t)$.

is considered to elaborate on the impact of iterations. Here, $q(t)$ is the modulation of the phase and since $X_1(t)$ is a monocomponent signal, it suffices to consider $\psi(t) = \theta(t)$.

For phase-modulated signals, iterative application of the extraction operator Eq. (4.9) provides protophase proxis $\theta_n(t)$ which are generally not perfectly demodulated in the first iterative steps. Namely, the modulation $\tilde{q}_n(t)$ Eq. (3.17) differs from the true modulation of $\phi(t)$. Then, it is possible to determine the success of convergence[10] of IHTE directly based on the residue $\Delta_n(t) = \phi(t) - \psi_n(t)$.

Starting at $\theta_0(t) = t$, subsequent residues are given by $\theta_1(\theta_0) = \phi(\theta_0) - \Delta_1(\theta_0)$, $\theta_2(\theta_1) = \phi(\theta_1) - \Delta_2(\theta_1)$, ... To demonstrate the generality of findings, the analytically tractable cases of $\theta^{(a,d)}(t)$ are analysed further.

4.2.1 Perturbed signal and protophases

Before discussing the convergence mechanism, perturbed equations for the protophases are derived here. First note that

$$X_1(t) = S_1(\phi(t)) \approx S_1(t) + \varepsilon \dot{S}_1 q(t), \qquad Y_1(t) \approx \hat{H}[S_1](t) + \varepsilon \hat{H}[\dot{S}_1 q](t)\ . \tag{4.11}$$

For the protophases in the first step, this means

$$\begin{aligned}\theta^{(a)}(t) &= \arg[z](t) = \arctan\left[\frac{Y_1(t)}{X_1(t)}\right]\\ &\approx \arg[S_1(t) + i\hat{H}[S_1](t)] + \varepsilon \frac{\hat{H}[\dot{S}_1 q](t) S_1(t) - \dot{S}_1 q(t) \hat{H}[S_1](t)}{S_1^2(t) + (\hat{H}[S_1])^2(t)}\end{aligned} \tag{4.12}$$

and

$$\begin{aligned}\theta^{(d)}(t) &= L(t) = \int_0^t \sqrt{X_1'^2 + Y_1'^2}\, d\tau\\ &\approx \int_0^t \sqrt{S_1'^2 + (\hat{H}[S_1'])^2}\, d\tau + \varepsilon \int_0^t \frac{(S_1'' q + S_1' q') S_1' + \hat{H}[S_1'' q + S_1' q'] \hat{H}[S_1']}{\sqrt{S_1'^2 + (\hat{H}[S_1'])^2}}\, d\tau\ .\end{aligned} \tag{4.13}$$

---

[10] Complementary is the optimal periodicity error $\mathrm{ERR}^{\star}_{\theta}$ which also converges for arbitrary protophases $\theta(t)$. If amplitude variations are present, convergence of both measures is not strictly related.

These results show, that $\hat{H}[X_1](t)$ applied on a signal without phase modulation ($q(t) = 0$) achieves demodulation already in the first step while in case of modulations, a residue $\Delta(t) = \phi(t) - \theta(t)$ exists which is a consequence of the afore discussed discrepancy between Hilbert transform and quadrature for wideband signals (see Sec. 3.2).

4.2.2 The effect of iterated Hilbert transforms

In principle the perturbed phase equations Eqs. (4.12) and (4.13) are valid also for other embedding types. However, the application of the iterated Hilbert transform Eq. (4.8) provides a mutual demodulation while other methods - although equally eligible for the construction of embeddings - would result in unstable iterations (see the info box).

Iterated derivative embeddings and analytic protophase

Similar to IHTE, iterations of the derivative embedding can be analysed. As an example here $\theta^{(a)}(t)$ is considered and the simple waveform $S_1(\phi) = \cos(\phi)$. For the analysis, one replaces the operator $\hat{H}[X_1](t)$ by $\dot{X}_1(t)$ in Eq. (4.12) and obtains the residue of phases

$$\Delta^{(a)}(t) = \phi(t) - \theta^{(a)}(t) = \varepsilon q(t) - \varepsilon \frac{(\ddot{S}_1 S_1 - \dot{S}_1^2) q + \dot{S}_1 S_1 \dot{q}}{S_1^2 + \dot{S}_1^2} = 2\varepsilon q(t) + \frac{\varepsilon \sin(2t)}{2} \dot{q} \,.$$

Application of the Fourier transformation to this equation results in its spectral representation

$$\mathcal{F}_{\Delta^{(a)}}(\omega) = 2\mathcal{F}_q(\omega) + \frac{\omega - 2}{4} \mathcal{F}_q(\omega - 2) - \frac{\omega + 2}{4} \mathcal{F}_q(\omega + 2) \,.$$

Importantly, it can be seen that components at frequency ω are amplified and that components which are shifted from frequencies $\omega \pm 2$ are additionally amplified if $|\omega| > 2$. Thus, iterations based on derivative embeddings necessarily fail and are particularly unstable for wideband signals.

Before discussing the spectral properties of IHTE, further preparation is needed. First, the results for the simple waveform $\cos(\phi)$ are

$$\Delta^{(a)}(t) = \varepsilon \left(q(t) + \cos(t) \hat{H}[q \sin](t) - q(t) \sin^2(t) \right) \,, \tag{4.14}$$

$$\dot{\Delta}^{(d)}(t) = \frac{\varepsilon}{2} \left(\dot{q}(t) + \cos(2t) \dot{q}(t) - \sin(2t) q(t) + 2\cos(t) \left(\hat{H}[\dot{q} \sin](t) + \hat{H}[q \cos](t) \right) \right) \tag{4.15}$$

Here, to get rid of the integration, $\Delta^{(d)}(t)$ is differentiated.

Second, there appear product terms $\hat{H}[q \sin](t)$, $\hat{H}[\dot{q} \sin](t)$ and $H[q \cos](t)$ in Eqs. (4.14), (4.15) which deserve further treatment by means of the Bedrosian identity Eq. (3.10): Without loss of generality, the modulation $q(t)$ can be represented by a sum

$$q(t) = q_h(t) + q_l(t) \tag{4.16}$$

where $q_l(t)$ corresponds to the slow modulation spectrum $\mathcal{F}_{q_l}(\omega)$ in domain $|\omega| \leq 1$ (narrowband modulation) and $q_h(t)$ corresponds to the fast modulation spectrum $\mathcal{F}_{q_h}(\omega)$ in domain $|\omega| > 1$ (wideband modulation)[11].

---

[11] Slow modulations and fast modulations are separated here by $\langle \dot{\phi} \rangle_t = 1$.

Inserting the separation Eq. (4.16) and applying the Bedrosian theorem[12], it follows

$$\begin{aligned}\Delta^{(a)}(t) = &\frac{\epsilon}{2}q_h(t) + \frac{\epsilon}{2}\left(q_h(t)\cos(2t) + \sin(2t)\hat{H}[q_h](t)\right) \ , \\ \dot{\Delta}^{(d)}(t) = &\frac{\epsilon}{2}\Big(\dot{q}_h(t) + \hat{H}[q_h](t) + \cos(2t)\left(\dot{q}_h(t) + \hat{H}[q_h](t)\right) \\ &+ \ \sin(2t)\left(\hat{H}[\dot{q}_h](t) - q_h(t)\right)\Big)\end{aligned}$$

In Fourier space, these equations are given by

$$\begin{aligned}\mathcal{F}_{\Delta^{(a)}}(\omega) = &\frac{1}{2}\left[\mathcal{F}_{q_h}(\omega) + \frac{1}{2}(1-\mathrm{sgn}(\omega-2))\mathcal{F}_{q_h}(\omega-2) + \frac{1}{2}(1+\mathrm{sgn}(\omega+2))\mathcal{F}_{q_h}(\omega+2)\right] \ , \\ \mathcal{F}_{\Delta^{(d)}}(\omega) = &\frac{1}{2}\Bigg[\frac{\omega-\mathrm{sgn}(\omega)}{\omega}\mathcal{F}_{q_h}(\omega) + \left(\frac{\omega-1}{2\omega}(1-\mathrm{sgn}(\omega-2))\mathcal{F}_{q_h}(\omega-2) \ + \right. \\ &\left.\frac{\omega+1}{2\omega}(1+\mathrm{sgn}(\omega+2))\mathcal{F}_{q_h}(\omega+2)\right)\Bigg] \ .\end{aligned} \tag{4.17}$$

A major simplification of the spectral representation can be found from the fact that the spectrum $\mathcal{F}_{q_h}(\omega)$ vanishes in the domain $|\omega| < 1$. The resulting spectral transfer equations are given then by

$$\mathcal{F}_{\Delta}(\omega) = \begin{cases} A(\omega)\mathcal{F}_{q_h}(\omega) + B(\omega)\mathcal{F}_{q_h}(\omega+2) & \text{if } \omega > 1 \ , \\ B(\omega)\mathcal{F}_{q_h}(\omega+2) + A(\omega)\mathcal{F}_{q_h}(\omega-2) & \text{if } -1 < \omega < 1 \ , \\ B(\omega)\mathcal{F}_{q_h}(\omega) + A(\omega)\mathcal{F}_{q_h}(\omega-2) & \text{if } \omega < -1 \ , \end{cases} \tag{4.18}$$

where

$$\begin{aligned} A(\omega) = B(\omega) = 1/2 \text{ for the analytic phase and } \Delta^{(a)}, \\ A(\omega) = \frac{\omega-1}{2\omega}, \ \ B(\omega) = \frac{\omega+1}{2\omega} \text{ for the length-based phase and } \Delta^{(d)}. \end{aligned} \tag{4.19}$$

Relation (4.18) can be considered as a transformation of the residual phase modulation at a step of the iteration procedure. Denoting the spectrum of the high-frequency modulation $\varepsilon q_h(t)$ at the n-th step of IHTE as $\mathcal{F}_n(\omega)$, a general recursion formula for the evolution of the spectrum under iterations is:

$$\mathcal{F}_{n+1}(\omega) = \begin{cases} A(\omega)\mathcal{F}_n(\omega) + B(\omega)\mathcal{F}_n(\omega+2) & \text{if } \omega > 1, \\ B(\omega)\mathcal{F}_n(\omega+2) + A(\omega)\mathcal{F}_n(\omega-2) & \text{if } -1 < \omega < 1, \\ B(\omega)\mathcal{F}_n(\omega) + A(\omega)\mathcal{F}_n(\omega-2) & \text{if } \omega < -1. \end{cases} \tag{4.20}$$

This relation is the main result of the upper analysis. Next, a discussion of its meaning is presented (where focus is put on positive frequencies due to evident symmetry).

- In both cases of protophase approximation, slow modulations are resolved exactly already in the first iteration: If the spectrum $\mathcal{F}_0$ lies in the interval $|\omega| \leq 1$, then $\mathcal{F}_1 = 0$. This is a well-known empirical fact and corresponds to the demodulation of narrow band signals while for wideband signals demodulation is not exact (see App. A.4 for a comparison of Hilbert transform and quadrature). This efficiency of the Hilbert embedding is valid, according the presented linear theory, for $\theta^{(a,d)}(t)$. Noteworthy, this result is derived for very weak modulation only, while the IHTE-algorithm is applicable also to stronger low-frequency modulation, where one indeed needs several iterations to achieve a good demodulation (see Fig. 4.7).

---

[12] For example, $\hat{H}[(q_h + q_l)\cos](t) = \hat{H}[q_h](t)\cos(t) + q_l(t)\sin(t)$.

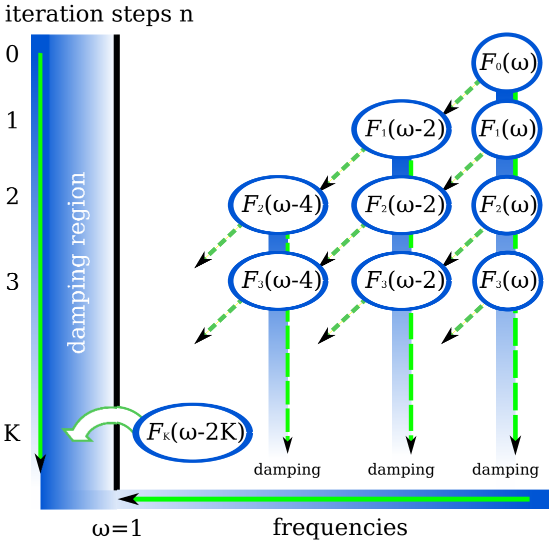

Figure 4.5: Depicted is the damping of Fourier modes in the range $2K < \omega < 2K + 2$ for the simple waveform $S_1(\varphi)$. In each iteration step, the method damps $\mathcal{F}_n(\omega)$ (dashed vertical arrows) and additionally generates a new Fourier mode at a smaller frequency (dashed diagonal arrows). At step K, a Fourier mode with frequency less than 1 is generated in the low-frequency region (bold green-white arrow), where it disappears at the next iteration. The damping factors are given by Eq. (4.19).

- Contrary to low-frequency components, the high-frequency components do not disappear immediately: if $\mathcal{F}_0(\omega) \neq 0$ for $|\omega| > 1$, then $\mathcal{F}_1 \neq 0$. According to Eq. (4.20), at each iteration step, there are two processes: (i) the harmonics at frequency ω is multiplied by factor $A(\omega)$ and (ii) there is a spectral transfer toward lower frequencies $\omega \to \omega - 2$, with the corresponding factor $B(\omega)$. Important is that both of these factors are less than one. Schematically, this is illustrated in Fig. 4.5. This scheme shows that for all spectra decaying at infinity, i. e. with $\lim_{\omega\to\infty} |\mathcal{F}_0(\omega)| = 0$, the erroneous modulation eventually disappears, i. e. $\lim_{n\to\infty} |\mathcal{F}_n(\omega)| = 0$. For some important classes of spectra, one can show that the eigenvalues of the transformation operator (4.20) are smaller than one so that the iteration procedure converges exponentially. In particular, for spectra $\mathcal{F}_{q_h}(\omega)$ which decay exponentially $\mathcal{F}_{q_h}(\omega) \sim \exp(-\iota\omega)$ (what corresponds to a smooth modulation $q_h(t)$), it follows $|\mathcal{F}_n| \sim \left(\frac{1+\exp(-2\iota)}{2}\right)^n \underset{n\to\infty}{\to} 0$.
- In the upper analysis components of modulation with frequencies $1, 3, 5, \ldots$, i. e. harmonics of the basic oscillation frequency are not considered. Such components can not be demodulated, because one can not distinguish them from the original phase – in fact, a modulation with these frequencies is equivalent to changes of the waveform $S(\phi)$ to a proto-waveform $\tilde{S}(\theta)$.

4.3 Testing theoretical relations

The upper analysis provides iteration maps Eq. (4.20) for the spectra of $\Delta^{(a,d)}(t)$. These spectral components are calculated and presented in Fig. 4.6 for four numerical setups. In case (a) the phase modulation is weak. Thus, the non-linear effects are indeed small and observed spectral amplitudes can be compared with theoretical predictions. In all other cases (b-d) relatively strong modulations are present, such that the non-linear effects become dominant.

As an example, a modulated phase

$$\phi(t) = t + a\sin(ft) + b\cos(gt) \tag{4.21}$$

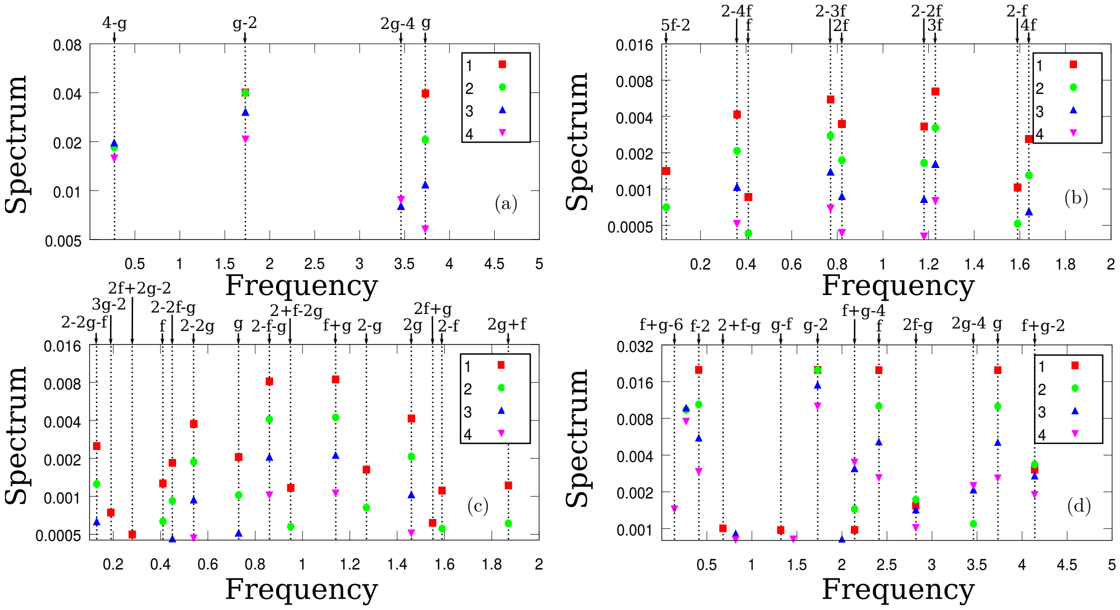

Figure 4.6: Depicted are most essential spectral components of the phase demodulation error $\Delta_n^{(a)}(t)$ for the first four iterations (squares, circles, up and bottom triangles, respectively). The observed spectral components are marked with arrows on top of the figures. The vertical scale is logarithmic, with the ticks marking factor 2. This allows a visual comparison of results as the theoretic damping factors are 1/2.

with two stationary modulation frequencies f and g is considered. IHTE are performed as exemplified in Fig. 4.4 – here for the analytic protophase proxi $\theta^{(a)}(t)$ Eq. (3.6).

- Panel (a) of Fig. 4.6 shows the case $a = 0$, $b = 0.2$, $g = 3.73$ of a single-harmonic modulation with high frequency components $\mathcal{F}_0(\pm g)$. Here the modulation is relatively weak such that the theoretical relations Eq. (4.20) hold. Indeed, at the first iteration two equal components $\mathcal{F}_1(\pm g) = \frac{1}{2}\mathcal{F}_0(\pm g)$ and $\mathcal{F}_1(\pm g \mp 2) = \frac{1}{2}\mathcal{F}_0(\pm g)$ appear (red squares in Fig. 4.6). In the second iteration: $\mathcal{F}_2(\pm g) = \frac{1}{4}\mathcal{F}_0(\pm g)$; $\mathcal{F}_2(\pm g \mp 2) = \frac{1}{2}\mathcal{F}_0(\pm g)$, and $\mathcal{F}_2(\pm g \mp 4) = \frac{1}{4}\mathcal{F}_0(\pm g)$ (green filled circles). In the third iteration: $\mathcal{F}_3(\pm g) = \frac{1}{8}\mathcal{F}_0(\pm g)$; $\mathcal{F}_3(\pm g \mp 2) = \frac{3}{8}\mathcal{F}_0(\pm g)$, and $\mathcal{F}_3(\pm g \mp 4) = \frac{1}{4}\mathcal{F}_0(\pm g)$ (blue triangles). And in the fourth iteration: $\mathcal{F}_4(\pm g) = \frac{1}{16}\mathcal{F}_0(\pm g)$; $\mathcal{F}_4(\pm g \mp 2) = \frac{1}{4}\mathcal{F}_0(\pm g)$, and $\mathcal{F}_4(\pm g \mp 4) = \frac{3}{16}\mathcal{F}_0(\pm g)$ (magenta downside triangles). In addition, weak non-linear components at frequency $2g - 4$ arise. These are the result of frequencies $2g$ and $2g - 2$ outside the shown frequency range.

- Panel (b) illustrates non-linear effects at a strong low-frequency single-harmonic modulation. Here $a = 1$, $f = 0.41$, and $b = 0$. Although the frequency of modulation is smaller than the base frequency $\omega = 1$, a rather small component $\mathcal{F}_1(f)$ remains, contrary to the prediction of linear theory. In the first iteration, higher harmonics nf and the combinational frequencies $nf - 2$ appear which are relatively large. During next iterations the amplitudes of these components decrease with a factor $\approx 1/2$. One can see that the first iterations are dominated by non-linear effects, and at this stage the spectrum broadens. Only subsequent iterations lead to decrease of the Fourier components.

- Panel (c) shows the spectra of a relatively strong two-frequency modulation, where both frequencies are low: $a = b = 0.3$, $f = 0.41$, $g = 0.73$. Due to non-linearity, many combinational frequencies $kf + lg$, $kl + fg - 2$ with integers k and l are exited. It appears that all the new frequencies, like in case (b), are created in the first iteration while further iterations roughly follow Eq. (4.20).
- Panel (d) shows, like case (c), a strong two-frequency modulation, but with high basic frequencies $a = b = 0.1$, $f = 2.41$, $g = 3.73$. One can see that at some combinational frequencies, the level even initially increases due to the cascade process of amplitude shifting (see, e.g. components with $f + g - 4$). For these components, more iterations are needed to reduce error.

In conclusion, the presented numerical tests show that the theory based on the linear approximation works well for weak modulation. In contrast, for strong modulation, essential non-linear effects are present at the first few iterations. Consequently, because the effective modulations become weaker over the course of iterations, higher iterative steps are better described by the theoretic relations.

4.4 Reconstruction of strong wideband modulations - a numerical study

In this section, the convergence of IHTE for strong wideband modulations is explored in more detail. For this, parameters in Eq. (4.21) with $a = b = 0.3/s$, $f = \sqrt{2}s$ and $g = \sqrt{3}s$ are considered. The parameter s allows to vary the modulation frequencies while the range of the phase modulation remains constant. The latter is quite large ($\min(d\phi/dt) = 1 - a(f + g) \approx 0.056$) such that first-order theoretical analysis of Sec. 4.2 is not applicable.

Additionally, a signal

$$X_2(t) = S_2(\phi(t)), \qquad S_2(\phi) = \cos(\phi) - 0.7\sin(2\phi) + \cos(3\phi) \tag{4.22}$$

is defined as an illustrative example for demodulation of multicomponent signals (see Fig. 4.3). The resulting embeddings Fig. 4.1 (e-h) shows an additional loop such that also a protophase-to-phase transformation is needed. (For a more complicated waveform see Sec. 4.5).

The following analysis[13] characterises the performance of IHTE for different levels of modulation time scale s in dependence of signals $X_{1,2}(t)$ and protophase proxis $\theta^{(a,d)}(t)$. The convergence of the optimal periodicity errors $\mathrm{Err}^{\star}_{\theta^{(a,d)};n}$ are depicted in Fig. 4.7. It can be readily seen that both protophases result in demodulation with very small residual errors and that even for slow frequency modulations ($s < 1$), the procedure is needed and performs best. Moreover, IHTE based on $\theta^{(d)}(t)$ is superior to the method based on $\theta^{(a)}(t)$.

While for $S_1(\phi)$ analytic protophase proxis can be calculated, for $S_2(\phi)$, only the length-based protophase proxis can be used. In Fig. 4.7 all the final errors are very small. It appears however, that for values of $s \geq 2$, the only applicable phases are $\theta^{(b,c,d)}(t)$ as they ensure monotonicity while iterations based on $\theta^{(a)}(t)$ fail at one of

---

[13] The signals are observed for 95 periods with a time step of $dt = 0.002$. The periodicity error $\mathrm{Err}^{\star}_{\theta^{(a,d)};n}$ is evaluated on the inner 80% of the transformed signal to discard boundary effects.

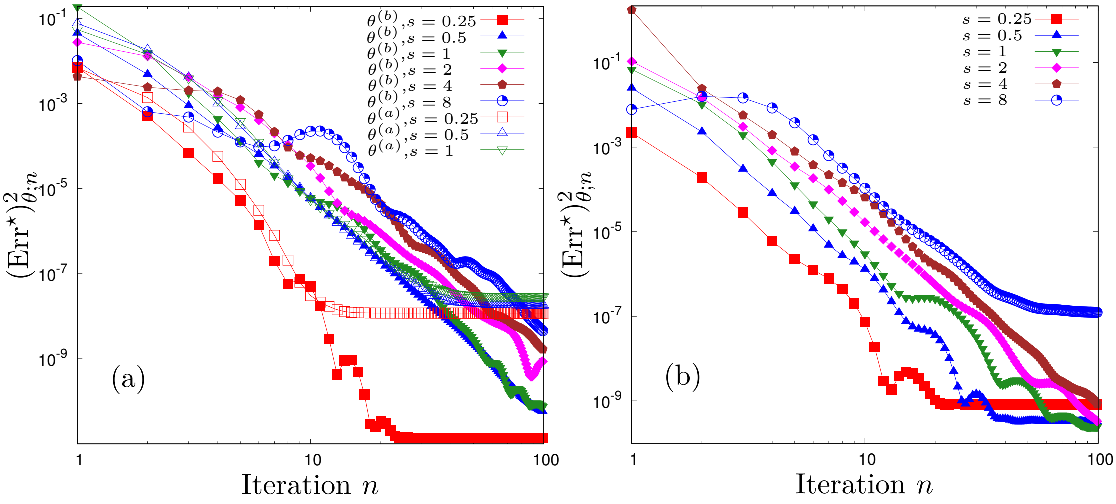

Figure 4.7: Depicted are errors of demodulation for several values of s during iteration. (a): Results for the simple waveform $S_1(\phi)$ and $\theta_n^{(a,d)}(t)$. Note that $s = [0.25; 0.5; 1]$ are depicted for both protophase proxis in the same color, but with open and filled markers respectively. For $s > 1$ the analytic protophase approximation is not suitable for reconstruction, as at high iterations it becomes non-monotonous. One can also see that the performance of the iterations is the best for the lowest considered frequency of modulation (case $s = 0.25$). (b): Results for the complex waveform $S_2(\varphi)$. Here only $\theta^{(d)}(t)$ can be used due to loops in the embedding Fig. 4.1.

the first iterations due to an approached non-monotonicity in time. Interestingly, the periodicity error decreases not monotonously with n. (For example, for $s = 8$, it increases at $n \gtrsim 10$.) This, is a direct result of the spectral shifting process described in Sec. 4.2. Nevertheless, even in these cases the error eventually becomes rather small.

The presented results confirm that the described method provides an effective demodulation of the signals. Remaining errors emanate from the numerical implementation of the Hilbert-integral Eq. (4.8), the calculation of length in the embedding plane Eq. (4.2) and from the evaluation of the periodicity error Eq. (4.6) itself. In particular, IHTE restore the $L^\star$-periodicity of $\theta_n^{(d)}(t)$ such that a projection to periods of length 2π is possible after iterations.

4.5 Generic smooth phase modulation

In the previous discussion, the average instantaneous frequency was a constant given by ω and the multicomponent signal was relatively simple. However, the IHTE can also be used to demodulate signals with quite wild instantaneous frequencies (see Eq. (3.5)) and it allows to demodulate even non-smooth waveforms formally defined through an infinite Fourier series expansion[14]. As an example, here the signal

$$X_3(t) = S_3(\phi(t)), \qquad S_3(\phi) = \frac{1}{6}\left[\cos(2\phi) + \sum_{j=1}^{4}\cos(j\phi) + \sin(j\phi)\right] \tag{4.23}$$

---

[14] For further examples see [161].

with an instantaneous frequency

$$\begin{aligned}\Omega(t) = \omega - 1 + 0.15\Big[\sqrt{5}\cos(\sqrt{5}t) + \sqrt{3}\sin(\sqrt{3}t)\Big] \\ + 3\exp\Big[-(t-250)^2/10^4\Big] - \tanh\Big[(t-450)/10\Big]\end{aligned} \tag{4.24}$$

is discussed.

The signal contains 4 peaks per period which account for a relatively complex embedding with 4 loops in Fig. 4.8. The frequency $\Omega(t)$ is depicted in Fig. 4.8 (a) and resembles a band due to the first two terms which contain fast isolated and stationary harmonics. In contrast, the last two terms in Eq. (4.24) result in a relatively slow variation of the effective bandwidth: While at the boundaries, a signal period contains several periods of the fast stationary modes, in the central part of the time series, the local value of $\langle\dot{\phi}\rangle_t$ rises such that more of the quadrature conditions (see App. A.4) are satisfied by the modulation spectrum. Thus, in the central part of the time series, the first Hilbert transform $\hat{H}[X_{1,3}](t)$ is a reasonable approximation of the quadrature. Indeed, this can be observed for $\Delta_1^{(b)}(t) = \phi(t) - \theta_1^{(b)}(t)$ (blue band in (a)) which shows a significant drop of complexity in the central region.

Iterations are performed using $\theta^{(b,c,d)}(t)$. The corresponding demodulation errors indicate that all of the three methods provide a good demodulation for $X_{1,3}(t)$. Noteworthy, although the initial modulation level is relatively small (0.1), the iterative procedure is needed as the first embedding resembles a wide band.

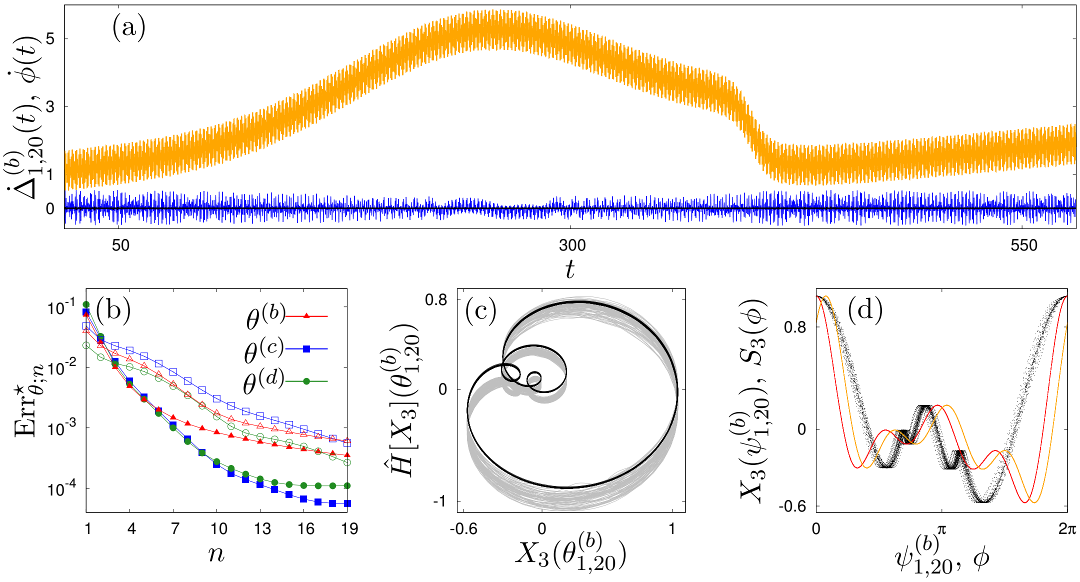

Figure 4.8: (a): Depicted is the instantaneous frequency Eq. (4.24) (orange) and frequency residues $\dot{\Delta}^{(b)}_{1,20}(t)$ in the first step (blue) and in step 20 (black) for the simple signal $X_1(t)$. (b): Shown are the demodulation errors $\mathrm{Err}^{\star}_{\theta^{(b,c,d)};n}$ for $\theta^{(b,c,d)}$ in red, blue and green respectively. Filled markers indicate results for $X_3(t)$ while empty markers correspond to $X_1(t)$. (c): Presented is the embedding after one iteration (grey) and after 20 iterations (black) for $X_3(t)$. The corresponding true waveform (orange) is depicted in (d). Also shown are the waveform in the first iteration (band of black points) and the final result after 20 iterations (red). Results in (c, d) are based on $\theta^{(b)}(t)$.

Chapter 5

Phase reconstruction with iterated Hilbert transform embeddings

Bibliographic information

The main results in this chapter have been published in:

Erik Gengel and Arkady Pikovsky
Phase reconstruction with iterative Hilbert transform embeddings
Physics of biological oscillators: Ch. 12, Springer (2021)

Main findings:

- Phase reconstruction based on iterative Hilbert transform embeddings of generic observables for the SL oscillator
- Reconstruction of the infinitesimal phase response curve for the SL oscillator
- Exploration of phase reconstruction performance for noise driven phase dynamics

5.1 Forced Stuart-Landau oscillator and observables

In this chapter, the performance of IHTE is explored for generic observables of a forced oscillator. The goal is, to present the benefits of IHTE analysis for subsequent phase-model reconstruction and to show limitations of the approach with regard to the true modulations of the system.

Here, the phase dynamics of the SL oscillator is reconstructed. Based on the obtained phases, the first-order phase model Eq. (1.6) is inferred. The considered oscillator equations is

$$\dot{a} = (\mu + i\nu)a - (1 + i\alpha)a|a|^2 + i\varepsilon p(t) + i\zeta(t), \qquad p(t) = \cos(\eta(t)) \qquad \eta(t) = s\omega t \;. \quad (5.1)$$

It is in full correspondence to the model of high-order phase-reduction theory of Ch. 2.3 where here a scaling is chosen such that the amplitude of the stable limit cycle $\sqrt{\mu}$ and the natural frequency $\omega = \nu - \alpha\mu$ depend on parameters of the system[1].

The external stimulus comprises a harmonic forcing term $p(t)$ of amplitude ε depending on a phase $\eta(t)$ with tunable frequency according to the parameter s and a stochastic term, $\zeta(t)$ which is used to emulate randomness in an observed system.

---

[1] The amplitude dynamics is given by $\dot{r} = r(\mu - r^2) + \varepsilon p(t)\sin(\theta)$

The system dynamics is observed through the generic observables

$$\begin{aligned} X_4(t) &= \hat{M}_4[u,v](t) = u(t) \\ X_5(t) &= \hat{M}_5[u,v](t) = 0.1v^2(t) + 0.2u^2(t) + 0.3v(t) + 0.4u(t) \\ X_6(t) &= \hat{M}_6[u,v](t) = X_5(t) + 0.3u(t)v(t) \; . \end{aligned} \tag{5.2}$$

Here, $u(t) = \Re[a](t)$ and $v(t) = \Im[a](t)$. The observable $X_4(t)$ resembles cosine oscillations. The observable $X_5(t)$ depends in a more complex way on $a(t)$ but it also has just one maximum and one minimum in a period. In contrast, the observable $X_6(t)$ is a multi-component signal with two maxima in a period. Thus, generalised proto waveforms $X_{5,6}(\theta)$ possess additional 2π-periodic modulations.

The signals contain additional amplitude modulations whose strength depends on the parameter μ. For small μ these modulations are significant and an accurate demodulation based on IHTE is not possible. In contrast, Fig. 5.1 depicts snapshots of the signals $X_{5,6}(t)$ and the resulting generalised waveforms $X_{5,6}(\varphi)$ for large μ. Indeed, since amplitude modulations are present, these functions mutually resemble bands which are sufficiently narrow. For these generalised waveforms, a demodulation can be successful. (For a comparison see Fig. 4.3 where $S_2(\varphi)$ is a perfect line and can generally be recovered from data).

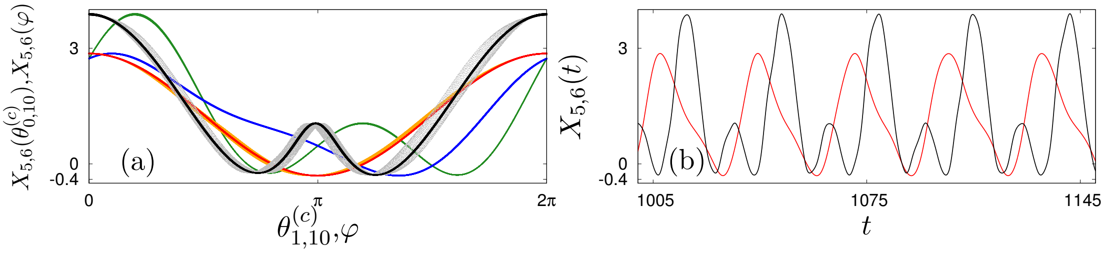

Figure 5.1: Panel (a): Generalised waveforms for $X_5(\varphi)$ (blue) and $X_6(\varphi)$ (green). The fact that these sets of points are indistinguishable from a line demonstrates validity of the phase description for the SL oscillator (i. e. the amplitude modulation is indeed small). The waveforms of the first protophase $\theta_1^{(c)}(t)$ are not lines but broad sets (orange for $X_5(\theta_1^{(c)})$ and grey for $X_6(\theta_1^{(c)})$). The same waveforms become nearly 2π-periodic functions of the protophase $\theta_{10}^{(c)}(t)$ after ten iterations of IHTE (red and black points, correspondingly). Panel (b): Time series for observables $X_{5,6}(t)$ (red, black). Simulation parameters are $\mu = 8$, $\alpha = 0.1$, $\nu = 1$, $\varepsilon = 0.1$ and $s = 1.8$ (for $X_5(t)$) and $s = 5.6$ (for $X_6(t)$). A harmonic forcing $\varepsilon p(t) = \varepsilon \cos(\eta(t))$ is used here. In this scale, small amplitude and phase modulations are hardly seen.

5.2 Numerical results

5.2.1 Reconstruction of deterministic phase dynamics

In the following, the dynamics Eq. (5.1), receives an external harmonic perturbation with $\varepsilon p(t) = \varepsilon \cos(\eta(t))$. The frequency of the driving, $s\omega$, is tuned to cover a wide range of slow and fast external frequencies. It is chosen such that the system[2] stays asynchronous with the forcing during observation.

For the reconstruction of the phase dynamics Eq. (1.6), the spline-based protophase proxi $\theta^{(c)}(t)$ is obtained from signals $X_{4,5,6}(t)$ using IHTE (see Fig. 4.4). Then, in each

---

[2] The system parameters are $\mu = 8$, $\alpha = 0.1$, $\nu = 1$, $\varepsilon = 0.1$.

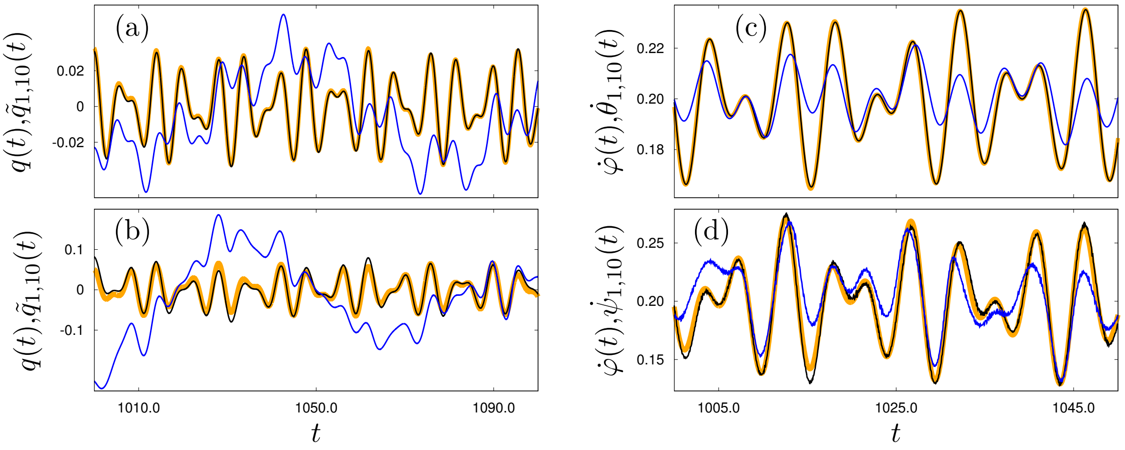

Figure 5.2: Comparison of true modulation $q(t)$ and of true instantaneous frequency $\dot{\varphi}(t)$ (orange) with the corresponding iteration results $\tilde{q}_n(t)$ in the first step (blue) and in the 10th step (black) for the observables $X_4(t)$ (a,c) and $X_6(t)$ (b,d). Parameters are $\mu = 8$, $\alpha = 0.1$, $\nu = 1$, $\varepsilon = 0.1$ and $r = 5.6$. For calculation of the phase derivatives a $\mathrm{SG}_{12,25,4}$ filter is employed.

step[3] DPT is employed to construct $\psi^{(c)}(t)$. Figure 5.2 shows a successful recovery of the actual phase dynamics for a quite large forcing frequency with $s = 5.6$. These results indicate that the phase reconstruction for non-linear oscillators is indeed inaccurate in the first Hilbert transform based on time while iterations restore the phase dynamics for the two observational signals $X_{4,6}(t)$.

The instantaneous frequency in Fig. 5.2 is estimated from the reconstructed phases by means of a Savitzky-Golay filter. The filter is defined by its order w_1 of the fitting polynomial on a window of $w_2 > w_1 + 1$ raw data points, symmetric around t [174]. To achieve a good reduction of any present noise, the signal is passed w_3 times through the filtering process. The parameter setting[4] is denoted by $\mathrm{SG}_{w_1,w_2,w_3}$.

The similarity of reconstructed and actual phase is quantified by the integrated residues of phases $\Delta_n(t) = \varphi(t) - \psi_n(t)$ and instantaneous frequencies $\dot{\Delta}_n(t) = \dot{\varphi}(t) - \dot{\psi}_n(t)$. The resulting similarity errors

$$\begin{aligned} \mathrm{STD}_n^{\psi} &= \sqrt{\frac{1}{\hat{N}_1}\int_{t_0}^{t_m}[\varphi(\tau)-\psi_n(\tau)]^2 d\tau} & \mathrm{STD}_n^{\dot{\psi}} &= \sqrt{\frac{1}{\hat{N}_2}\int_{t_0}^{t_m}[\dot{\varphi}(\tau)-\dot{\psi}_n(\tau)]^2 d\tau} \\ \hat{N}_1 &= \int_{t_0}^{t_m}(\varphi(\tau)-\tilde{\omega}\tau)^2 d\tau & \hat{N}_2 &= \int_{t_0}^{t_m}[\dot{\varphi}(\tau)-\tilde{\omega}]^2 d\tau \end{aligned} \tag{5.3}$$

are a measure for the spectral power of the residual modulation in the approximated phases[5].

Figure 5.3 depicts the course of the similarity errors under iteration for several slow and fast modulation frequencies: While for slow modulations ($s < 1$), the reconstruction is already accurate in the first step, for fast forcing frequencies ($s > 1$) indeed, several

---

[3] Here, 20 iterations suffice. For the reconstruction, 100 periods of oscillation with a time step of $dt = 0.01$ are observed. The summation in the DPT Eq. (3.23) is truncated at 1000 modes.

[4] Instead of fixed standard parameters, a generic least-square polynomial fit is used. This is necessary since interpolation of marker events, t_j, introduces variations in the time stepping.

[5] The normalisation constant $\hat{N}_{1,2}$ assumes average linear growth of $\varphi(t)$ according to the frequency $\tilde{\omega}$. The latter is estimated from protophase by a linear least square fit. Boundary effects in the first and last 10% are discarded.

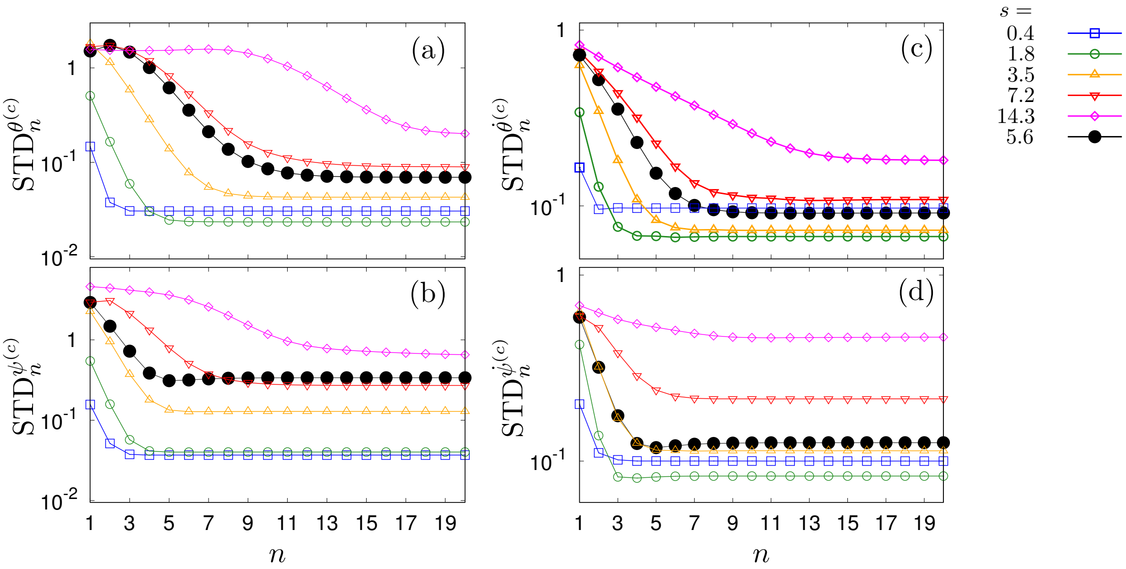

Figure 5.3: Phase and frequency errors for observables X_4 (a, c) and X_5 (b, d) for different forcing frequencies $s\omega$. Also shown in (b, d black doted line) is the reconstruction error for $X_6(t)$, where the use of length, $L(t)$, for phase calculation is crucial. Slow modulations are essentially reconstructed in the first step while fast modulations need at least several iterations. With increased forcing frequency, $\theta_n^{(c)}(t)$ differs significantly from $\varphi(t)$ and the number of needed iterative steps grows.

iterations are needed for precise reconstruction. However, essentially in all the considered cases, iterations decrease errors of the first commonly used phase approximations by a factor of ten or even more!

5.2.2 Reconstruction of the phase response curve

As an example, for potential benefits of IHTE in subsequent phase-based data analysis, the coupling function is recovered from observations of the SL system through $X_4(t)$. System parameters are similar to Sec. 5.2.1. In particular, here fast modulations ($s \in [4.5, 5.6]$) are considered in addition to slow modulations ($s = 0.06$, Fig. 5.5).

Since the system Eq. (5.1) is perturbed by a periodic force $\varepsilon p(t) = \varepsilon \cos(\eta(t))$, the actual coupling function, $q(t) = Q(\varphi(t), \eta(t))$, is a 2π-periodic function of its arguments. Thus, given a phase approximation $\psi_n(t)$ and the external force phase $\eta(t)$, an approximate coupling function

$$\begin{aligned}\tilde{Q}_n(\tilde\varphi, \tilde\eta) &= \frac{\sum_{k=0}^{K}\left[\dot\psi_n(\psi_{n;k}, \eta_k) - \tilde\omega\right]\mathbb{K}_\kappa(\tilde\varphi - \psi_{n;k}, \tilde\eta - \eta_k)}{\sum_{k=0}^{K}\mathbb{K}_\kappa(\tilde\varphi - \psi_{n;k}, \tilde\eta - \eta_k)}\\ \mathbb{K}_\kappa(x, y) &= \exp[\kappa(\cos(x) + \cos(y) - 2)]\end{aligned}$$

is estimated by a Kernel-density fit[6] of $\dot\psi_n(\psi_n, \eta)$ onto a $2\pi \times 2\pi$-periodic lattice of $\tilde\varphi, \tilde\eta$ [163]. Figure 5.4 presents the results of this fit.

The true iPRC $Z(\varphi)$, follows directly from differentiation of Eq. (2.9) with respect to the coordinate in the direction of forcing ($v = \Im[a]$):

$$Z(\varphi) = \frac{\partial \Phi[\mathbf{y}]}{\partial v} = \frac{\partial \theta}{\partial v} - \alpha\frac{\partial \ln[r]}{\partial v} = \frac{u}{u^2+v^2} - \alpha\frac{v}{u^2+v^2} = \frac{\cos(\theta) - \alpha\sin(\theta)}{\sqrt{\mu}}\,. \tag{5.4}$$

---

[6] Parameter κ determines the fitting radius. Here, $\kappa = 200$.

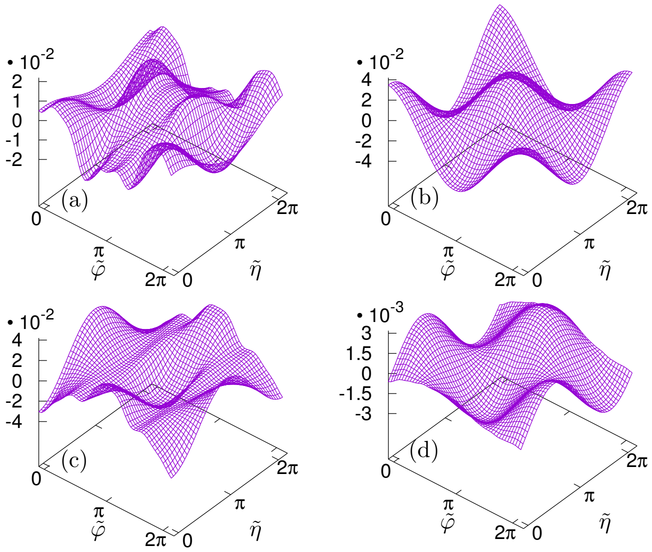

Figure 5.4: Reconstructed coupling functions $\tilde{Q}_1(\tilde{\varphi},\tilde{\eta})$ (panel (a)) and $\tilde{Q}_{10}(\tilde{\varphi},\tilde{\eta})$ (panel (b)) based on $\theta_1^{(c)}(t)$ and $\theta_{10}^{(c)}(t)$, respectively. The reconstruction error for the first iteration $\tilde{Q}_1(\tilde{\varphi},\tilde{\eta}) - Q(\tilde{\varphi},\tilde{\eta})$ is shown in panel (c), and for the 10th iteration $\tilde{Q}_{10}(\tilde{\varphi},\tilde{\eta}) - Q(\tilde{\varphi},\tilde{\eta})$ in panel (d). Noteworthy, the vertical scale in panel (d) is more than ten times smaller than in panel (c)!

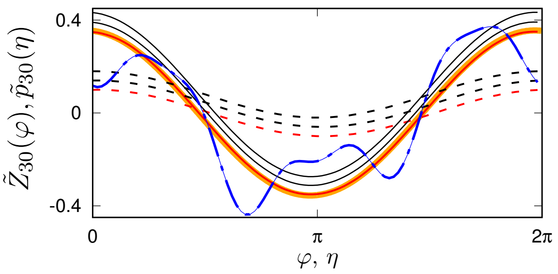

Figure 5.5: Given in orange is $Z(\varphi)$ Eq. (5.4). The blue line depicts the estimation of $\tilde{Z}_{30}(\varphi)$ based on $\theta_1^{(c)}(t)$ for $s = 5.6$. Also shown are estimates $\tilde{Z}_{30}(\varphi)$ (solid line) and $\varepsilon\cos(\eta)$ (dashed line) based on $\theta_{10}^{(c)}(t)$ for $s \in [0.06, 4.5, 5.6]$ (top to bottom). Red lines refer to the coupling functions in Fig. 5.4.

For a data-driven decomposition, an iterative factorisation procedure[7] is applied making use of the phase model Eq. (1.6) [98]. The obtained external force $\tilde{p}_{30}(\eta)$ and iPRC $\tilde{Z}_{30}(\varphi)$ are depicted in Fig. 5.5.

From visual inspection of both figures, it can be seen that the phase-model reconstruction based on a phase approximation $\psi_{10}^{(c)}(t)$ of IHTE is superior to the commonly used first phase approximation $\psi_1^{(c)}(t)$. In fact, for $\psi_1^{(c)}(t)$, deviations of the coupling function are of the same order as the original model while for $\psi_{10}^{(c)}(t)$, the error is reduced by a factor of more then ten (compare Fig. 5.4 (c,d)).

In regard of these encouraging results, it must be stressed that the presented performance is possible for quite large μ and smooth modulations. Moreover, the considered phase model comprises only the first harmonics of the phase. While the methods robustness with regard to different model complexity levels is discussed in Ch. 6, in the following the SL model is considered further to illustrate the IHTE performance for noisy signals.

5.2.3 Phase reconstruction of noise modulated phase dynamics

The embedding and reconstruction of stochastic components of a system dynamics renders an important aspect of oscillatory data analysis. On the one hand, no stochastic

---

[7] External force and iPRC are determined up to a factor since iPRC and external force appear as a product in Eq. (1.6). It is chosen such that the amplitude of the forcing is ε. The scheme is iterated for 30 steps.

embedding theorem exists. On the other hand, dynamic noise can activate oscillations or causes structurally uncoupled systems to synchronise [175, 176]. However, according to the convergence theory Sec. 4.2, IHTE demodulations are meaningful if the modulation spectra are bounded or decay exponentially fast at infinity what is usually not the case for stochastic oscillators. Thus, the goal of this section is to examine the noise sensitivity of IHTE.

White Gaussian noise

White Gaussian noise possesses an unbounded spectrum such that the spectral transfer operation Eq. (4.20) is not convergent. Moreover, unbounded noise results in infinitely many small loops in an embedding. Thus, the length definition Eq. (4.2) is not applicable as the embedding resembles a fractal curve.

As an example, the SL system Eq.(5.1) is driven by a harmonic force and Gaussian white noise with amplitude σ and zero mean[8]:

$$p(t) = \cos(5.6\omega t), \qquad \langle\zeta\rangle_t = 0, \langle\zeta(t), \zeta(\tilde{t})\rangle_t = \sigma^2\delta(t-\tilde{t}) \ . \tag{5.5}$$

To overcome the problem of the unbounded noise, the initial raw data of the system,

---

[8] The system parameters are $\mu = 8$, $\alpha = 0.1$, $\nu = 1$, $\varepsilon = 0.2$, $\sigma \in [0.06, 0.08, 0.1]$.

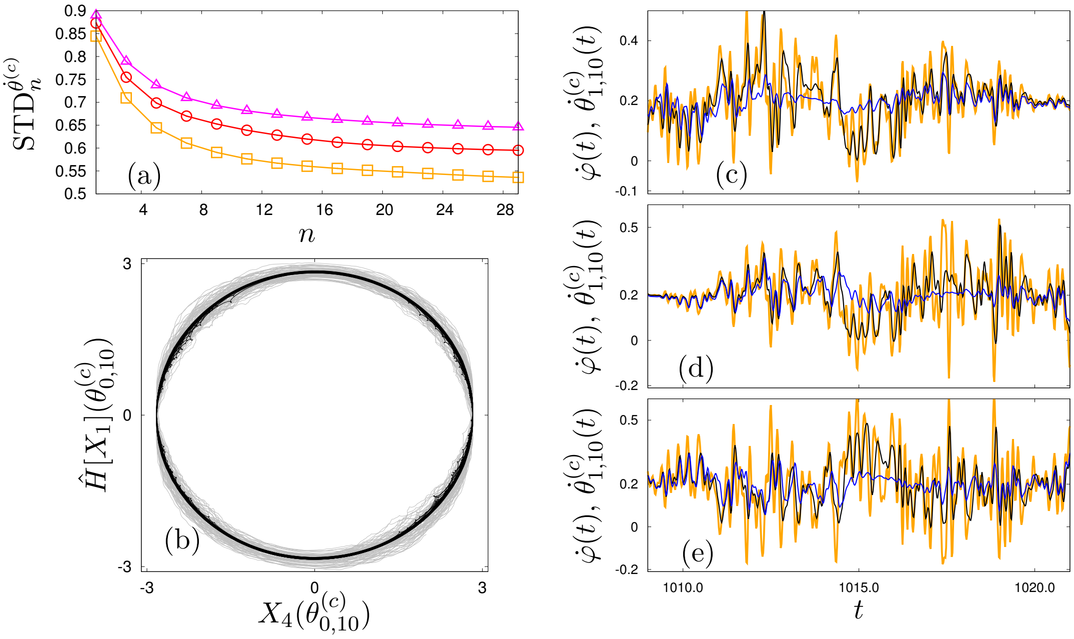

Figure 5.6: Phase reconstruction for the SL system with $\mu = 8$, $\alpha = 0.1$, $\nu = 1$, $\varepsilon = 0.2$ and $s = 5.6$. The system is observed by $X_4(t)$. Panel (a): Errors of frequency reconstruction for $\sigma \in [0.06, 0.08, 0.1]$ (squares, circles, triangles). Panel (b): First Hilbert embedding (grey) and the last embedding at step $n = 10$ (black). Note that there are still small scale loops present as a result of the remaining noise influence in $X_4(t)$. Panels (c, d, e): Snapshots of the instantaneous frequency $\dot\varphi(t)$ (orange), and of the reconstructed frequencies $\dot\theta^{(c)}_1(t)$ (blue) and $\dot\theta^{(c)}_{10}(t)$ (black) for σ as in (a). Note that $\dot\varphi(t)$ can be negative as an effect of noise, while all reconstructions obey the condition set by Eq. (3.18),(I).

$\tilde{X}_4(t)$, is smoothed by a $\mathrm{SG}_{12,25,4}$ filter to obtain $X_4(t)$ (see Fig. 4.4)[9]. This essentially introduces a spectral cut-off and results in a well defined embedding curve (see Fig. 5.6 (b) where still many smaller loops are present). Similarly, the asymptotic phase $\varphi(t)$ of the system is smoothed using the same filtering parameters. Its instantaneous frequencies $\dot{\varphi}(t)$ can be negative in Fig. 5.6 (c, d, e). Therefore, a high polynomial order of smoothing is indeed needed. As a consequence, the following results have to be interpreted relatively to the smoothing parameters which are here chosen in such a way that they preserve essential local features of the dynamics.

Since all of the conditions Eqs. (3.18) and (3.19) are not fulfilled in this example, the actual phase dynamics is only partly reconstructed, as can be seen also from Fig. 5.6 (a) where the decay of reconstruction error is much less pronounced than in Fig. 5.3. Roughly, the method improves the estimation of the phase, by a factor up to 2.

Coloured Gaussian noise - sensitivity and sampling

While the SG filter is able to adapt to fluctuations on a small scale, it is not clear how sensitive IHTE in a practical setting is. Namely, Sec. 4.2 suggests that the spectral width of the IHTE is not limited as long as the modulation spectrum of the phase decays exponentially fast at a certain frequency. However, in practical circumstances, a signal is sampled in finite time and with a finite rate of $\sim 1/dt$ what introduces a maximal frequency resolution for any small-scale fluctuations.

To examine this resolution, an Ornstein-Uhlenbeck process[10] with zero mean, amplitude σ and correlation time τ_c is considered:

$$\dot{\zeta} = \frac{-\zeta}{\tau_c} + \sqrt{\frac{2}{\tau_c}}\sigma\xi(t), \qquad \langle \zeta(t)\zeta(\tilde{t})\rangle_t = \sigma^2 \exp(-|t-\tilde{t}|\tau_c^{-1}) \,. \tag{5.6}$$

The correlation time τ_c allows to tune the roughness of noise: While for small τ_c, $\zeta(t)$ contains microscopic fluctuations at high frequencies, larger τ_c results in only slow random changes of the modulation [179]. The system dynamics[11] is observed by $X_4(t)$ Eq. (5.2) with a time step of $dt = 0.01$.

A phase of the system is then reconstructed based on the raw data and based on smoothed data obtained by $\mathrm{SG}_{6,25,4}$ and $\mathrm{SG}_{12,25,4}$ filters. $\varphi(t)$ and $\dot{\varphi}(t)$ are smoothed accordingly. The iteration procedure is carried out for 20 steps. Then, in each step, phase approximations $\psi_n^{(c)}(t)$ are calculated and derivatives $\dot{\psi}_n^{(c)}(t)$ using a $\mathrm{SG}_{12,25,4}$ filter.

The frequency resolution of the SG filter depends on parameters w_1 and w_2. By fixing $w_2 = 25$ the response however, changes linearly [180]. The polynomial order of the filter determines how many moments of the local statistics are preserved by the filtering. Thus, in the raw data, all moments of the frequency $\dot{\varphi}(t)$ are present while in the filtered data, the first 12 and 6 moments are preserved respectively. By this procedure for each noise level, three accuracy levels are provided which allow to estimate the sensitivity level of IHTE. The results of the analysis are depicted in Fig. 5.7.

In (a) the phase modulation for the slowest noise $\tau_c = 5$ indicates that IHTE is able to recover long range and short range random fluctuations (inlet) of the phase dynamics.

---

[9] The simulations are carried out with a time step of $dt = 0.01$. Thus, the filtering window is 0.25 time units long.

[10] Leonard S. Ornstein (1880-1941) [177], George E. Uhlenbeck (1900-1988) [178]

[11] The system parameters are $\mu = 6$, $\alpha = 0.1$, $\nu = 1$, $\varepsilon = 0.1$, $s = 5.6$. The rescaled forcing amplitude is $(\varepsilon + \sigma)/\mu \approx 0.033$. Noise parameters are $\tau_c \in [0.01, 0.05, 0.1, 0.5, 1, 2, 5]$ with $\sigma = 0.1$.

In Fig. 5.7 (b), all frequency errors are shwon for all smoothness levels of the original noise and the three accuracy levels of filtering. Since frequency reconstruction is sensitive to deviations $\sim \mathcal{O}(dt)$, small-scale discrepancies in the reconstruction can be detected. Indeed, for the case $\tau_c = 5$ (black curves) the initially smoothed frequency and the reconstructed frequencies essentially coincide. This indicates that the IHTE approach is able to recover all features of the phase at this noise level and most of the frequency information.

The increase of fluctuation frequency of the noise is reflected by a successive increase in the spread of reconstruction errors for the three smoothing levels. This indicates that the smoothed version of $\dot{\varphi}(t)$ and the reconstructed versions of frequency $\dot{\psi}_n^{(c)}(t)$ are different. The reason for this becomes clear by inspection of Fig. 5.7 (c) where the true and reconstructed frequencies are shown for the highest fluctuation rate of $\tau_c = 0.01$ based on the raw data (orange, blue, black) and based on $\mathrm{SG}_{12,25,4}$ filter (brown, red): IHTE is able to reconstruct the harmonic component of forcing but only minor components of the frequency noise.

This allows to estimate the sensitivity of IHTE for microscopic oscillations in the phase by comparison of convergence for different filtering levels. If convergences are similar, IHTE has reconstructed all fluctuations and thus can be regarded as sensitive to

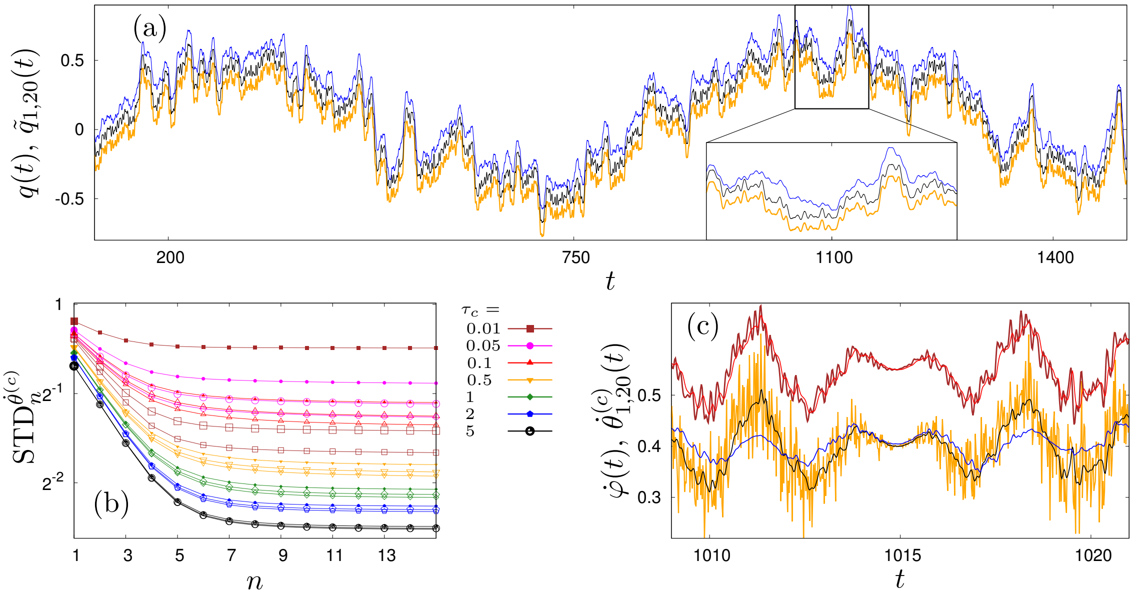

Figure 5.7: Depicted are phase reconstruction results for the SL system perturbed by a harmonic input and a coloured Gaussian noise. Model parameters are $\mu = 6$, $\alpha = 0.1$, $\nu = 1$, $\varepsilon = 0.1$, $\sigma = 0.1$, $s = 5.6$. Results are based on $X_4(t)$ obtained from two levels of smoothing: $\mathrm{SG}_{12,25,4}$ (large markers in (b)) and $\mathrm{SG}_{6,25,4}$ (medium markers in (b)). Also shown are results based on raw data $\tilde{X}_4(t)$ (solid markers in (b)). Panel (a) presents the full time series of the true modulation $q(t)$ (orange) and recovered modulations $\tilde{q}_{1,20}(t)$ (blue, black) for rather smooth noise with $\tau_c = 5$. The inlet shows a zoom of modulations around $t = 1100$. Panel (b) depicts similarity errors for all considered τ_c and all three smoothing levels. As an example for fast non-smoothed fluctuating noise, panel (c) depicts the frequencies $\dot{\varphi}(t)$ (orange) and $\dot{\theta}_{1,20}^{(c)}(t)$ (blue, black) for $\tau_c = 0.01$. Additionally, results for the $\mathrm{SG}_{12,25,4}$ filter are presented in brown ($\dot{\varphi}(t)$) and red ($\dot{\theta}_{20}^{(c)}(t)$). These curve are shifted for better visibility.

the fastest scale of these fluctuations. A visual inspection of Fig. 5.7 (b) indicates that frequencies obtained from IHTE and SG filtering roughly coincide above $\tau_c = 1$. Thus, IHTE is able to demodulate characteristic frequency components of roughly $2\pi/\tau_c \approx 15.7\omega$ at a sampling rate of $\tau_c/dt = 100$.

Telegraph noise

This section considers a proof of concept for applications in which oscillatory signals convey information about a telegraph-process. Telegraph noise occurs for example in electronic systems due to impurities [181]. It is also utilised in modelling of financial markets and biological systems [182]. Here, a telegraph process

$$\zeta(t) = \pm\sigma, \qquad \langle \zeta(t_J)\zeta(t_{J-1})\rangle = -1 \tag{5.7}$$

is considered. Then, $\zeta(t)$ mimics the jump dynamics in the stochastic SL oscillator. Additionally, $\zeta(t)$ gives at hand an illustrative example for a non-smooth phase modulation through definition of the instantaneous frequency $\dot{\phi}(t) = 1 + \zeta(t)$ in the signal $X_3(t) = S_3(\phi(t))$.

The jump amplitude of the noise is 2σ. The jumps between the two states σ and $-\sigma$ are anti-correlated and occur at jumping times t_J. As an example, the jumping-interval length $\Delta_J = t_{J+1} - t_J$ is Poissonian distributed[12] [183] according to

$$\rho_{\tau_J}(\Delta_J) = \frac{\Delta_J^2}{2\tau_J^3} \exp\left(-\Delta_J/\tau_r\right) . \tag{5.8}$$

The parameter τ_J determines how frequent jumps occur. The average jumping interval length is $3\tau_J$.

The results in Fig. 5.8 (a, c) indicate that a reconstruction of the phase information is indeed possible, given a purely phase modulated signal[13]. This is indicated by the residua $\Delta^{(c)}_{1,20}(t)$ which have been chosen to visualise the relative success of demodulation. In (a), the noise with jumping rate $\langle \Delta_J \rangle = 3/16$ oscillates fast compared to the carrier frequency. The resulting deviations of $\psi_1^{(c)}(t)$ from the actual phase are thus relatively large. On the contrary in (c), $\langle \Delta_J \rangle = 9$ what accounts for an average slow modulation and proper demodulation already in the first step. These results are accompanied by the periodicity error in Fig. 5.8 (e) for other rate parameters which indicates mutual demodulation of the signal in accordance with the results presented in Ch. 4.

In contrast, Fig. 5.8 (b, d) depicts the results for the phase reconstruction in the forced SL system. It can be seen that – although the most critic deviations are damped – a significant bottom level of fluctuations remains. This observation is underlined by Fig. 5.8 (f) where for all considered rates τ_J, the convergence of the periodicity error is much less pronounced. The main reason for this is the presence of amplitude modulations in $X_6(t)$. The generalised proto waveform $X_6(\theta)$ thus, can not obey the constraints that underlie IHTE (see Eqs. (3.13) and (3.18)). Accordingly, the *amplitude modulation level* (AML) constitutes a hard boundary for the convergence of IHTE (see Ch. 6 for further discussion).

An other major aspect in this analysis is the DPT (see Fig. 3.3). While the procedure removes most of the 2π-periodic modulations, some distortions remain in the phase

---

[12] Siméon D. Poisson (1781-1840) [4]

[13] System Parameters of the SL oscillator Eq. (5.1) are $\mu = 6$, $\alpha = 0.1$, $\nu = 1$. Noise parameters are $\sigma = 0.1$ and $\tau_J \in [1/16, 1/8, 1/4, 1/2, 1, 2, 3]$.

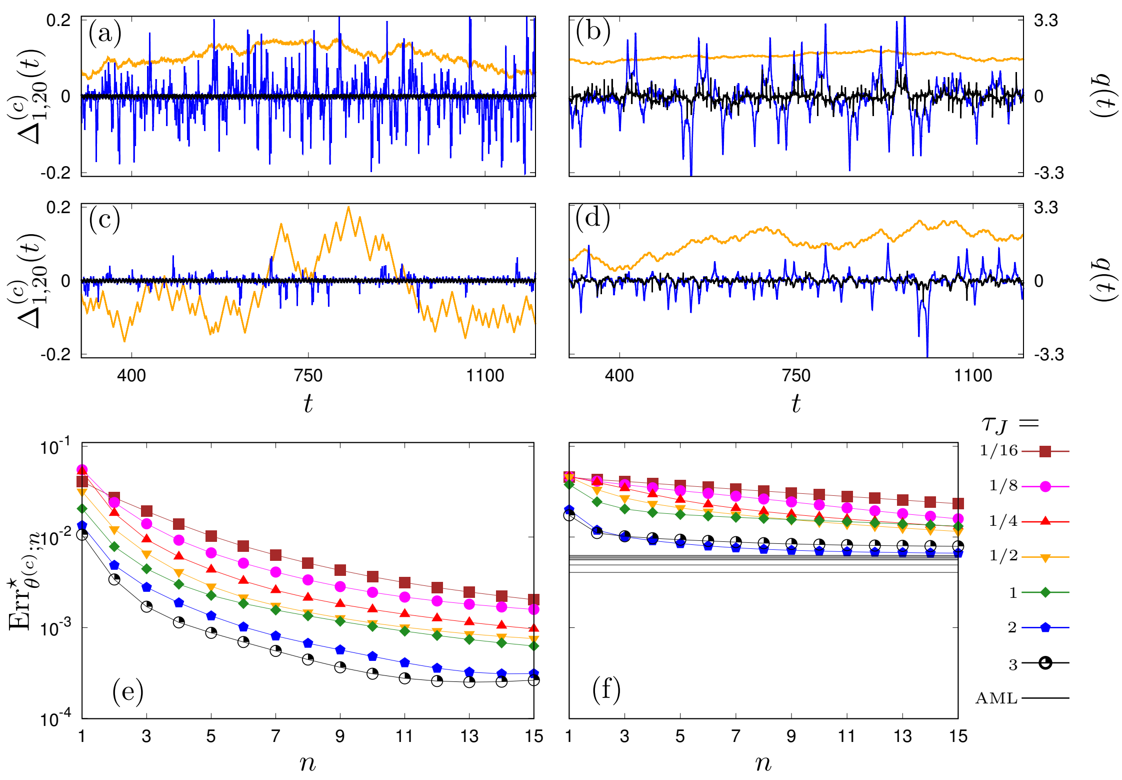

Figure 5.8: Depicted are phase residua for the signal $X_3(t)$ (a, c) and for $X_6(t)$ (b, d). Shown are results of the first iterative and after 20 iterations (blue/black) for $\tau_J = 1/16$ (a,b) and $\tau_J = 3$ (c, d). Shown in the background of the plots are modulations $q(t)$ (orange). (e, f): Periodicity errors for $X_{3,6}(t)$. Noteworthy are the black solid lines in (f) which indicate the level of amplitude modulation (AML) present in the signal $X_6(t)$. This level constitutes a lower bound of accuracy for phase demodulation (see Ch. 6).

approximation for the SL system. In contrast, 2π-periodic modulations are much more reduced for the purely phase-modulated signal $X_3(t)$. This underlines the significance of the demodulation conditions Eq. (3.18) for a successful reconstruction of the microscopic phase dynamics. If IHTE is unable to guarantee them, also the DPT necessarily fails. In particular, the missing 2π-periodicity of $\theta^{(d)}(t)$ turns out to be deprecated if the sampling interval dt is to large. In contrast, due to interpolation, the spline-based protophase $\theta^{(c)}(t)$ avoids such problems to a large extent.

Up to this point, measurement noise has been excluded from a discussion as this work seeks to examine the genuine properties of IHTE which would otherwise be masked by the problem of noise filtering. In fact, an additive random term introduces completely unrelated modulations to the underlying dynamics of the system. Thus, the basic assumptions of the phase modulation procedure are no longer fulfilled. Unfortunately, the Hilbert transform is highly sensitive to these small random fluctuations such that a reconstruction of the true phase is significantly corrupted. This problem is further examined in the forthcoming chapters.

Chapter 6

Limitations of phase reconstructions

Bibliographic information

A manuscript of the findings in this chapter is currently under preparation.

Erik Gengel and Arkady Pikovsky
Data driven phase reconstruction with iterated Hilbert transform embeddings
- benefits and limitations

Main findings:

- Parameter study of IHTE for generic phase-amplitude modulations
- Examination of limiting factors in phase reconstruction

6.1 The influence of amplitude modulations

For generic phase-amplitude modulated signals of non-linear oscillators, the amplitude modulation is usually significant. Then, strict 2π-periodicity of the generalised waveform $X(\varphi)$ (see Eq. (3.13)) is lost and IHTE are unable to provide a reliable demodulation. Indeed, in the presence of (weak) amplitude perturbations, a phase extraction according to the demodulation operator $\hat{P}[X]$ Eq. (4.9) mixes spectral content of the true phase modulation in $\varphi(t)$ and the genuine spectral content of amplitude variations. For the first protophase approximation it follows

$$\theta_1(t) = \hat{P}[X](\theta_0) \approx \hat{P}\Big[\hat{M}[\mathbf{y}^{(0)}]\Big](\theta_0) + \Delta_{\hat{P},1}(X, \delta\mathbf{y})(\theta_0)\ . \tag{6.1}$$

But, in subsequent iterative steps, additional distortions might remain small. However, since neither the plane IHTE demodulation nor the transformation of protophases $\theta(t)$ to phase approximations $\psi(t)$ is able to separate true amplitude modulations from artificial amplitude modulations, a combination of IHTE and DPT (see Sec. 3.5) can provide largely erroneous results. When occurs the transition from reliable estimation to erroneous results?

The deviation of a signal from pure phase modulation can be estimated by integration of the function

$$X(\varphi + 2\pi) - X(\varphi) \approx X'(\mathbf{y}^{(0)}(\varphi))[\delta\mathbf{y}(t(\varphi + 2\pi)) - \delta\mathbf{y}(t(\varphi))]\ .$$

The resulting measure

$$(\mathrm{AML}_X)^2 = \frac{\int_{\varphi(t_0)}^{\varphi(t_m)} [X(\varphi + 2\pi) - X(\varphi)]^2 d\varphi}{\int_{\varphi(t_0)}^{\varphi(t_m)} (X(\varphi) - \langle X\rangle_t)^2 d\varphi} \tag{6.2}$$

is denoted as *amplitude modulation level* (AML). If $X(\varphi)$ resembles a wide band such that a decomposition into $S(\varphi)$ and $\varphi(t)$ is not meaningful, AML_X is large. On the contrary, if a signal is purely phase modulated, AML_X vanishes.

Accordingly, a corrected periodicity error

$$\mathrm{Err}^{*}_{\mathbf{q};n} = \mathrm{Err}^{\star}_{\mathbf{q};n} \frac{\int_{\mathbf{q}(t_0)}^{\mathbf{q}(t_m)} X^2(\mathbf{q}) d\mathbf{q}}{\int_{\mathbf{q}(t_0)}^{\mathbf{q}(t_m)} (X(\mathbf{q}) - \langle X \rangle_t)^2} \tag{6.3}$$

for a protophase $\mathbf{q}(t)$ is employed in the following discussion. In fact, AML can be interpreted as the minimal periodicity error, i. e. it quantifies the periodicity in the situation that phase reconstruction yields $\varphi(t)$. The slight modification of normalisation from second moment to variance reduces the dependence on the mean value of a signal and thus allows to compare the absolute value of the difference Eq. (6.1) for signals with different averages.

6.1.1 Setting the scene - oscillators, forcing and observation

For the following discussion of problems, the SL dynamics and the VdP dynamics are considered.

Oscillator models

The considered SL dynamics

$$\dot{a} = \mu(1 - |a|^2)a + ia(\mu - |a|^2 - 1) + i\varepsilon p(t) \tag{6.4}$$

is a mixture of versions Eqs. (2.6) and (5.1) with constant limit-cycle amplitude of unity and a constant average frequency ω. Most importantly, in this scaling, the unperturbed phase dynamics depends only weakly on parameter μ through the explicit isochronic coupling $\varphi(t) = \theta(t) - \alpha\mu^{-1}\ln[r(t)]$ what allows the clearest separation of amplitude variations and phase modulations in the following analysis.

In the unperturbed VdP systems Eq. (2.29), μ determines the stability of the cycle and the type of oscillations. While for small $\mu \ll 1$ the system performs quasi-harmonic oscillations – similar to the SL system but with a weakly stable limit cycle, for $\mu \gg 1$ relaxation oscillations with two distinct time scales are present. To make the demodulation procedures for SL and VdP oscillator more comparable, the state variables $u(t)$ and $v(t)$ of the VdP system are rescaled so that their amplitude on the limit cycle varies only slowly according to μ. Moreover, the scaling ensures a relatively constant frequency of the system (see Fig. 6.1):

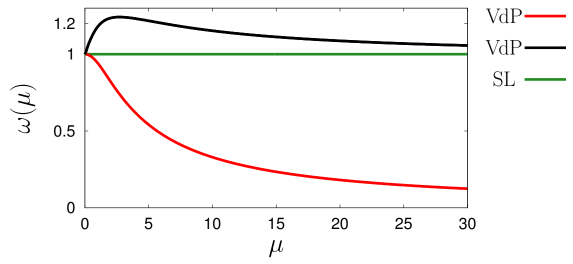

Figure 6.1: Shown are frequencies $\omega(\mu)$. For the SL system Eq. (2.12) the frequency is a constant (green). In contrast, for the first VdP oscillator Eq. (2.29) ($\omega_1 = 1$) $\omega(\mu)$ shows a strong non-linear dependence (red). In the scaled VdP dynamics Eq. (6.5), the variations of the frequency is much smaller (black).

$$\dot{u} = -\Big(1 + \frac{\mu}{4}\Big)^2 v \qquad \dot{v} = u + \mu\Big(1 + \frac{\mu}{4}\Big)\Big(1 - 4u^2\Big) + \varepsilon p(t)\ . \tag{6.5}$$

Forcing

The forcing in both system is given by

$$p(t) = \left[\cos(\omega s t) + \cos\left(\sqrt{3/5}\omega s t + \pi/4\right) + \cos\left(\sqrt{2/5}\omega s t + \pi/2\right)\right]/3\ . \tag{6.6}$$

In contrast to Sec. 5.1 where a purely harmonic force is in use, here three incommensurate frequencies are considered. Again, the parameter s allows to tune the frequencies with respect to the systems frequency $\omega(\mu)$. The main purpose of this choice is that forcing and system dynamics stay asynchronous. A practical motivation follows from neuroprosthetic research areas [184] where the complex shape of external (theta-burst) stimuli is adapted to intervene in a pathological state of the brain or even correct the network pathology with external devices.

Observable

As a final example, in this chapter the generic observable

$$X_7(t) = u^3(t) + v(t) + 2u(t)v(t) \tag{6.7}$$

is considered where $u(t), v(t)$ are the state-space variables of the SL or VdP oscillator in Eqs. (2.12) and (6.5). This observable is a smooth and moderately complex function of the state space variables. For quasi-harmonic oscillations it has two maxima and minima on the basic period of oscillations while it is quite wild for relaxation oscillations (see Fig. 6.2 (c)). In fact $X_7(t)$ combines several unfortunate properties for inference: On the one hand it contains epoch of large spikes which demand for a high rate of sampling. On the other hand, in between spikes the signal changes monotonously or is comparably flat and thus relatively insensitive to changes in the underlying state-space dynamics.

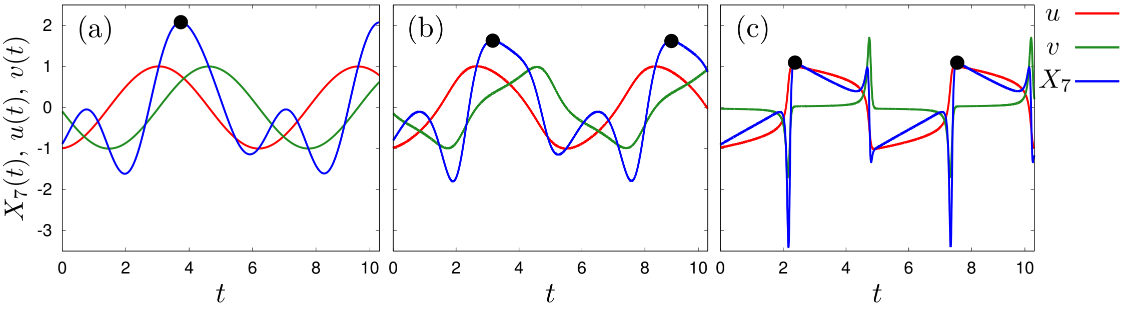

Figure 6.2: (a): Observables of the SL oscillator with $\alpha = 0.1$ for $\mu = 0.5$ and $\omega s = 0.5$. (b, c): Observables of the VdP oscillator for $\omega s = 0.5$ and $\mu \in [0.5, 5]$ respectively. The bold black dots indicate marker events that correspond to a Poincaré crossing in the embedding space.

Amplitude modulation levels

Figure 6.3 presents the AML for the SL and VdP system[1].

It can be seen that for the SL oscillator curves of AML normalised for different ε nearly perfectly overlap in Fig. 6.3 (a). This indicates that AML_{X_7} decreases $\sim \varepsilon$.

---

[1] System parameters are $\alpha = 0.1$, $\omega = 1.0$ for the SL oscillator. Forcing parameters are $\omega s \in [0.5, 1, 5]$ and $\varepsilon \in [0.01, 0.02, 0.05, 0.1]$.

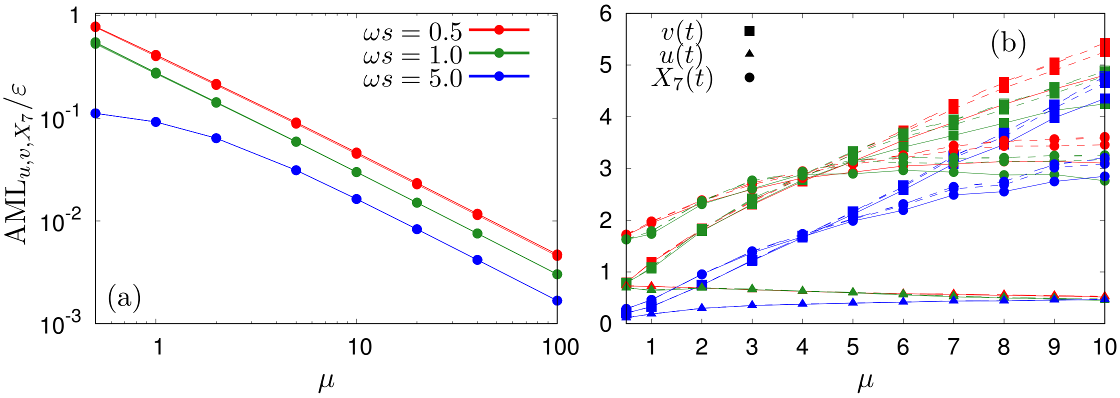

Figure 6.3: Shown are levels of amplitude modulation in (a) for the driven SL oscillator Eqs. (2.6) and (6.6) observed by $X_7(t)$ Eq. (6.7). Curves show AML_{X_7} Eq. (6.1) normalized by the amplitude of the forcing $\varepsilon \in [0.01, 0.02, 0.05, 0.1]$ and values of forcing frequency as in the panel. (b): Depicted is AML_{u,v,X_7} for the VdP equation (6.5) for frequencies like in panel (a) and similar forcing amplitudes (dashed lines).

Moreover, the level of AML decreases with parameter μ as $\sim \mu^{-1}$. Thus, in the limit $\mu \to \infty$, the observable $X_7(t)$ is purely phase modulated.

In contrast, for the VdP dynamics there is no any significant decrease of the level of the amplitude modulation visible in Fig. 6.2 (b). Additionally, the amplitude modulation level slightly spreads out for different ε indicating a complex dependence on Ω, μ and ε. Thus, it is rather problematic if here any technique based on the phase demodulation works.

6.2 Phase demodulation for oscillators – method dependent effects

6.2.1 Periodicity error

To remove as much amplitude effect as possible, a direct amplitude demodulation of $X_7(t)$ can be achieved by normalisation with $r(t) = \sqrt{u^2(t) + v^2(t)}$. The corresponding signal is denoted by $\bar{X}_7(t)$. In particular, for the SL oscillator this procedure yields $\bar{u}(t) = \cos(\phi(\varphi, r))$ and $\bar{v}(t) = \sin(\phi(\varphi, r))$ which still weakly depend on $r(t)$ through the model-dependent isochronic coupling. Thus, any distortions in the phase approximation will be of second order in ε (see Sec. 7.2.2 for a further discussion).

Figure 6.4 indicates that direct amplitude modulations present in $X_7(t)$ account for at least one order of magnitude in the periodicity errors. In contrast, direct normalisation to obtain $\bar{X}_7(t)$ indeed allows for a successful phase reconstruction by means of IHTE, essentially independent of the stability level.

This observation is supported by a comparison of different phase modulations in Fig. 6.5: For $\bar{X}_7(t)$, phase estimates indicate significant – although not perfect – improvements due to the usage of IHTE in combination with DPT. In contrast for the original data $X_7(t)$, iterations provide only minor improvements. In fact, results in Figs. 6.4 and 6.5 are an indication that (I)HTE are already vulnerable to small amplitude variation in the raw data.

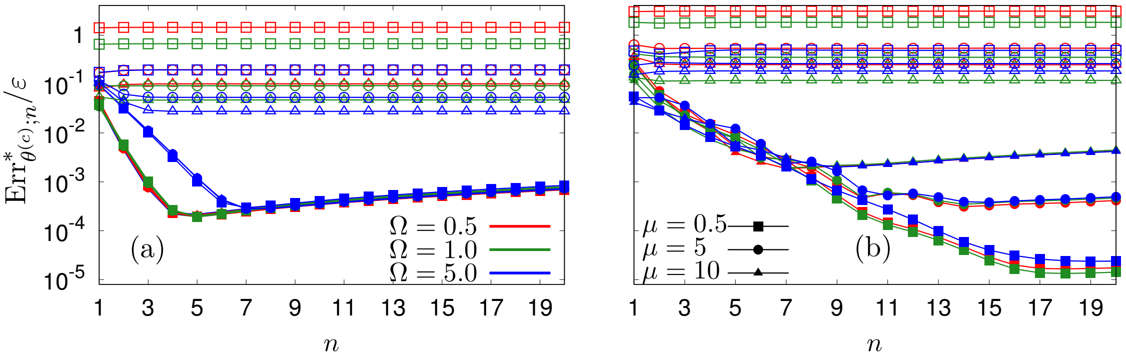

Figure 6.4: Depicted are modified periodicity errors Eq. (6.3) of $X_7(t)$ for the SL (a) and VdP (b) dynamics. Shown are results for different stability regimes: $\mu \in [1, 5, 10]$ (squares,triangles and circles) and forcing frequencies $\Omega \in [0.5, 1, 5]$ (red, green, blue). Results for $X_7(t)$ are shown with empty markers and results for $\bar{X}_7(t)$ are shown with full markers. While demodulation of $\bar{X}(t)$ is successful, the results based on $X(t)$ indicate that no improvement of phase reconstruction was achieved.

Interestingly, while for the SL oscillator, the normalisation yields similar convergences for all stability levels, a spread of curves is observed for the VdP system. This spread is caused by two main effects. First, the waveform changes according to μ. As a consequence, small numerical errors in $\mathrm{Err}^*_{\theta^{(c)};n}/\varepsilon$ become visible for the challenging waveform at $\mu = 10$. Second, it can be expected, that the spread is also a product of the still present isochronic coupling in $\varphi(t)$: While for the SL system, isochronic coupling of phases and amplitudes is functionally similar for all stability level $\sim \mu^{-1}$, the isochronic coupling in case of the VdP equation depends non-linearly on μ. Accordingly, the smallest residual errors occur for small μ where the VdP dynamics is quasi-harmonic with a comparably weak isochronic coupling. Then, for increasing μ, the isochonic density becomes more non-uniform on the limit cycle what causes the periodicity error to saturate at higher values.

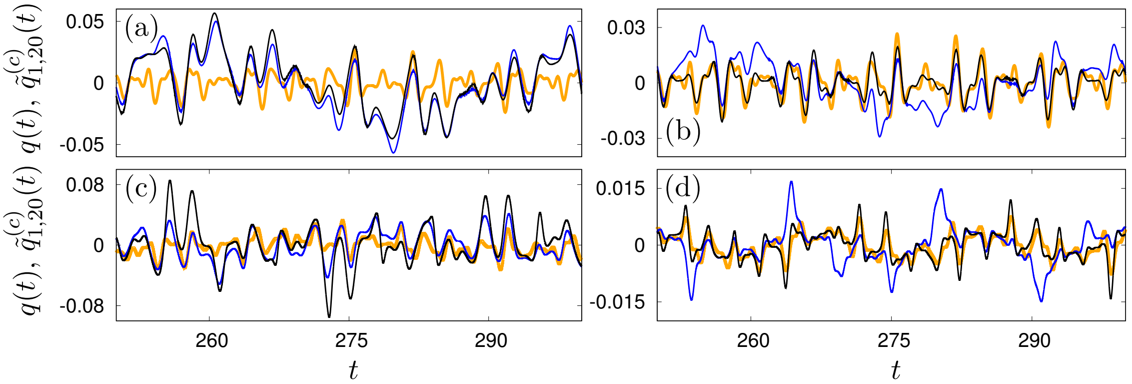

Figure 6.5: Shown are snapshots of phase modulations for the SL (a, b) and VdP system (c, d). A comparison of true modulation $q(t) = \varphi(t) - \omega t$ (orange) and reconstructions $\tilde{q}^{(c)}(t) = \psi^{(c)}(t) - \tilde{\omega} t$ in the first step (blue) and after iteration (black) indicates the success of Hilbert iterations for $\bar{X}_7(t)$ (b, d). In contrast no essential improvement is visible for the phase-amplitude modulated signal $X_7(t)$ in (a, c). System parameters are $\mu = 0.5$, $\omega s = 5$, $\varepsilon = 0.1$, $\alpha = 0.1$.

6.2.2 Phase similarity error

The periodicity error Eq. (6.3) delivers a measure of demodulation accuracy, if the actual phase $\varphi(t)$ is unknown and is thus applicable in experiments. Complementary is the phase similarity error STD^{ψ}_{n} Eq. (5.3) which monitors the actual discrepancy between $\varphi(t)$ and the phase approximation $\psi_n(t)$. In presence of amplitude modulations both measures are not strictly related to each other. Is it anyhow sufficient to estimate the periodicity error $\mathrm{Err}^*_{\mathbf{q};n}$ to find the optimal phase approximation?

As an example, here demodulation of the state space coordinate $u(t)$ is considered for the SL and VdP system in dependence of stability μ and frequency ratio s. After finding a decomposition $u(t) = \tilde{S}(\theta(t))$, the DPT is applied to the VdP signal. Shown in Fig. 6.6 is the minimal value of $\mathrm{STD}^{\psi^{(c)};\star}$, not to be mistaken with the reconstruction error at the optimal value of periodicity $\mathrm{Err}^*_{\theta^{(c)}}$.

Clearly, demodulation can be achieved for the SL oscillator with rather high precision and for most of the considered parameters. Noteworthy, in some cases the difference $\psi(t) - \varphi(t)$ is of the same order as the amplitude of the true modulation. This underlines that commonly used phase approximations $\psi_1(t)$ based on the first Hilbert transform are not suitable for further analysis. Then, performing iterations, even in the worst case of small μ, some improvements are achieved. Contrasting are the demodulation results for the VdP oscillator where iterations provide only smaller improvements.

At which step the optimal demodulation is achieved might not be detectable based on $\mathrm{Err}^*_{\mathbf{q};n}$. Instead, the minimal value $\mathrm{Err}^*_{\mathbf{q}}$ arises at a step n^* and corresponds to $\mathrm{STD}^{\psi,*}$ while the true minimum of the phase error, $\mathrm{STD}^{\psi,\star}$ occurs at a step $n^\star$. Indeed, Fig. 6.7 indicates that the relative difference of both errors is small compared to the strength of forcing – particularly for the SL system, where an iterative demodulation achieves most of its accuracy in the first steps followed by a saturation in accuracy. Thus the discrepancy between theoretic-optimal step $n^\star$ and detectable optimum step n^* is rather large while the relative difference of accuracies is small. This statement holds for most

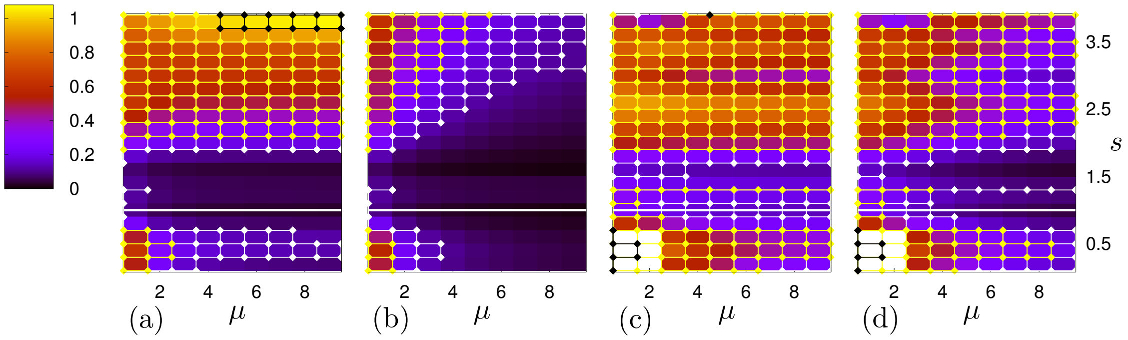

(a) (b) (c) (d)

Figure 6.6: Shown are optimal phase similarity errors $\mathrm{STD}^{\psi;\star}$ obtained from demodulation of $u(t)$. The bold horizontal line indicates $s = 1$. White diamonds indicate for $0.5 > \mathrm{STD}^{\psi;\star} > 0.1$ yellow diamonds indicate for $1 > \mathrm{STD}^{\psi;\star} > 0.2$ and black diamonds indicate for $\mathrm{STD}^{\psi;\star} > 1$. Shown in (a,b) are results for the SL system. Shown in (c,d) are results for the VdP oscillator. Generally, it can be seen that IHTE allows for major improvements of wideband demodulation ($s > 1$). Also minor improvements are visible in the slow frequency band ($s < 1$). In accordance with Fig.6.3, the reconstruction of the SL phase is achieved for a wide range of stability and frequency pairs. In contrast, for the VdP system the improvements are relatively small and occur mostly for high stability and high frequencies.

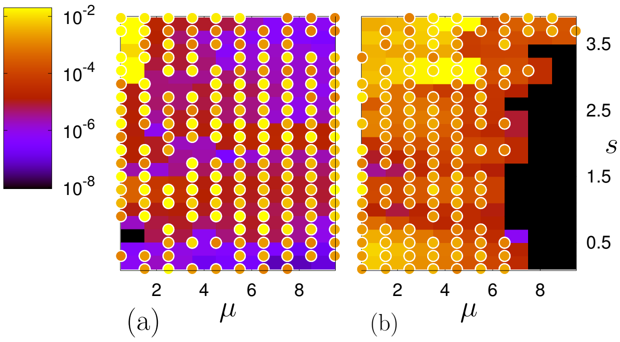

(a) (b)

Figure 6.7: Shown in colour scale are the differences $\left|\mathrm{STD}^{\psi^{(c)},\star} - \mathrm{STD}^{\psi^{(c)},*}\right|$ corresponding to Fig. 6.6. Coloured dots indicate cases where optimal periodicity and optimal phase occure at different steps. Point colour indicates the difference $|n^\star - n^*|$ of the respecitve iterative steps rescaled to the interval of the error difference. (a): SL, (b): VdP

of the parameters shown. Slightly different are observations for the VdP system which indicate that a stronger correlation of optimal steps is present while at the same time discrepancies $n^\star - n^*$ account also for larger error differences, two orders of magnitude larger than for the SL system! This discrepancy however, might be considered as a minor problem since the phase reconstruction suffers from a to large AML.

6.3 The problem of protophase-to-phase tranformation

Information about the actual phase dynamics is usually found in the tiny remaining variations after performing the DPT Eq. (3.23). Thus, a protophase-to-phase transformation demands for accurate estimates of the Fourier modes Eq. (3.25) and for this a protophase needs to be 2π-periodic and the time series has to be sufficiently long. Then, the mapping $\Theta(\varphi)$ is estimated based on data.

Complementary to the DPT a protophase-to-phase mapping can be constructed by a direct Fourier fit on the data $\varphi(\theta) - \theta = \Delta(\theta)$:

$$\left\langle (\Delta(\theta) - (\psi_{\mathrm{FPT}}(\theta) - \theta))^2 \right\rangle_\theta \to \min .$$

The obtained mapping $\psi_{\mathrm{FPT}}(\theta)$ is termed *fit-based protophase-to-phase transformation* (FPT) and the resulting phase approximation is $\psi_{\mathrm{FPT}}(t)$. Such an approach avoids the uniform-density assumption needed for DPT and thus is able to capture variations in a (non-uniform) phase density $\rho(\varphi)$.

Indeed, while the protophase-to-phase mappings based on DPT and FPT indicate for an essential reconstruction, erroneous modulations remain in the phase approximations $\psi^{(c)}_{\mathrm{DPT};1,20}(t)$. This can be observed in the scatter plots $\dot{\Delta}^{(c)}_{\mathrm{DPT}}(\dot{\varphi})$ in columns 2 and 3 of Fig. 6.8. In fact, for none of the considered cases a significant improvement of the phase approximation is achieved by IHTE although the AML_{X_7} in Fig. 6.3 indicates that $X_7(t)$ is approximately phase modulated. In contrast, the FPT results in column 4 of Fig. 6.8 show a smaller deviation for a small AML (large μ).

Complementary are the fitting results shown in Fig. 6.9 for the VdP system. As $X_7(t)$ is quite spiky, $\Delta^{(c)}(\theta^{(c)})$ in columns 2 and 3 shows large jumps in its derivative. Thus a quite large number of fitting modes F_k and long observations are needed to obtain accurate estimations. Here a zoom to one of the local minima of $\Delta^{(c)}(\theta^{(c)}) = \varphi(\theta^{(c)}) - \theta^{(c)}$ shows that, DPT and FPT are able to recover the shape of the band with only very small variations left. Moreover, it can be seen by comparison of columns 2 and 3 that the gradients in $\Delta^{(c)}(\theta^{(c)})$ increase due to iteration. Thus, IHTE – in this example – results in even more demanding data.

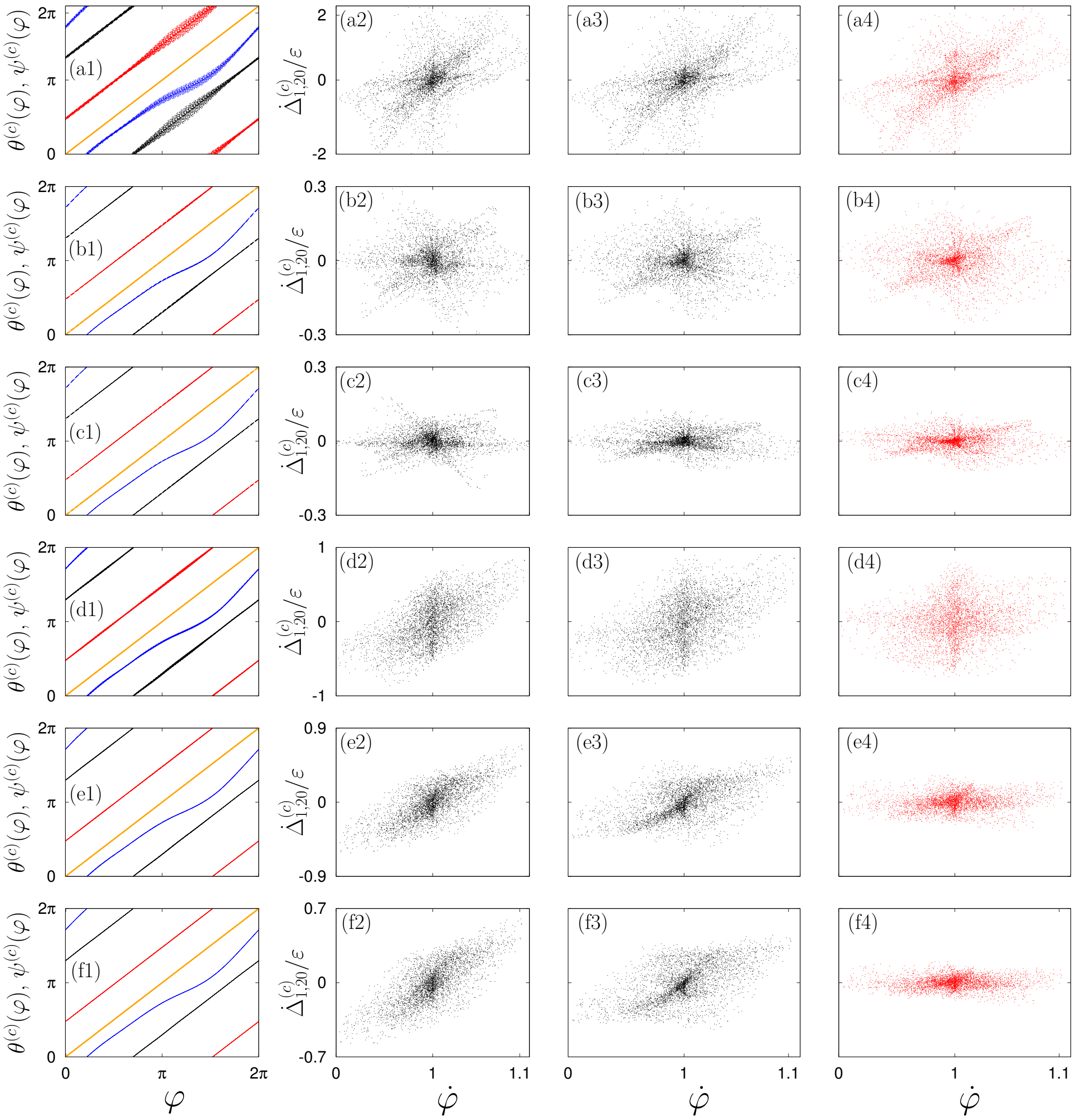

Figure 6.8: Shown are results for the SL oscillator. Column 1: Mappings $\theta^{(c)}(\varphi)$ (blue), $\psi^{(c)}_{\mathrm{DPT}}(\varphi)$ (black) and $\psi^{(c)}_{\mathrm{FPT}}(\varphi)$ (red). Other panels show scatter plots of derivative deviation $\dot{\Delta}^{(c)}_{1,20}(t)$ against the true derivative of $\varphi(t)$. Columns 2,3: Results based on $\theta_{1,20}(t)$ for the DPT. Column 4: Results for $\theta^{(c)}_{20}(t)$ and FPT. Parameters are (a): $\mu = 0.5$, $s\omega = 0.5$, (b): $\mu = 5$, $s\omega = 0.5$, (c): $\mu = 10$, $s\omega = 0.5$, (d): $\mu = 0.5$, $s\omega = 5$, (e): $\mu = 5$, $s\omega = 5$, (f): $\mu = 10$, $s\omega = 5$. Fixed parameters are $\varepsilon = 0.1$,, $\omega = 1$, $\alpha = 0.1$. The FPT and DPT are performed with 40 and 20 Fourier modes repectively.

In conclusion, for dynamical systems, imprecise protophases and the uniform-density assumption Eq. (3.19) result in unavoidable errors in the phase reconstruction. While these errors are not present if a purely phase modulated signal is analysed by means of IHTE, they seem to be amplified if periodicity is blurred. Partly, the demands for an accurate estimation of the protophase-to-phase mapping might be met by an increase of the observation time[2]. However this results in long computation times needed for IHTE.

---

[2] The fitting results in Fig. 6.9 are obtained on data sets containing $3 \cdot 10^5$ point. In total $700, 600, 500, 400, 375, 350, 325, 275, 250, 225, 200, 175, 150, 100, 50$ and 25 modes are used to perform a

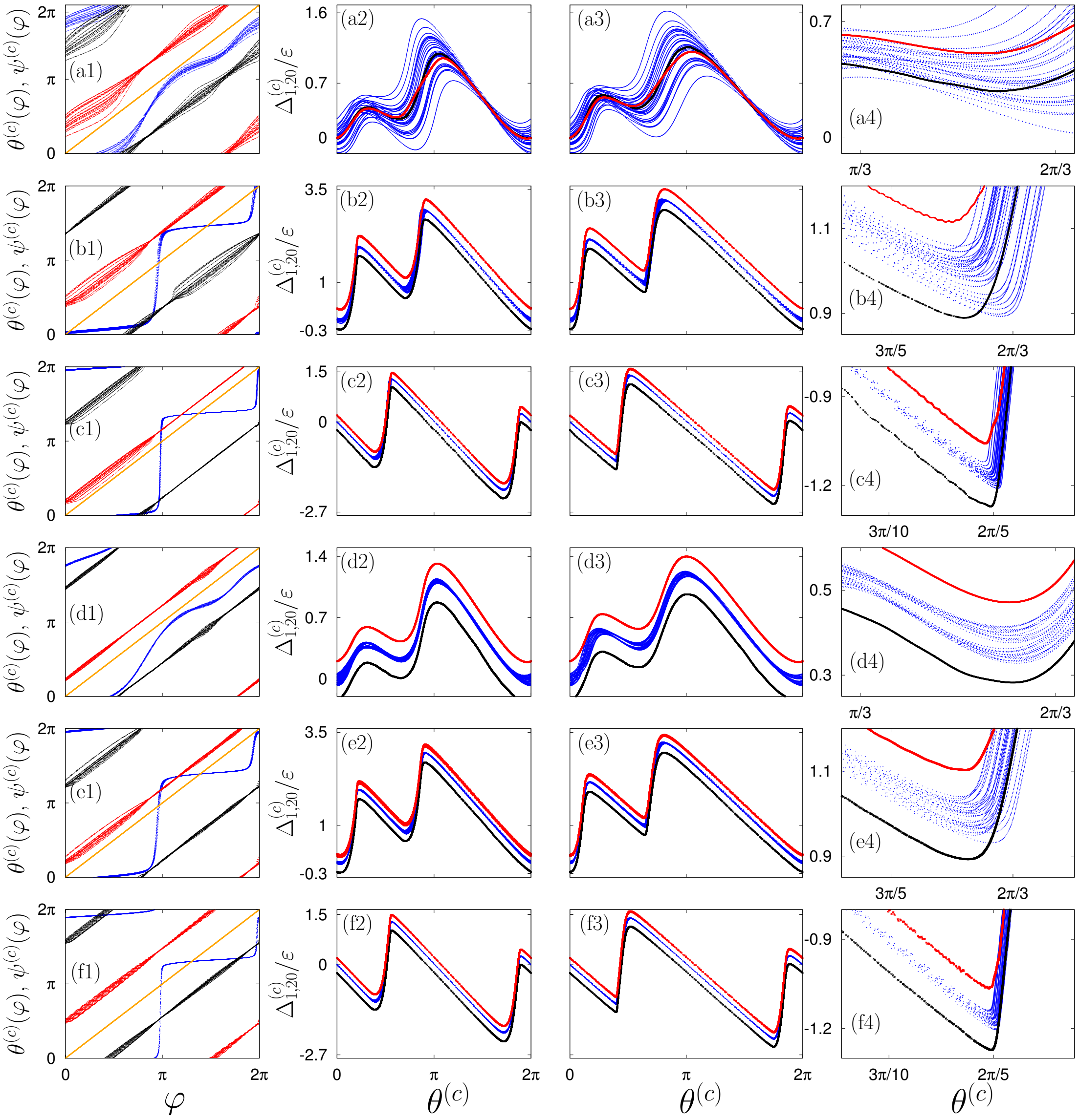

Figure 6.9: Results for the VdP oscillator. Column 1: Mappings $\theta^{(c)}(\varphi)$ (blue), $\psi^{(c)}_{\mathrm{DPT}}(\varphi)$ (black) and $\psi^{(c)}_{\mathrm{FPT}}(\varphi)$ (red). Other panels show $\Delta^{(c)}_{1,15}(\theta^{(c)})$ and fit from DPT (black) and FPT (red). Columns 2,3: Results based on $\theta_{1,15}(t)$. Column 4: Results for $\theta^{(c)}_{15}(t)$. Shown here is a zoom into one of the two local minima. Parameters are (a): $\mu = 0.5$, $s\omega = 0.5$, (b): $\mu = 5$, $s\omega = 0.5$, (c): $\mu = 10$, $s\omega = 0.5$, (d): $\mu = 0.5$, $s\omega = 5$, (e): $\mu = 5$, $s\omega = 5$, (f): $\mu = 10$, $s\omega = 5$. The forcing amplitude is $\varepsilon = 0.1$. Noteworthy, for these highly challenging fits, the DPT and FPT transform are realised with different modes. Or the fitting is not succesfull at all.

Currently, it is an open problem how to incorporate non-uniformity into the DPT. As is indicated by FPT, doing so would potentially allow to further decrease the phase reconstruction error. On the other hand, the DPT reliably estimates the uniform density even for highly challenging phase data presented in Fig. 6.9. Thus, it still constitutes the best – and only – choice to retrieve a phase approximation.

DPT and FPT. The optimal result of this scan is depicted in the panels

Chapter 7

Future topics

7.1 Phase dynamics reconstruction for biological oscillator networks

Typically, signals of biological oscillators contain significant amplitude modulations (e. g. see Fig. 3.1). However, it might be possible to observe biological oscillations with quite stable amplitudes. In experiments this could be achieved in controlled settings and if probands are at rest. Here, a system of three non-identical ML oscillators Eq. (1.1) serves as an example:

$$\begin{aligned} C\dot{V}_1 &= I_0 - g_L(V_1 - E_L) - g_K w(V_1 - E_K) - g_{Ca} M_\infty(V_1)(V_1 - E_{Ca}) + I_{\text{syn}}(V_1, V_2) \\ \dot{w}_1 &= \lambda_{w,1}(V_1)(W_\infty(V_1) - w_1) \\ C\dot{V}_2 &= I_0 - g_L(V_2 - E_L) - g_K w(V_2 - E_K) - g_{Ca} M_\infty(V_2)(V_1 - E_{Ca}) \\ &\quad + I_{\text{syn}}(V_2, V_1) + I_{\text{syn}}(V_2, V_3) \\ \dot{w}_2 &= \lambda_{w,2}(V_2)(W_\infty(V_2) - w_2) \\ C\dot{V}_3 &= I_0 - g_L(V_3 - E_L) - g_K w(V_3 - E_K) - g_{Ca} M_\infty(V_3)(V_3 - E_{Ca}) + I_{\text{syn}}(V_3, V_2) \\ \dot{w}_3 &= \lambda_{w,3}(V_3)(W_\infty(V_3) - w_3)\ . \end{aligned} \tag{7.1}$$

The single units are coupled by synaptic currents

$$I_{\text{syn}}(V_k, V_j) = \frac{\varepsilon(V_{\text{rev}} - V_k)}{1 + \exp(-(V_j - V_{\text{th}})/\sigma_s)}\ . \tag{7.2}$$

The parameters[1] of the model can be found in Tab. A.1. The neurons differ in their time constant $1/\tau_{g;1,2,3} \in [1/\tau_g, 0.4/\tau_g, 0.8/\tau_g]$ of gating which is incorporated in $\lambda_{w,k}(V_k)$. The system parameters are chosen in accordance to maintain an asynchronous network state. The coupling topology is similar to the oscillator triplet analysed in Ch. 2. The original state-space dynamics is depicted in Fig. 7.2. Indeed, each oscillator possesses a quite stable spike amplitude but significant perturbations are present in the lower left part of the limit cycles.

The phase dynamics of the units is reconstructed by means of the previously employed IHTE-DPT procedure[2]. Observed is the membrane potential $V_k(t)$. Figure 7.1 shows snapshots of the frequency reconstructions together with the true frequencies $\dot{\varphi}_{1,2,3}(t)$, obtained directly from the state space dynamics.

Interestingly, iterations restore the timing of the main frequency pulses to a high precision. This indicates that IHTE indeed, restore phase modulations which occur horizontally in the signal. The remaining deviation can be attributed to the still present vertical amplitude variation in the signal and to the isochronic coupling which is not considered in the present procedure.

---

[1] Additional parameter of coupling are $\varepsilon = 0.2$ mA/mV, $V_{\text{rev}} = 20$ mV, $V_{\text{th}} = 25$ mV and $\sigma_s = 1$ mV.

[2] The reconstruction is based on 20 steps of the IHTE. The DPT is performed based on 150 Fourier modes. 1000 periods of the slowest oscillator are observed with $dt = 0.2$. Frequencies are reconstructed by means of a $\text{SG}_{12,25,4}$ filter

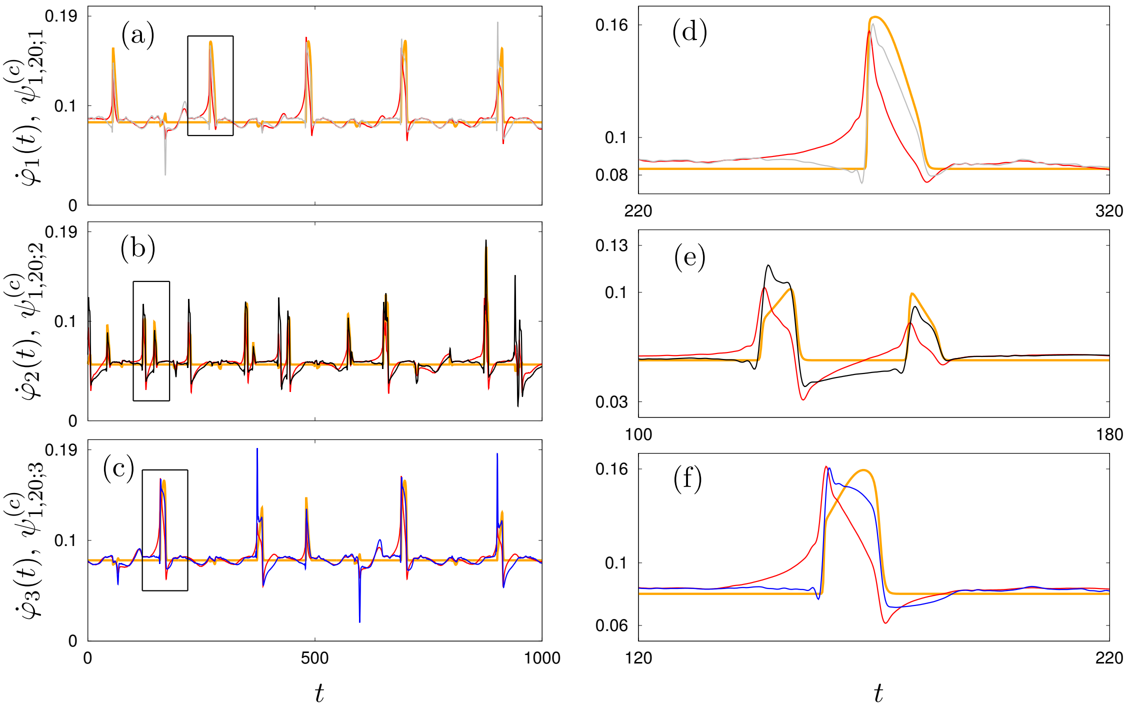

Figure 7.1: Shown in panels (a-c) are the frequency recontructions $\dot{\psi}^{(c)}_{1,2,3}(t)$ for the true frequency $\dot{\varphi}_{1,2,3}(t)$ (orange). Frequencies of the first iterate are shown in red. Frequencies of step 20 are shown in grey, black and blue respectively. The true frequency is obtained directly from the state space dynamics (see Sec. 2.4.1).

Data-driven network inference based on IHTE?

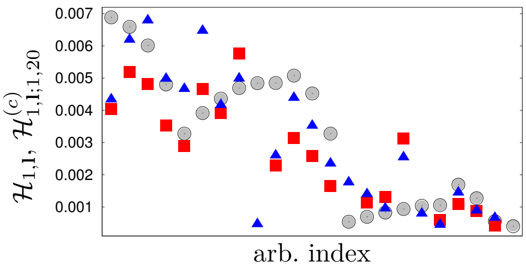

Shown are phase-coupling constants $\mathcal{H}_{1;\mathbf{l}} > 0.0002$ (see Ch. 2) for the first neuron obtained from direct fitting over 1000 (grey) and 2000 periods (black). Coupling constant based on $\psi^{(c)}_{1,20}(t)$ and 1000 periods are shown in red and blue respectively. Modes up to $|l_k| \leq 4$ are considered.

Coupling modes for all oscillators are listed in Tab. A.8. Due to its pulsatile nature, many of the modes account for pairwise coupling. Below, general observations are listed:

- Most of the actual coupling modes are detected also in the IHTE-based reconstruction.
- The strength of the coupling modes is poorly recovered. However, a closer inspection shows that result based on $\psi^{(c)}_{20}(t)$ indeed show some improvement compared to the commonly used Hilbert phase $\psi^{(c)}_1(t)$.
- Some modes have not been resolved at all in the data driven reconstruction while other modes are erroneously detected.

7.2 What does it mean to include amplitudes?

More precise phase reconstruction techniques have to include some coupling of phases and amplitudes. While in theoretic descriptions such a task yields long and involved equations (see Ch. 2), a data driven reconstruction of phase-amplitude coupling is even more challenging. The main reason for this is that phase-reconstruction methods usually have only limited control over the incorporation of amplitude modulations into the phase modulation. On the one hand this is due to the still existent discrepancy in purpose and mathematical definition of the methods and on the other hand, due to inherent method dependent shortcomings in general.

7.2.1 The separation problem

Given a signal $X(t) = \hat{M}[\mathbf{y}(t)]$ it is argued in Sec. 3.3 that for weakly perturbed limit cycles a waveform $S(\varphi) = \hat{M}[\mathbf{y}^{(0)}(\varphi)]$ and a (small) perturbation $\delta S(\varphi, \delta\mathbf{y}) = \hat{M}'[\mathbf{y}^{(0)}](\varphi)\delta\mathbf{y}$ can be defined. On the one hand this separation is motivated by theoretic conceptions that result in a mutual phase demodulation by means of IHTE. On the other hand, this separation leads to highly erroneous reconstructions of $\varphi(t)$:

If just $X(t) = S(\varphi(t))$ is considered, where $\varphi(t)$ is modulated, it means that $\dot{\varphi}(t)$ Eq. (2.2) necessarily incorporates information about the amplitude perturbation $\delta\mathbf{y}(t)$ of the system through the isochronic coupling. Thus, $\varphi(t) = \varphi(t, \delta\mathbf{y})$. However, at the same time, the true amplitude perturbation is observed explicitly in the embedding through $\delta S(\varphi, \delta\mathbf{y})$. But this means that $S(\varphi)$ and $\delta S(\varphi, \delta\mathbf{y})$ are (partly) redundant. The consequence is that a constructive definition of the waveform $S(\varphi)$ – and thus amplitude, measured relative to an imaginary unperturbed embedding, is problematic.

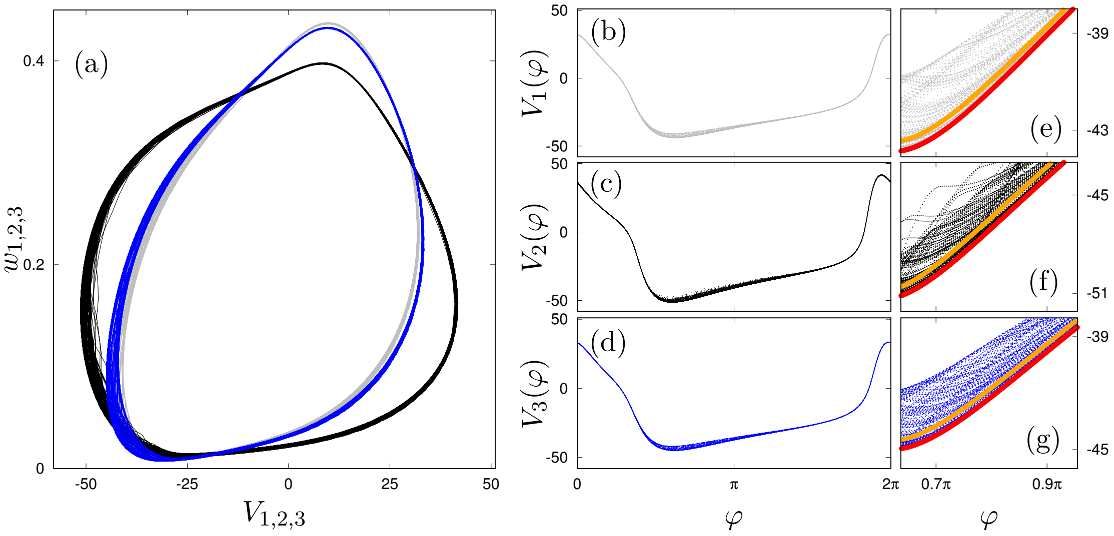

Figure 7.2: Depicted in (a) are the perturbed state trajectories of the ML network Eq. (7.1). The wide band of the trajectory in the left part of the cycle indicates that phase-amplitude coupling is significant. Panels in (b-d) depict the generalies waveforms $V_{1,2,3}(\varphi)$ (grey,back,blue). Shown in (e-g) is an enlarged view of the wavform. Additional curves show the time average $\langle X(\varphi(t))\rangle$ as an example for an erroneous recontruction of the refenrce waveform (orange) and the true waveforms of the unperturbed system (red).

$S(\varphi)$ seems to arise in the limit of weak perturbations such that *the* waveform is defined by a measurement $\hat{M}[\mathbf{y}^{(0)}(\varphi)]$ of the limit cycle solution and, implicitly, by the isochronic coupling $\Phi'[\mathbf{y}^{(0)}]$ (e. g. see Eq. (1.6)). But the assumption that the functional dependence of $S(\varphi)$ on φ is time invariant collides with existence of amplitude variation in $X(t)$ as there exists $X(\varphi)$ but not $S(\varphi)$. Thus, if one would try to retrieve $S(\varphi)$ – for example – from local time averaging of the generalised waveform $X(\varphi)$ at phase φ, it is usually not guaranteed that $\langle \delta S(\varphi, \delta\mathbf{y}(t))\rangle_t$ vanishes for all φ (see Fig. 7.2). Consequently, $S(\varphi)$ and thus, the reference embedding, would incorporate amplitude information although it is assumed that any state in an unperturbed system should depend solely on $\varphi(t)$.

Practically, since the modulations of $\varphi(t)$ and $\delta S(\varphi, \delta\mathbf{y})$ occur simultaneously, it is impossible to decide to which extent the band-like structure of a generalised waveform $X(\varphi)$ is caused by a phase modulation or by an amplitude deviation. In performing a phase demodulation, one simply assumes validity of the approximation $X(t) = S(\varphi(t))$ even though the validity of this approximation is limited. Indeed, this approximation might be possible if $\delta S(\varphi, \delta\mathbf{y})$ is small. However, it depends crucially on the method of phase demodulation and its robustness against variations of amplitude, what *small* really means!

7.2.2 The problem of essential mixing

The separation problem might be (partly) tackled through the introduction of an isochronic mapping in the embedding space but for this, a phase and an amplitude need to be reliably defined. Namely, there must not exist any spurious modulations in a protophase $\theta(t)$ and a proto-waveform $X(\theta)$. Indeed, for any complex number $X(t) + iY(t)$, its modulus might serve as an amplitude. As is illustrated in Fig. 1.9, the Hilbert transform provides the most stable geometric definition of amplitude through the modulus $A_z(t) = |z|(t)$ of the analytic signal.

But there is no guarantee that this amplitude is connected in an obvious way to the observed true perturbation $\hat{M}'[\mathbf{y}^{(0)}(t)]\delta\mathbf{y}(t)$ or directly to $\delta\mathbf{y}(t)$. This simply is a matter of fact. First, the observation can project the true state dynamics in such a way that the embedding comprises loops. While this might not be a problem for the determination of a protophase (see Sec. 4.1.2), $A_z(t)$ has limited meaning. Second there exists no general rule to construct the quadrature of a signal $X^{(q)}(t)$! Indeed, the Hilbert transform might be the most generic approximation of such a quadrature but it is still not exact in all cases. This is illustrated in Fig. 7.3 which shows demodulation results for the seemingly simple signal $X_{\mathrm{mono}}(t) = A(t)\cos(\phi(t))$.

- Panel (a) illustrates the method-related error of the reconstructed phase $\psi^{(a)}(t)$ based on IHTE and if $X_{\mathrm{mono}}(t)$ is purely amplitude modulated with $A(t) = (1 + 0.1\cos(\sqrt{5}t))$ (this modulation is fast and thus can not be demodulated from the slow carrier $\cos(t)$). The actual phase in this example is $\phi(t) = t$ while the reconstructed phase is $\psi_n^{(d)}(t) = t + \Delta_n^{(a)}(t)$. Thus, the actual amplitude modulations results in an artificial phase modulation. Notably, these artificial modulations increase in the course of iteration, what indicates that the IHTE are not suitable to demodulate this kind of signals properly.

- Panel (b) shows the opposite case of pure phase modulation where the phase is $\phi(t) = t + 1.2(\sin(0.25\sqrt{2}t) + \cos(0.25\sqrt{3}t)$ and $A(t) = 1$. It can be seen that here,

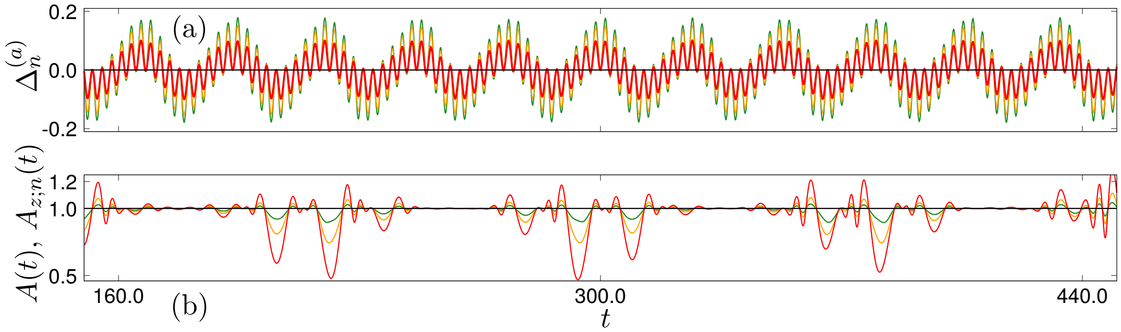

Figure 7.3: (a): Deviations $\Delta_n^{(d)}$, obtained from IHTE of $X_{\mathrm{mono}}(t) = (1 + 0.1\cos(\sqrt{5}t))\cos(t)$. This signal is purely amplitude modulated. (b): Shown are the actual amplitude $A(t) = 1$ in black and the amplitude $A_{z;n}(t)$ obtained via IHTE of $X_{\mathrm{mono}}(t) = \cos(t + 1.2(\sin(0.25\sqrt{2}t) + \cos(0.25\sqrt{3}t))$. This signal is purely phase modulated. Both panels show iterative steps $n = 1$ (red), $n = 2$ (orange) and $n = 3$ (green).

> the first Hilbert transform is not a good approximation of the quadrature as the reconstructed amplitude $A_{z;1}(t)$ deviates from the true amplitude $A(t)$. However, the iterative procedure proposed in Ch. 4 delivers a quadrature (notably, also for much more complicated mutli-component signals) as finally, $A_{z,n}(t) = A(t) = 1$.

For signals in which amplitude modulation and phase modulation occur simultaneously, a meaningful demodulation is possible if the spectra of amplitude $\mathcal{F}_A(\omega)$ and phase $\mathcal{F}_\phi(\omega)$ are well separated. In that case an amplitude demodulation prior to (I)HTE prevents the excitation of spurious oscillatory modes in the Hilbert transform:

$$A_z(t) = |z|(t) = \sqrt{A^2(t)\cos(\phi(t)) + A^2(t)(\hat{H}[\cos(\phi)])^2(t)} = A(t) \; .$$

In this equation the separation of the product under the Hilbert transform is possible due to the Bedrosian identity Eq. (3.10) (see also App. A.4). Then, the identity $\hat{H}[\cos(\phi)](t) = \sin(\phi(t))$ for generic phases can be ensured by means of IHTE (see Sec. 4.2). Thus, an amplitude $A_z(t)$ might be used to extract[3] a distorted and approximate isochronic coupling between $\psi(t)$ and $A_z(t)$.

The ultimate frontier for phase demodulation is constituted by all signals in which an amplitude modulation of $A(t)$ is fast compared to the phase modulation. In all these cases, mixing of phase and amplitude modulations is also observed. However, this mixing is *essential* in the sense that it arises due to true modulations of the amplitude.

For example, given the analytic protophase phase $\theta^{(a)}(t)$, the corrected form of the protophase approximation Eq. (6.1) for a signal $X(t) = S(\varphi) + \delta S(\varphi, \delta\mathbf{y})$ Eq. (3.11) is

$$\begin{aligned} \theta^{(a)}(t) = \arg[z](t) = \arctan\left[\frac{Y(t)}{X(t)}\right] &\approx \arg[S(t) + i\hat{H}[S](t)] \\ + \varepsilon\frac{\hat{H}[\dot{S}q](t)S(t) - \dot{S}q(t)\hat{H}[S](t)}{S^2(t) + (\hat{H}[S])^2(t)} &+ \varepsilon\frac{\hat{H}[\delta S](t)S(t) - \hat{H}[S](t)\delta S(t)}{S^2(t) + \hat{H}[S]^2(t)} \; . \end{aligned} \tag{7.3}$$

This result shows that perturbations of the signal amplitude and the phase modulation both contribute in $\mathcal{O}(\varepsilon)$ to the protophase approximation if the Hilbert transform is

---

[3] The construction of an isochronic coupling for generic embeddings constitutes a heavily numerical task in itself. Further discussion can be found in [112, 185].

used. Moreover, since the amplitude of the measurement – and thus, the deviation δS – relate to the phase dynamics by an unknown isochronic coupling, the amplitude contribution to the phase error STD_n^{ψ} Eq. (5.3) can be much larger than the first two perturbative terms. These terms resemble the protophase operator, convergent under Hilbert iterations while the last term prevents full convergence and is related to the AML. Additionally, if instead of amplitude variations, measurement noise is present, it appears that the reconstruction error of phases is at least of the same order as the noise. In both situations, this implies that a theoretic separation of the observed non-stationary signal behaviour is significantly corrupted by a large sensitivity of the Hilbert transform to already small amplitude variations.

One possible strategy to reduce essential demodulation errors indeed, could be an initial amplitude demodulation. Unfortunately, for dynamical systems the spectra of $\varphi(t)$ and $\delta S(\varphi, \delta\mathbf{y})$ to a large extent can reside on the same support (depending on the complexity of isochronic coupling and observation operator) such that an explicit amplitude demodulation prior to phase demodulation yields no significant improvement. In Ch. 6 such a demodulation was performed but with the true amplitude $r(t)$ based on the state space variables. In a data-driven setting, this amplitude is not known either such that normalisation with the possibly erroneous embedding amplitude $A_z(t)$ results in further errors in the phase-reconstruction process.

7.2.3 Extending the Hilbert transform and the phase definition

The essence of the afore discussion is that a signal quadrature $X^{(q)}(t)$ does not suffice to reconstruct the asymptotic phase $\varphi(t)$ from data. Instead, a dynamic quadrature $X_d^{(q)}(t)$ is needed. This quadrature would be defined in such a way that the *dynamic* analytic signal is

$$z_d(t) = A_d(\mathbf{r}(t), \varphi(t)) \exp(\varphi(t)) = X(t) + iX_d^{(q)}(t) \ ,$$

where $\mathbf{r}(t)$ is the true amplitude and $\varphi(t)$ is the true asymptotic phase of the dynamical system. The construction of such a function from geometric techniques is an open problem. Presumably, it is one of the most challenging problems of data analysis. First, due to the theoretic demands and second, due to the still existent shortcomings of IHTE.

Where should the information of an amplitude dependence enter the IHTE-DPT procedure? For example, an amplitude dependence could be incorporated in a generalised protophase-to-phase transformation: Instead of using $\dot{\varphi}(t) = \omega$ in a derivation, it might be possible to achieve an improvement based on a first-order model $\dot{\varphi} = \omega + \varepsilon q(\varphi, A_z(t))$. It is currently unclear if such pursuit could be successful.

Alternatively, the embedding amplitude $A_{z;n}(t)$ could enter in each iterative step. This strategy is presumably more natural. For example, it could be beneficial to introduce a correction function $\xi_n(t)$ that changes the Hilbert convolution slightly. Then, instead of $\hat{H}[X](\theta_n)$, the transformation $\hat{H}[\xi X](\theta_n)$ is performed. Where, to achieve a simultaneous demodulation of amplitude and phase, proper constraints are needed. For example, for $X_{\mathrm{mono}}(t) = A(t)\cos(\phi(t))$, the (final) correction function is $\xi(t) = 1/A(t)$. Parallel to the amplitude separation, a correction to the protophase is needed: $\theta_n(t, A_z) = \theta_n(t) + \Psi_\theta(A_z)$. How to construct such corrections – and in particular, how to balance their different influences on demodulation –for the (iterated) Hilbert transform is not known.

Moreover, one could use the IHTE-DPT procedure to find optimal phase and amplitude $A_{z,n^\star}(t)$ and $\psi_{n^\star}(t)$ in accordance with the condition Eqs. (3.18), (3.19). Then, the obtained functions could be subsequently used in a method for numerical construction of isochrones. Presumably, all of these approaches will have to incorporate further information such as the phase of an external input $\eta(t)$ (e. g. Sec. 5.2.2), the external input $\varepsilon p(t)$ (if it is known at all) or/and further assumptions about the phase-amplitude dynamics.

Global phase description in chaotic systems by means of IHTE phases?

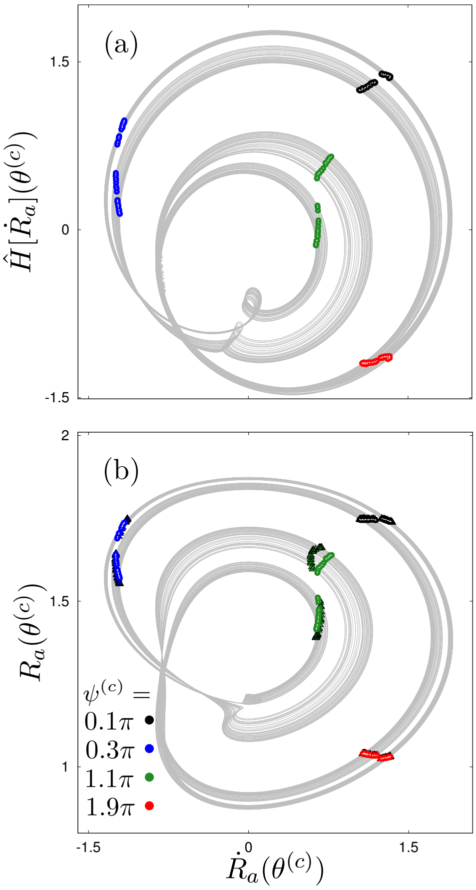

For chaotic systems, a weak phase description is possible by means of isophases. Isophases are defined as stroboscopic sets of states $\mathbf{y}_T(t)$ with return time $T = 2\pi/(\theta(t_m) - \theta(t_0))$. Since all $\mathbf{y}_T(t)$ are situated on the attractor an inherent phase-amplitude description is needed here. Moreover, due to phase diffusion, the set of points $\{\mathbf{y}_T((\tilde{t}/(2\pi) + k)T), k \in \mathbb{N}\}_{\tilde{t}\in\mathbb{R}}$ will gradually scatter with each new return. Thus, optimal isophases are constructed by fitting of a global parametrisation to the stroboscopic sets [186, 185]. Alternatively, augmented IHTE could be flexible enough to define $\{\mathbf{y}_T(t(\psi) + kT), k \in \mathbb{N}\}_{\psi\in\mathbb{R}}$ based on Hilbert phases ψ. As an example, shown in (a) is the IHTE in step ten for $\dot{R}_a(t)$ of the kidney oscillator Eq. (1.2). Main parameters are $c = 4.2$, $T_t = 4.5$s and $d = 0.11$. Panel (b) depicts the state space projection to the plane $(\dot{R}_a, R_a)$. Data points of similar Hilbert phases $\psi_1^{(c)}(t)$ (black-coloured triangles) and $\psi_{10}^{(c)}(t)$ (white-coloured circles) indicate that IHTE indeed cause minor change in the stroboscopic sets.

7.3 Hilbert transforms in practice

There exist various ways to transfer information over vast distances. Most importantly, radio communication and optical signals [19, 187]. In either situation one is confronted with the fact that signals have to be band-limited as otherwise, a receiver is unable to reconstruct the signal content. Here, the IHTE-DPT transformation might be used in a computer-assisted setting to increase the information content in communication signals. However, the numerical evaluation of the integral Eq. (4.8) might be to slow[4], if a real-time demodulation is needed.

An alternative way to construct the IHTE employs the spectral definition Eq. (3.9) for the time-Hilbert transform:

---

[4] The computation time of the integral scales $\sim ((t_m - t_0)/dt)^2$

- Given a (phase-modulated) signal $X(t)$, the Hilbert transform $\hat{H}[X](t)$ is found from the inverse Fourier transform using a standardised fast Fourier-transform implementation (FFT).
- Then, a protophase approximation $\theta_1^{(a,b,c,d)}(t)$ is calculated from the analytic signal $z(t)$ by means of a method exemplified in Sec. 4.1.2.
- The obtained protowaveform $X(\theta_1)$ is sampled unevenly. To apply again the FFT-based Hilbert transform on $X(\theta_1)$, the data has to be re-sampled to a uniform grid. (This step implements the main idea of IHTE, which is rescaling of time.)
- In the next step, $\theta_2(\theta_1)$ is calculated from the embedding of $X(\theta_1)$. Subsequent steps will lead to mutual demodulation.

The advantage of this implementation is the usage of an optimised and readily available fast Fourier tranform.

In present devices, an all-optic (or all-electronic) construction of the analytic signal is achieved by filtering and splitting of a received signal into two components which are phase-shifted relative to each other by $-\pi/2$. Such a device explores the definition of a band-limited quadrature such that an interesting future topic for experimental research would be the realisation of a physical IHTE transformer [171, 188, 187]. Needed for such a realisation is an optical or electric device with response $1/(\pi t)$. Unfortunately, a device with such a characteristics can be realised only approximately due to limitation in the size of a device and precision errors. Moreover, its realisation would still rely on a digital phase calculation and re-sampling of the original data. Will it anyhow be possible to pave the way towards a new demodulation device?

7.4 Further questions

The idea of iterations that leads to the IHTE constitutes a solution for a decade-long standing problem in phase demodulation and the advanced approaches of length-based protophase estimation – presented here in a condensed form – provides additional opportunities for researchers with high interest in accurate and meaningful phase estimation.

However, phase-reduction theory and phase-demodulation fit together only under rather specific assumptions. Certainly, it depends on the purpose how accurate a phase and an amplitude should be estimated from a signal. Moreover, it depends on the type of problem, how to estimate amplitude(s) and phase(s) from a signal at all.

Nevertheless, several questions arise from the presented work to which further efforts could be dedicated:

- How to disentangle phase modulations $q(t)$ and amplitude modulations $\tilde{A}(t)$ if the amplitude spectrum and the phase-modulation spectrum overlap, i.e. if the Bedrosian identity is not satisfied? This question involves an extended spectral convergence analysis of the IHTE transformation. **(physics, mathematics)**
- An answer to the first question leads to a general construction rule for mutual signal quadratures $X^{(q)}(t)$. How to construct the dynamic quadrature $X_d^{(q)}(t)$ to retrieve $\varphi(t)$ from embeddings of observations? **(physics, mathematics)**
- How accurate is an IHTE-based network reconstruction compared to direct reconstruction? **(phyics, mathematics)**

- An evaluation of IHTE in widespread research application and in combination with other methods is needed as there exists no absolute criterion for its success. **(physics, engineering, chemistry, biology, biomedical research)**
- An optimisation of the numerical IHTE integration could potentially be achieved by high-performance programming. **(computer science)**
- The Hilbert transform arises in the theory of analytic functions. Can one rigorously proof the mechanism introduced here for IHTE? What is the most generic functional space on which convergence of IHTE is guaranteed? **(mathematics)**

The high-order phase reduction provided in this text motivates further exploration of high-order coupling effects:

- Based on the phase model Egs. (2.21) - (2.23) or the derived coupling modes App. A.5 – What are the synchronisation properties of an auxiliary network given by the derived coupling modes? **(physics/mathematics)**
- What is the exact parameter dependence of coupling constants in the VdP (or even ML) triplet? **(physics/mathematics)**
- Is it possible to realise further experiments in which the predicted triplet couplings can be observed (e. g. using lasers, mechanical oscillators or in vitro neurons)? **(physics, engineering, chemistry, biology, biomedical research)**

Bibliography

[1] K. Popper, *Alles Leben ist Problemlösen.* No. 2, PIEPER, 2012.

[2] V. Hösle, *Philospohie der ökologischen Krise.* No. 2, Verlag C.H.Beck, München, 1994.

[3] V. Hösle, *Die Krise der Gegenwart und die Verantwortung der Philosophie.* Verlag C.H.Beck, München, 1997.

[4] A. Zwahr, *Der Brockhaus in drei Bänden.* F.A.Brockhaus, Leipzig, Mannheim, 2005.

[5] M. Esfeld, *Philosophie der Physik.* No. 2, Surkamp Taschenbuch Wissenschaft, 2012.

[6] J. Kepler, "Mysterium cosmographicum (tübingen, 1596)," *translated by AM Duncan The Secret of the Universe*, pp. 63–64, 1981.

[7] C. Huygens and C. H. Zulichemii, "F. horologium oscillatorium sive de motu pendulorum ad horologia aptato demonstrationes geometricae," *Apud F. Muguet, Paris, France*, 1673.

[8] A. Pikovsky, J. Kurths, M. Rosenblum, and J. Kurths, *Synchronization: a universal concept in nonlinear sciences*, vol. 12. Cambridge university press, 2003.

[9] N. DeClaris, "Prof. Dr. Balthasar Van der Pol–In Memoriam," *IRE Transactions on Circuit Theory*, vol. 7, no. 4, pp. 360–361, 1960.

[10] B. van der Pol, "Lxxxviii. on relaxation-oscillations," *The London, Edinburgh, and Dublin Philosophical Magazine and Journal of Science*, vol. 2, no. 11, pp. 978–992, 1926.

[11] M. Rosenblum and A. Pikovsky, "Synchronization: from pendulum clocks to chaotic lasers and chemical oscillators," *Contemporary Physics*, vol. 44, no. 5, pp. 401–416, 2003.

[12] S. H. Strogatz, D. M. Abrams, A. McRobie, B. Eckhardt, and E. Ott, "Crowd synchrony on the millennium bridge," *Nature*, vol. 438, no. 7064, pp. 43–44, 2005.

[13] M. J. Mercier, N. B. Garnier, and T. Dauxois, "Reflection and diffraction of internal waves analyzed with the hilbert transform," *Physics of Fluids*, vol. 20, no. 8, p. 086601, 2008.

[14] H. Taher, S. Olmi, and E. Schöll, "Enhancing power grid synchronization and stability through time-delayed feedback control," *Physical Review E*, vol. 100, no. 6, p. 062306, 2019.

[15] M. Wickramasinghe and I. Z. Kiss, "Synchronization of electrochemical oscillators with differential coupling," *Physical Review E*, vol. 88, no. 6, p. 062911, 2013.

[16] K. A. Blaha, A. Pikovsky, M. Rosenblum, M. T. Clark, C. G. Rusin, and J. L. Hudson, "Reconstruction of two-dimensional phase dynamics from experiments on coupled oscillators," *Physical Review E*, vol. 84, no. 4, p. 046201, 2011.

[17] I. Ashraf, R. Godoy-Diana, J. Halloy, B. Collignon, and B. Thiria, "Synchronization and collective swimming patterns in fish (hemigrammus bleheri)," *Journal of the Royal Society Interface*, vol. 13, no. 123, p. 20160734, 2016.

[18] A. Tyrrell, G. Auer, and C. Bettstetter, "Fireflies as role models for synchronization in ad hoc networks," in *2006 1st Bio-Inspired Models of Network, Information and Computing Systems*, pp. 1–7, IEEE, 2006.

[19] R. Ludwig and J. Taylor, "Descanso design and performance summary series article 4: Voyager telecommunications," *Washington: NASA*, pp. 1–6, 2002.

[20] W. Moon and J. S. Wettlaufer, "Coupling functions in climate," *Philosophical Transactions of the Royal Society A*, vol. 377, no. 2160, p. 20190006, 2019.

[21] A. Lupo, W. Kininmonth, J. Armstrong, and K. Green, "Global climate models and their limitations," *Climate change reconsidered II: Physical science*, vol. 9, p. 148, 2013.

[22] D. Gerten, W. Lucht, S. Ostberg, J. Heinke, M. Kowarsch, H. Kreft, Z. W. Kundzewicz, J. Rastgooy, R. Warren, and H. J. Schellnhuber, "Asynchronous exposure to global warming: freshwater resources and terrestrial ecosystems," *Environmental Research Letters*, vol. 8, no. 3, p. 034032, 2013.

[23] D. A. Zappalà, M. Barreiro, and C. Masoller, "Uncovering temporal regularity in atmospheric dynamics through Hfilbert phase analysis," *Chaos: An Interdisciplinary Journal of Nonlinear Science*, vol. 29, no. 5, p. 051101, 2019.

[24] J. L. Silverberg, M. Bierbaum, J. P. Sethna, and I. Cohen, "Collective motion of humans in mosh and circle pits at heavy metal concerts," *Physical review letters*, vol. 110, no. 22, p. 228701, 2013.

[25] N. Wessel, C. Ziehmann, J. Kurths, U. Meyerfeldt, A. Schirdewan, and A. Voss, "Short-term forecasting of life-threatening cardiac arrhythmias based on symbolic dynamics and finite-time growth rates," *Physical Review E*, vol. 61, no. 1, p. 733, 2000.

[26] E. Formento, K. Minassian, F. Wagner, J. B. Mignardot, C. G. Le Goff-Mignardot, A. Rowald, J. Bloch, S. Micera, M. Capogrosso, and G. Courtine, "Electrical spinal cord stimulation must preserve proprioception to enable locomotion in humans with spinal cord injury," *Nature neuroscience*, vol. 21, no. 12, pp. 1728–1741, 2018.

[27] J. M. Bronstein, M. Tagliati, R. L. Alterman, A. M. Lozano, J. Volkmann, A. Stefani, F. B. Horak, M. S. Okun, K. D. Foote, P. Krack, *et al.*, "Deep brain stimulation for Parkinson disease: an expert consensus and review of key issues," *Archives of neurology*, vol. 68, no. 2, pp. 165–165, 2011.

[28] J. Engel, T. A. Pedley, and J. Aicardi, *Epilepsy: a comprehensive textbook*, vol. 3. Lippincott Williams & Wilkins, 2008.

[29] M. Rossi, A. Bradbury, A. Magagna, M. Pesce, S. Taddei, and A. Stefanovska, “Investigation of skin vasoreactivity and blood flow oscillations in hypertensive patients: effect of short-term antihypertensive treatment,” *Journal of hypertension*, vol. 29, no. 8, pp. 1569–1576, 2011.

[30] B. Fromy, P. Abraham, C. Bouvet, B. Bouhanick, P. Fressinaud, and J. L. Saumet, “Early decrease of skin blood flow in response to locally applied pressure in diabetic subjects,” *Diabetes*, vol. 51, no. 4, pp. 1214–1217, 2002.

[31] K. Supekar, V. Menon, D. Rubin, M. Musen, and M. D. Greicius, “Network analysis of intrinsic functional brain connectivity in Alzheimer’s disease,” *PLoS Comput Biol*, vol. 4, no. 6, p. e1000100, 2008.

[32] A. Bashan, R. P. Bartsch, J. W. Kantelhardt, S. Havlin, and P. C. Ivanov, “Network physiology reveals relations between network topology and physiological function,” *Nature communications*, vol. 3, no. 1, pp. 1–9, 2012.

[33] P. C. Ivanov and R. P. Bartsch, “Network physiology: mapping interactions between networks of physiologic networks,” in *Networks of Networks: the last Frontier of Complexity*, pp. 203–222, Springer, 2014.

[34] R. P. Bartsch, K. K. Liu, A. Bashan, and P. C. Ivanov, “Network physiology: how organ systems dynamically interact,” *PloS one*, vol. 10, no. 11, p. e0142143, 2015.

[35] H. Reichert, *Neurobiologie.* Georg Thieme Verlag, 2000.

[36] D. A. Drachman, “Do we have brain to spare?,” 2005.

[37] F. Zenke, E. J. Agnes, and W. Gerstner, “Diverse synaptic plasticity mechanisms orchestrated to form and retrieve memories in spiking neural networks,” *Nature communications*, vol. 6, no. 1, pp. 1–13, 2015.

[38] R. C. Cassilhas, S. Tufik, and M. T. de Mello, “Physical exercise, neuroplasticity, spatial learning and memory,” *Cellular and Molecular Life Sciences*, vol. 73, no. 5, pp. 975–983, 2016.

[39] V. Röhr, R. Berner, E. L. Lameu, O. V. Popovych, and S. Yanchuk, “Frequency cluster formation and slow oscillations in neural populations with plasticity,” *PloS one*, vol. 14, no. 11, p. e0225094, 2019.

[40] H. Osterhage and K. Lehnertz, “Nonlinear time series analysis in epilepsy,” *International Journal of Bifurcation and Chaos*, vol. 17, no. 10, pp. 3305–3323, 2007.

[41] N. Tukhlina, M. Rosenblum, A. Pikovsky, and J. Kurths, “Feedback suppression of neural synchrony by vanishing stimulation,” *Physical Review E*, vol. 75, no. 1, p. 011918, 2007.

[42] A. L. Hodgkin and A. F. Huxley, “A quantitative description of membrane current and its application to conduction and excitation in nerve,” *The Journal of physiology*, vol. 117, no. 4, p. 500, 1952.

[43] R. FitzHugh, “Impulses and physiological states in theoretical models of nerve membrane,” *Biophysical journal*, vol. 1, no. 6, p. 445, 1961.

[44] E. M. Izhikevich and J. Moehlis, “Dynamical systems in neuroscience: The geometry of excitability and bursting,” *SIAM review*, vol. 50, no. 2, p. 397, 2008.

[45] G. Werner, “Metastability, criticality and phase transitions in brain and its models,” *Biosystems*, vol. 90, no. 2, pp. 496–508, 2007.

[46] C. Morris and H. Lecar, “Voltage oscillations in the barnacle giant muscle fiber,” *Biophysical journal*, vol. 35, no. 1, pp. 193–213, 1981.

[47] L. A. Annecchino and S. R. Schultz, “Progress in automating patch clamp cellular physiology,” *Brain and Neuroscience Advances*, vol. 2, p. 2398212818776561, 2018.

[48] N. W. Schultheiss, A. A. Prinz, and R. J. Butera, *Phase response curves in neuroscience: theory, experiment, and analysis.* Springer Science & Business Media, 2011.

[49] A. N. Burkitt, “A review of the integrate-and-fire neuron model: I. homogeneous synaptic input,” *Biological cybernetics*, vol. 95, no. 1, pp. 1–19, 2006.

[50] E. M. Izhikevich, “Resonate-and-fire neurons,” *Neural networks*, vol. 14, no. 6-7, pp. 883–894, 2001.

[51] M. M. Halassa and P. G. Haydon, “Integrated brain circuits: astrocytic networks modulate neuronal activity and behavior,” *Annual review of physiology*, vol. 72, pp. 335–355, 2010.

[52] S. Makovkin, A. Kumar, A. Zaikin, S. Jalan, and M. Ivanchenko, “Multiplexing topologies and time scales: The gains and losses of synchrony,” *Physical Review E*, vol. 96, no. 5, p. 052214, 2017.

[53] H. Lassmann, “Multiple sclerosis pathology,” *Cold Spring Harbor perspectives in medicine*, vol. 8, no. 3, p. a028936, 2018.

[54] W. J. Brownlee, T. A. Hardy, F. Fazekas, and D. H. Miller, “Diagnosis of multiple sclerosis: progress and challenges,” *The Lancet*, vol. 389, no. 10076, pp. 1336–1346, 2017.

[55] E. Niedermeyer and F. L. da Silva, *Electroencephalography: basic principles, clinical applications, and related fields.* Lippincott Williams & Wilkins, 2005.

[56] M. Hämäläinen, R. Hari, R. J. Ilmoniemi, J. Knuutila, and O. V. Lounasmaa, “Magnetoencephalography-theory, instrumentation, and applications to noninvasive studies of the working human brain,” *Reviews of modern Physics*, vol. 65, no. 2, p. 413, 1993.

[57] S. A. Huettel, A. W. Song, G. McCarthy, *et al.*, *Functional magnetic resonance imaging*, vol. 1. Sinauer Associates Sunderland, MA, 2004.

[58] M. Teplan *et al.*, “Fundamentals of EEG measurement,” *Measurement science review*, vol. 2, no. 2, pp. 1–11, 2002.

[59] K. Lehnertz, C. Geier, T. Rings, and K. Stahn, "Capturing time-varying brain dynamics," *EPJ Nonlinear Biomedical Physics*, vol. 5, p. 2, 2017.

[60] A. Sanz-Garcia, T. Rings, and K. Lehnertz, "Impact of type of intracranial EEG sensors on link strengths of evolving functional brain networks," *Physiological Measurement*, vol. 39, no. 7, p. 074003, 2018.

[61] D. Fraiman and D. R. Chialvo, "What kind of noise is brain noise: anomalous scaling behavior of the resting brain activity fluctuations," *Frontiers in physiology*, vol. 3, p. 307, 2012.

[62] W. H. Organization *et al.*, "Epilepsy: a public health imperative: summary," tech. rep., World Health Organization, 2019.

[63] F. Mormann, R. G. Andrzejak, C. E. Elger, and K. Lehnertz, "Seizure prediction: the long and winding road," *Brain*, vol. 130, no. 2, pp. 314–333, 2007.

[64] J. F. Téllez-Zenteno, R. Dhar, and S. Wiebe, "Long-term seizure outcomes following epilepsy surgery: a systematic review and meta-analysis," *Brain*, vol. 128, no. 5, pp. 1188–1198, 2005.

[65] M.-T. Horstmann, S. Bialonski, N. Noennig, H. Mai, J. Prusseit, J. Wellmer, H. Hinrichs, and K. Lehnertz, "State dependent properties of epileptic brain networks: Comparative graph–theoretical analyses of simultaneously recorded EEG and MEG," *Clinical Neurophysiology*, vol. 121, no. 2, pp. 172–185, 2010.

[66] P. E. McSharry, L. A. Smith, and L. Tarassenko, "Prediction of epileptic seizures: are nonlinear methods relevant?," *Nature medicine*, vol. 9, no. 3, pp. 241–242, 2003.

[67] L. Kuhlmann, K. Lehnertz, M. P. Richardson, B. Schelter, and H. P. Zaveri, "Seizure prediction-ready for a new era," *Nature Reviews Neurology*, vol. 14, no. 10, pp. 618–630, 2018.

[68] T. Wilkat, T. Rings, and K. Lehnertz, "No evidence for critical slowing down prior to human epileptic seizures," *Chaos: An Interdisciplinary Journal of Nonlinear Science*, vol. 29, no. 9, p. 091104, 2019.

[69] T. Loddenkemper, A. Pan, S. Neme, K. B. Baker, A. R. Rezai, D. S. Dinner, E. B. Montgomery Jr, and H. O. Lüders, "Deep brain stimulation in epilepsy," *Journal of Clinical Neurophysiology*, vol. 18, no. 6, pp. 514–532, 2001.

[70] J.-P. Lachaux, E. Rodriguez, J. Martinerie, and F. J. Varela, "Measuring phase synchrony in brain signals," *Human brain mapping*, vol. 8, no. 4, pp. 194–208, 1999.

[71] O. Faust, U. R. Acharya, H. Adeli, and A. Adeli, "Wavelet-based EEG processing for computer-aided seizure detection and epilepsy diagnosis," *Seizure*, vol. 26, pp. 56–64, 2015.

[72] M. Politis, K. Wu, S. Molloy, P. G. Bain, K. R. Chaudhuri, and P. Piccini, "Parkinson's disease symptoms: the patient's perspective," *Movement Disorders*, vol. 25, no. 11, pp. 1646–1651, 2010.

[73] K. R. Chaudhuri, D. G. Healy, and A. H. Schapira, "Non-motor symptoms of Parkinson's disease: diagnosis and management," *The Lancet Neurology*, vol. 5, no. 3, pp. 235–245, 2006.

[74] O. Rascol, P. Payoux, F. Ory, J. J. Ferreira, C. Brefel-Courbon, and J.-L. Montastruc, "Limitations of current Parkinson's disease therapy," *Annals of Neurology: Official Journal of the American Neurological Association and the Child Neurology Society*, vol. 53, no. S3, pp. S3–S15, 2003.

[75] C. Hammond, H. Bergman, and P. Brown, "Pathological synchronization in Parkinson's disease: networks, models and treatments," *Trends in neurosciences*, vol. 30, no. 7, pp. 357–364, 2007.

[76] O. V. Popovych, B. Lysyansky, M. Rosenblum, A. Pikovsky, and P. A. Tass, "Pulsatile desynchronizing delayed feedback for closed-loop deep brain stimulation," *PloS one*, vol. 12, no. 3, 2017.

[77] A. Eusebio, W. Thevathasan, L. D. Gaynor, A. Pogosyan, E. Bye, T. Foltynie, L. Zrinzo, K. Ashkan, T. Aziz, and P. Brown, "Deep brain stimulation can suppress pathological synchronisation in parkinsonian patients," *Journal of Neurology, Neurosurgery & Psychiatry*, vol. 82, no. 5, pp. 569–573, 2011.

[78] C. Moreau, L. Defebvre, A. Destee, S. Bleuse, F. Clement, J. Blatt, P. Krystkowiak, and D. Devos, "STN-DBS frequency effects on freezing of gait in advanced Parkinson disease," *Neurology*, vol. 71, no. 2, pp. 80–84, 2008.

[79] B. S. Appleby, P. S. Duggan, A. Regenberg, and P. V. Rabins, "Psychiatric and neuropsychiatric adverse events associated with deep brain stimulation: a meta-analysis of ten years' experience," *Movement disorders: official journal of the Movement Disorder Society*, vol. 22, no. 12, pp. 1722–1728, 2007.

[80] J. T. Wright Jr, G. Bakris, T. Greene, L. Y. Agodoa, L. J. Appel, J. Charleston, D. Cheek, J. G. Douglas-Baltimore, J. Gassman, R. Glassock, *et al.*, "Effect of blood pressure lowering and antihypertensive drug class on progression of hypertensive kidney disease: results from the aask trial," *Jama*, vol. 288, no. 19, pp. 2421–2431, 2002.

[81] A. S. Levey and J. Coresh, "Chronic kidney disease," *The lancet*, vol. 379, no. 9811, pp. 165–180, 2012.

[82] Y. Emelianova, A. Kuznetsov, J. Laugesen, E. Mosekilde, and N.-H. Holstein-Rathlou, "Oscillator suppression in the blood flow regulation of interacting, non-identical nephrons," *Journal of Hypertension: Open Access*, vol. 3, no. 3, p. 1000153, 2014.

[83] N.-H. Holstein-Rathlou, K.-P. Yip, O. V. Sosnovtseva, and E. Mosekilde, "Synchronization phenomena in nephron-nephron interaction," *Chaos: An Interdisciplinary Journal of Nonlinear Science*, vol. 11, no. 2, pp. 417–426, 2001.

[84] M. Barfred, E. Mosekilde, and N.-H. Holstein-Rathlou, "Bifurcation analysis of nephron pressure and flow regulation," *Chaos: An Interdisciplinary Journal of Nonlinear Science*, vol. 6, no. 3, pp. 280–287, 1996.

[85] K. S. Jensen, E. Mosekilde, and N.-H. Holstein-Rathlou, "Behaviour in kidney pressure regulation," *Mondes en Developpement*, no. 54–55, pp. 91–109, 1986.

[86] P. Bittihn, *Complex structure and dynamics of the heart.* Springer, 2014.

[87] M. Lambertz and P. Langhorst, “Simultaneous changes of rhythmic organization in brainstem neurons, respiration, cardiovascular system and EEG between 0.05 Hz and 0.5 Hz,” *Journal of the autonomic nervous system*, vol. 68, no. 1-2, pp. 58–77, 1998.

[88] V. Ticcinelli, T. Stankovski, D. Iatsenko, A. Bernjak, A. E. Bradbury, A. R. Gallagher, P. Clarkson, P. V. McClintock, and A. Stefanovska, “Coherence and coupling functions reveal microvascular impairment in treated hypertension,” *Frontiers in physiology*, vol. 8, p. 749, 2017.

[89] J. M. Davidenko, A. V. Pertsov, R. Salomonsz, W. Baxter, and J. Jalife, “Stationary and drifting spiral waves of excitation in isolated cardiac muscle,” *Nature*, vol. 355, no. 6358, pp. 349–351, 1992.

[90] N. Sperelakis, “An electric field mechanism for transmission of excitation between myocardial cells,” 2002.

[91] R. Clayton, O. Bernus, E. Cherry, H. Dierckx, F. H. Fenton, L. Mirabella, A. V. Panfilov, F. B. Sachse, G. Seemann, and H. Zhang, “Models of cardiac tissue electrophysiology: progress, challenges and open questions,” *Progress in biophysics and molecular biology*, vol. 104, no. 1-3, pp. 22–48, 2011.

[92] R. Barrio, S. Coombes, M. Desroches, F. Fenton, S. Luther, and E. Pueyo, “Excitable dynamics in neural and cardiac systems,” *Communications in Nonlinear Science and Numerical Simulation*, 2020.

[93] J. E. Hall, *Guyton and Hall Textbook of Medical Physiology, Jordanian Edition E-Book*. Elsevier, 2016.

[94] V. Kappadan, S. Telele, I. Uzelac, F. Fenton, U. Parlitz, S. Luther, and J. Christoph, “High-resolution optical measurement of cardiac restitution, contraction, and fibrillation dynamics in beating vs. blebbistatin-uncoupled isolated rabbit hearts,” *Frontiers in Physiology*, vol. 11, 2020.

[95] M. G. Khan, *Rapid ECG interpretation*. Springer Science & Business Media, 2008.

[96] A. Schlemmer, T. Baig, S. Luther, and U. Parlitz, “Detection and characterization of intermittent complexity variations in cardiac arrhythmia,” *Physiological measurement*, vol. 38, no. 8, p. 1561, 2017.

[97] A. Schlemmer, S. Berg, T. Lilienkamp, S. Luther, and U. Parlitz, “Spatiotemporal permutation entropy as a measure for complexity of cardiac arrhythmia,” *Frontiers in Physics*, vol. 6, p. 39, 2018.

[98] B. Kralemann, M. Frühwirth, A. Pikovsky, M. Rosenblum, T. Kenner, J. Schaefer, and M. Moser, “In vivo cardiac phase response curve elucidates human respiratory heart rate variability,” *Nature communications*, vol. 4, no. 1, pp. 1–9, 2013.

[99] T. Stankovski, S. Petkoski, J. Raeder, A. F. Smith, P. V. McClintock, and A. Stefanovska, “Alterations in the coupling functions between cortical and cardio-respiratory oscillations due to anaesthesia with propofol and sevoflurane,” *Philosophical Transactions of the Royal Society A: Mathematical, Physical and Engineering Sciences*, vol. 374, no. 2067, p. 20150186, 2016.

[100] G. G. Berntson, J. T. Cacioppo, and K. S. Quigley, “Respiratory sinus arrhythmia: autonomic origins, physiological mechanisms, and psychophysiological implications,” *Psychophysiology*, vol. 30, no. 2, pp. 183–196, 1993.

[101] G. E. Billman, “Heart rate variability–a historical perspective,” *Frontiers in physiology*, vol. 2, p. 86, 2011.

[102] T. S. Lugovaya, “Biometric human identification based on ECG,” *PhysioNet*, 2005.

[103] T. B. Garcia, *12-lead ECG: The art of interpretation*. Jones & Bartlett Publishers, 2013.

[104] P. Gregory, S. Lodge, T. Kilner, and S. Paget, “Accuracy of ECG chest electrode placements by paramedics; an observational study,” *medRxiv*, p. 19001321, 2019.

[105] S. Zaunseder, A. Trumpp, D. Wedekind, and H. Malberg, “Cardiovascular assessment by imaging photoplethysmography–a review,” *Biomedical Engineering/Biomedizinische Technik*, vol. 63, no. 5, pp. 617–634, 2018.

[106] M. Li, W. Xiong, and Y. Li, “Wearable measurement of ECG signals based on smart clothing,” *International Journal of Telemedicine and Applications*, vol. 2020, 2020.

[107] Z. Chen, P. Venkat, D. Seyfried, M. Chopp, T. Yan, and J. Chen, “Brain–heart interaction: cardiac complications after stroke,” *Circulation research*, vol. 121, no. 4, pp. 451–468, 2017.

[108] S. Sahoo, P. Biswal, T. Das, and S. Sabut, “De-noising of ECG signal and QRS detection using Hilbert transform and adaptive thresholding,” *Procedia Technology*, vol. 25, pp. 68–75, 2016.

[109] K. Li, H. Rüdiger, and T. Ziemssen, “Spectral analysis of heart rate variability: time window matters,” *Frontiers in neurology*, vol. 10, p. 545, 2019.

[110] Ç. Topçu, M. Frühwirth, M. Moser, M. Rosenblum, and A. Pikovsky, “Disentangling respiratory sinus arrhythmia in heart rate variability records,” *Physiological measurement*, vol. 39, no. 5, p. 054002, 2018.

[111] V. I. Smirnov, “Biography of A.M. Lyapunov,” *International journal of control*, vol. 55, no. 3, pp. 775–784, 1992.

[112] R. Cestnik, *Inferring oscillatory dynamics from data*. PhD thesis, Vrije Universiteit Amsterdam, 2020.

[113] J. H. Argyris, G. Faust, M. Haase, and R. Friedrich, *An exploration of dynamical systems and chaos: completely revised and enlarged second edition*. Springer, 2015.

[114] I. Mezić, “Spectrum of the Koopman operator, spectral expansions in functional spaces, and state-space geometry,” *Journal of Nonlinear Science*, pp. 1–55, 2019.

[115] S. Shirasaka, W. Kurebayashi, and H. Nakao, “Phase-amplitude reduction of transient dynamics far from attractors for limit-cycling systems,” *Chaos: An Interdisciplinary Journal of Nonlinear Science*, vol. 27, no. 2, p. 023119, 2017.

[116] A. Mauroy and I. Mezić, “Global computation of phase-amplitude reduction for limit-cycle dynamics,” *Chaos: An Interdisciplinary Journal of Nonlinear Science*, vol. 28, no. 7, p. 073108, 2018.

[117] D. Wilson and J. Moehlis, “Isostable reduction of periodic orbits,” *Physical Review E*, vol. 94, no. 5, p. 052213, 2016.

[118] P. M. Morse, “Bernard Osgood Koopman, 1900–1981,” *Operations Research*, vol. 30, no. 3, pp. 417–427, 1982.

[119] D. Wilson, “A data-driven phase and isostable reduced modeling framework for oscillatory dynamical systems,” *Chaos: An Interdisciplinary Journal of Nonlinear Science*, vol. 30, no. 1, p. 013121, 2020.

[120] Y. Kuramoto, *Chemical oscillations, waves, and turbulence.* Courier Corporation, 2003.

[121] H. Daido, “Order function and macroscopic mutual entrainment in uniformly coupled limit-cycle oscillators,” *Progress of theoretical physics*, vol. 88, no. 6, pp. 1213–1218, 1992.

[122] G. Thut, C. Miniussi, and J. Gross, “The functional importance of rhythmic activity in the brain,” *Current Biology*, vol. 22, no. 16, pp. R658–R663, 2012.

[123] J. M. Beggs and D. Plenz, “Neuronal avalanches in neocortical circuits,” *Journal of neuroscience*, vol. 23, no. 35, pp. 11167–11177, 2003.

[124] J. A. Roberts, L. L. Gollo, R. G. Abeysuriya, G. Roberts, P. B. Mitchell, M. W. Woolrich, and M. Breakspear, “Metastable brain waves,” *Nature communications*, vol. 10, no. 1, pp. 1–17, 2019.

[125] S. Majhi, B. K. Bera, D. Ghosh, and M. Perc, “Chimera states in neuronal networks: A review,” *Physics of life reviews*, vol. 28, pp. 100–121, 2019.

[126] L. Ramlow, J. Sawicki, A. Zakharova, J. Hlinka, J. C. Claussen, and E. Schöll, “Partial synchronization in empirical brain networks as a model for unihemispheric sleep,” *EPL (Europhysics Letters)*, vol. 126, no. 5, p. 50007, 2019.

[127] F. Peter, C. C. Gong, and A. Pikovsky, “Microscopic correlations in the finite-size kuramoto model of coupled oscillators,” *Physical Review E*, vol. 100, no. 3, p. 032210, 2019.

[128] C. H. Coulam, D. M. Bouley, and F. G. Sommer, “Measurement of renal volumes with contrast-enhanced MRI,” *Journal of Magnetic Resonance Imaging: An Official Journal of the International Society for Magnetic Resonance in Medicine*, vol. 15, no. 2, pp. 174–179, 2002.

[129] D. J. Marsh, O. V. Sosnovtseva, E. Mosekilde, and N.-H. Holstein-Rathlou, “Vascular coupling induces synchronization, quasiperiodicity, and chaos in a nephron tree,” *Chaos: An Interdisciplinary Journal of Nonlinear Science*, vol. 17, no. 1, p. 015114, 2007.

[130] D. Postnov, D. Postnov, D. Marsh, N.-H. Holstein-Rathlou, and O. Sosnovtseva, “Dynamics of nephron-vascular network,” *Bulletin of mathematical biology*, vol. 74, no. 12, pp. 2820–2841, 2012.

[131] M. Rosenblum and A. Pikovsky, “Self-organized quasiperiodicity in oscillator ensembles with global nonlinear coupling,” *Physical review letters*, vol. 98, no. 6, p. 064101, 2007.

[132] H. Krantz and T. Schreiber, “Nonlinear time series analysis, 1997.”

[133] T. Sauer, J. A. Yorke, and M. Casdagli, “Embedology,” *Journal of statistical Physics*, vol. 65, no. 3-4, pp. 579–616, 1991.

[134] A. Pikovsky, “Reconstruction of a neural network from a time series of firing rates,” *Physical Review E*, vol. 93, no. 6, p. 062313, 2016.

[135] A. Pikovsky, “Reconstruction of a scalar voltage-based neural field network from observed time series,” *EPL (Europhysics Letters)*, vol. 119, no. 3, p. 30004, 2017.

[136] N. Polyzotis, M. Zinkevich, S. Roy, E. Breck, and S. Whang, “Data validation for machine learning,” *Proceedings of Machine Learning and Systems*, vol. 1, pp. 334–347, 2019.

[137] C. Letellier, L. A. Aguirre, and J. Maquet, “Relation between observability and differential embeddings for nonlinear dynamics,” *Physical Review E*, vol. 71, no. 6, p. 066213, 2005.

[138] M. Feldman, *Hilbert transform applications in mechanical vibration.* John Wiley & Sons, 2011.

[139] M. Rosenblum and R. Cestnik, “Inferring the phase response curve from observation of a continuously perturbed oscillator,” *Scientific reports*, vol. 8, no. 1, pp. 1–10, 2018.

[140] R. Hegger and H. Kantz, “Improved false nearest neighbor method to detect determinism in time series data,” *Physical Review E*, vol. 60, no. 4, p. 4970, 1999.

[141] H. Broer and S. van Strien, “In memoriam, Floris Takens 1940–2010,” 2011.

[142] F. Takens, “Detecting strange attractors in turbulence,” in *Dynamical systems and turbulence, Warwick 1980*, pp. 366–381, Springer, 1981.

[143] H. D. Abarbanel, R. Brown, J. J. Sidorowich, and L. S. Tsimring, “The analysis of observed chaotic data in physical systems,” *Reviews of modern physics*, vol. 65, no. 4, p. 1331, 1993.

[144] O. V. Sosnovtseva, A. N. Pavlov, E. Mosekilde, K.-P. Yip, N.-H. Holstein-Rathlou, and D. J. Marsh, “Synchronization among mechanisms of renal autoregulation is reduced in hypertensive rats,” *American Journal of Physiology-Renal Physiology*, vol. 293, no. 5, pp. F1545–F1555, 2007.

[145] A. R. Brazhe, D. J. Marsh, N.-H. Holstein-Rathlou, and O. Sosnovtseva, “Synchronized renal blood flow dynamics mapped with wavelet analysis of laser speckle flowmetry data,” *PloS one*, vol. 9, no. 9, 2014.

[146] D. J. Marsh, A. S. Wexler, A. Brazhe, D. E. Postnov, O. V. Sosnovtseva, and N.-H. Holstein-Rathlou, “Multinephron dynamics on the renal vascular network,” *American Journal of Physiology-Renal Physiology*, vol. 304, no. 1, pp. F88–F102, 2013.

[147] A. Roulet and C. Bruder, “Quantum synchronization and entanglement generation,” *Physical review letters*, vol. 121, no. 6, p. 063601, 2018.

[148] M. G. Rosenblum, L. Cimponeriu, A. Bezerianos, A. Patzak, and R. Mrowka, “Identification of coupling direction: application to cardiorespiratory interaction,” *Physical Review E*, vol. 65, no. 4, p. 041909, 2002.

[149] H. Osterhage, F. Mormann, T. Wagner, and K. Lehnertz, “Measuring the directionality of coupling: phase versus state space dynamics and application to EEG time series,” *International journal of neural systems*, vol. 17, no. 03, pp. 139–148, 2007.

[150] M. Paluš and A. Stefanovska, “Direction of coupling from phases of interacting oscillators: an information-theoretic approach,” *Physical Review E*, vol. 67, no. 5, p. 055201, 2003.

[151] D. Chicharro and R. G. Andrzejak, “Reliable detection of directional couplings using rank statistics,” *Physical Review E*, vol. 80, no. 2, p. 026217, 2009.

[152] J. M. L. Lew D. Landau, *Mechanik.* No. 1, Verlag Harri Deutch, 1997.

[153] L. Neuhäuser, A. Mellor, and R. Lambiotte, “Multibody interactions and nonlinear consensus dynamics on networked systems,” *Physical Review E*, vol. 101, no. 3, p. 032310, 2020.

[154] M. Komarov and A. Pikovsky, “Finite-size-induced transitions to synchrony in oscillator ensembles with nonlinear global coupling,” *Physical Review E*, vol. 92, no. 2, p. 020901, 2015.

[155] C. C. Gong and A. Pikovsky, “Low-dimensional dynamics for higher-order harmonic, globally coupled phase-oscillator ensembles,” *Physical Review E*, vol. 100, no. 6, p. 062210, 2019.

[156] M. Rosenblum and A. Pikovsky, “Efficient determination of synchronization domains from observations of asynchronous dynamics,” *Chaos: An Interdisciplinary Journal of Nonlinear Science*, vol. 28, no. 10, p. 106301, 2018.

[157] B. Kralemann, A. Pikovsky, and M. Rosenblum, “Reconstructing phase dynamics of oscillator networks,” *Chaos: An Interdisciplinary Journal of Nonlinear Science*, vol. 21, no. 2, p. 025104, 2011.

[158] B. Kralemann, A. Pikovsky, and M. Rosenblum, “Detecting triplet locking by triplet synchronization indices,” *Physical Review E*, vol. 87, no. 5, p. 052904, 2013.

[159] B. Kralemann, A. Pikovsky, and M. Rosenblum, “Reconstructing effective phase connectivity of oscillator networks from observations,” *New Journal of Physics*, vol. 16, no. 8, p. 085013, 2014.

[160] H. Bauer, “Eberhard hopf 17.4.1902 – 24.7.1983,” *Jahrbuch*, pp. 254 – 256, 1984.

[161] E. Gengel and A. Pikovsky, “Phase demodulation with iterative Hilbert transform embeddings,” *Signal Processing*, vol. 165, pp. 115–127, 2019.

[162] S. Strogatz, “Arthur Taylor Winfree,” *Physics Today*, vol. 56, no. 6, pp. 74–74, 2003.

[163] M. Rosenblum and A. Pikovsky, “Nonlinear phase coupling functions: a numerical study,” *Philosophical Transactions of the Royal Society A*, vol. 377, no. 2160, p. 20190093, 2019.

[164] M. Le Van Quyen, J. Foucher, J.-P. Lachaux, E. Rodriguez, A. Lutz, J. Martinerie, and F. J. Varela, “Comparison of Hilbert transform and wavelet methods for the analysis of neuronal synchrony,” *Journal of neuroscience methods*, vol. 111, no. 2, pp. 83–98, 2001.

[165] N. E. Huang, M.-L. Wu, W. Qu, S. R. Long, and S. S. Shen, “Applications of Hilbert-Huang transform to non-stationary financial time series analysis,” *Applied stochastic models in business and industry*, vol. 19, no. 3, pp. 245–268, 2003.

[166] B. Kralemann, L. Cimponeriu, M. Rosenblum, A. Pikovsky, and R. Mrowka, “Phase dynamics of coupled oscillators reconstructed from data,” *Physical Review E*, vol. 77, no. 6, p. 066205, 2008.

[167] N. E. Huang and Z. Wu, “A review on Hilbert-Huang transform: Method and its applications to geophysical studies,” *Reviews of geophysics*, vol. 46, no. 2, 2008.

[168] Y.-L. Tseng, P.-Y. Ko, and F.-S. Jaw, “Detection of the third and fourth heart sounds using Hilbert-huang transform,” *Biomedical engineering online*, vol. 11, no. 1, p. 8, 2012.

[169] E. Bedrosian, “A product theorem for Hilbert transforms,” *Rand Memorandum*, 1962.

[170] E. Bedrosian, “The analytic signal representation of modulated waveforms,” *Proceedings of the IRE*, vol. 50, no. 10, pp. 2071–2076, 1962.

[171] D. Vakman, “On the analytic signal, the teager-kaiser energy algorithm, and other methods for defining amplitude and frequency,” *IEEE Transactions on signal processing*, vol. 44, no. 4, pp. 791–797, 1996.

[172] F. Bahmed, F. Khatoon, B. R. Reddy, and F. Bahmed, “Relation between respiratory rate and heart rate–a comparative study,” *Indian J. Clin. Anat. Physiol*, vol. 3, pp. 436–9, 2016.

[173] W. H. Press, S. A. Teukolsky, W. T. Vetterling, and B. P. Flannery, *Numerical recipes 3rd edition: The art of scientific computing.* Cambridge university press, 2007.

[174] A. Savitzky and M. J. Golay, “Smoothing and differentiation of data by simplified least squares procedures.,” *Analytical chemistry*, vol. 36, no. 8, pp. 1627–1639, 1964.

[175] A. S. Pikovsky and J. Kurths, “Coherence resonance in a noise-driven excitable system,” *Physical Review Letters*, vol. 78, no. 5, p. 775, 1997.

[176] S. M. Wieczorek, “Noise synchronisation and stochastic bifurcations in lasers,” *Nonlinear Laser Dynamics: From Quantum Dots to Cryptography*, 2011.

[177] H. Kramers, "Levenbericht L.S. Ornstein," *Jaarboek, Amsterdam*, pp. 225–231, 1940.

[178] E. G. D. Cohen, "George E. Uhlenbeck and statistical mechanics," *American Journal of Physics*, vol. 58, no. 7, pp. 619–625, 1990.

[179] G. E. Uhlenbeck and L. S. Ornstein, "On the theory of the Brownian motion," *Physical review*, vol. 36, no. 5, p. 823, 1930.

[180] R. W. Schafer, "On the frequency-domain properties of Savitzky-Golay filters," in *2011 Digital Signal Processing and Signal Processing Education Meeting (DSP/SPE)*, pp. 54–59, IEEE, 2011.

[181] D. Lachance-Quirion, S. Tremblay, S. A. Lamarre, V. Methot, D. Gingras, J. Camirand Lemyre, M. Pioro-Ladriere, and C. N. Allen, "Telegraphic noise in transport through colloidal quantum dots," *Nano letters*, vol. 14, no. 2, pp. 882–887, 2014.

[182] A. Di Crescenzo, B. Martinucci, and S. Zacks, "Telegraph process with elastic boundary at the origin," *Methodology and Computing in Applied Probability*, vol. 20, no. 1, pp. 333–352, 2018.

[183] M. Kac, "A stochastic model related to the telegrapher's equation," *The Rocky Mountain Journal of Mathematics*, vol. 4, no. 3, pp. 497–509, 1974.

[184] S. R. Soekadar, C. Arfeller, A. Rilk, S. K. Plontke, and C. Plewnia, "Theta burst stimulation in the treatment of incapacitating tinnitus accompanied by severe depression," *CNS Spectr*, vol. 14, no. 4, pp. 208–211, 2009.

[185] J. T. Schwabedal and A. Pikovsky, "Phase description of stochastic oscillations," *Physical review letters*, vol. 110, no. 20, p. 204102, 2013.

[186] J. T. Schwabedal, A. Pikovsky, B. Kralemann, and M. Rosenblum, "Optimal phase description of chaotic oscillators," *Physical Review E*, vol. 85, no. 2, p. 026216, 2012.

[187] L. Li, L. Xu, L. Zhang, Y. Duan, Y. Li, N. Yang, C. Zhang, and X. Zhang, "Real-time optical vector network analyzer based on coherent time-stretch," in *2020 Conference on Lasers and Electro-Optics (CLEO)*, pp. 1–2, IEEE, 2020.

[188] H. Emami, N. Sarkhosh, L. A. Bui, and A. Mitchell, "Amplitude independent RF instantaneous frequency measurement system using photonic Hilbert transform," *Optics express*, vol. 16, no. 18, pp. 13707–13712, 2008.

[189] H. Kitajima and J. Kurths, "Forced synchronization in morris-lecar neurons," *International Journal of Bifurcation and Chaos*, vol. 17, no. 10, pp. 3523–3528, 2007.

[190] M. Hénon, "On the numerical computation of Poincaré maps," 1982.

Appendix A

Technical details

A.1 Morris-Lecar neuron

The different membrane compartments considered in Eq. (1.1) approach certain steady-state values depending on the ambient potential $V(t)$. For the ML dynamics, it is assumed that the Ca^{2+} gating approaches its equilibrium activation $M_\infty(V)$ instantaneously. In contrast the slower K^+ gating relaxes towards $W_\infty(V)$. Moreover, the relaxation constant $\lambda_w(V)$ for the slow gating shows a global minimum at a certain voltage. All three gating functions possess a stereotypical shape modelled by

$$X_\infty(V) = \frac{1}{2}\left(1 + \tanh\left(\frac{V - V_{1,3}}{V_{2,4}}\right)\right) \qquad \lambda_w(V) = \frac{1}{\tau_g}\cosh\left(\frac{V - V_3}{V_4}\right) . \tag{A.1}$$

Here $X_\infty = [M, W]_\infty(V)$. The actual shape of these characteristic functions represents the molecular dynamics of gating which is immersed in the ever fluctuating neuronal environment. Thus, the involved parameters actually depend on temperature ϑ. This is the reason why in Sec. 7.1 τ_g is varied. The parameters used in the simulations are listed in table A.1. The models are stimulated with a baseline current of $I_0 = 50$ mA.

$C = 20\ \mu$ F/cm^2	$g_L = 2$ mS/cm^2	$g_K = 8$ mS/cm^2	$g_{Ca} = 4$ mS/cm^2
$V_1 = -1.2$ mV	$V_2 = 18$ mV	$V_3 = 12\ \ (2)$ mV	$V_4 = 17.4$ mV
$E_L = -60$ mV	$E_K = -80$ mV	$E_{Ca} = 120$ mV	$\tau_g = 15$ s

Table A.1: List of modelling parameters for the ML neuron Eq. (1.1). C is the membrane capacity, $g_{L,K;Ca}$ are the conductivities of leakage, K^+ and Ca^{2+} ion channels, $V_{1,2,3,4}$ are empiric parameters for the channel activation, $E_{L,K,Ca}$ are the respective equilibrium potentials of leakage, K^+ and Ca^{2+} channels and τ_g is the relaxation time of gating. Parameters are adapted from [189]. Values for V_3 result in type I (type II) oscillations.

A.2 Nephron oscillator

The nephron dynamics introduced in Sec. 1.1.2 involves 16 empirical parameters listed in table A.2. The dynamics of the nephron depends on the glomerular pressure P_g which follows from solution of the implicit equation

$$0 = C_e(P_g, P_t)(P_v - P_g) + \frac{R_e}{R_a}(P_a - P_g)[C_e(P_g, P_t) + (1 - H_a)(C_e(P_g, P_t) - C_a))] .$$

This equation depends on the protein concentration in the efferent blood:

$$C_e(P_g, P_t) = \left(\sqrt{a^2 + 4b(P_g - P_t)} - a\right)/(2b) .$$

For a solution, P_g is found by bisection. The Filtration activity of a nephron is determined by

$$F_g(P_g, P_t, R_a) = \frac{P_a - P_g}{R_a}(1 - H_a)\left(1 - \frac{C_a}{C_e(P_g, P_t)}\right) .$$

The stiffness of the arteriola walls is modelled by a potential

$$K(R_a) = [7(R_a/R_{a,0} - 1.25)/5]^8 + 1 .$$

The TGF response that is exerted on the arteriola muscle cells is modelled by

$$\begin{aligned} \mathrm{TGF}(\chi_3) =& \mathrm{TGF}_{\mathrm{max}} - \frac{\mathrm{TGF}_{\mathrm{max}} - \mathrm{TGF}_{\mathrm{min}}}{1 + \exp[c((\chi_3 - P_d)/(R_{h,0}F_{h,0}) - S)]} \\ S =& 1 - \log[(1 - \mathrm{TGF}_{\mathrm{min}})/(\mathrm{TGF}_{\mathrm{max}} - 1)]/c \end{aligned} \tag{A.2}$$

$P_a = 13.33$ kPa	$C_a = 54$ g/l	$H_a = 0.5$	$a = 21,73$ Pa·l/g
$P_v = 1.33$ kPa	$C_{\mathrm{tub}} = 0.4$	$F_{h,0} = 0.2$	$b = 0.38$ Pa· $\mathrm{l}^2/\mathrm{g}^2$
$P_d = 6$ kPa	$\mathrm{TGF}_{\mathrm{max}} = 1.5$	$\mathrm{TGF}_{\mathrm{min}} = 0.75$	$R_h = 5.33$ kPa· s/nl
$R_{a,0} = 24.39$ kPa· s/nl	$\omega_a = 0.22$ s^{-1}	$F_{\mathrm{reab}} = 0.3$ nl/s	$R_e = 0.25$ kPa ·s/nl

Table A.2: List of modelling parameters for the nephron model in Sec. 1.1.2. $P_{a,v}$ are the blood pressures in the afferent and efferent arteriole. P_d is the urine pressure in the distal tubule. $R_{a,0}$ and R_e are the normal resistivity of the afferent and resistivity of the efferent arteriole. R_h is the resistivity of the loop of Henle. C_a and C_{tub} are the compliances of the afferent arteriole and of the tubule. ω_a is the frequency for resistivity oscillations. H_a is the afferent hematocrit ratio of the blood. F_{reab} is the reabsorption rate of urine in the tubule and $F_{h,0}$ is a normalisation value for the flow in the loop of Henle. $\mathrm{TGF}_{\mathrm{max,min}}$ determine the range of the TGF response in the afferent arteriole.

Additionally, a relaxation time of $T_t = 4.5$ s is used in this monograph. Similarly to the control parameter c, it influences the complexity of the attractor. The relaxation constant $d = 0.11$ is chosen such that a chaotic dynamics is possible.

A.3 Determination of the phase response curve

For an unperturbed system, the phase after m periods is $2\pi m$ while for perturbed systems, the relaxation to the cycle causes a phase response potentially integrating up over several periods. Thus, the cumulative phase response after perturbation is $2\pi m - \varphi(\tilde{T})$, where $\tilde{T}$ is the time needed to complete m periods. Namely, after a first perturbed period, T_1, the next periods are of length $T_2, ...T_m$, where T_m is nearly the same as T. Thus to determine the *cumulative* iPRC, in accordance with Eq. (1.6) one calculates

$$Z(\varphi) := \frac{2\pi m - \varphi(\tilde{T})}{\varepsilon} = \frac{2\pi}{\varepsilon}\left(m - \frac{1}{T}\sum_{k=1}^{m} T_k\right) = \int_t^{t+\tilde{T}} \Phi'[\mathbf{y}(\tau)] \cdot \mathbf{p}(\tau) d\tau . \tag{A.3}$$

For a numerical determination, periods T and T_k have to be calculated for which standard methods exist [190].

A.4 Bedrosians identity and demodulation

The quadrature of $X_{\text{mono}}(t) = A(t)\cos(\phi(t))$ is given by $X^{(q)}_{\text{mono}}(t) = A(t)\sin(\phi(t)) = A(t)\cos(\phi(t) - \pi/2)$ since this allows to construct the mutual continuation of $X_{\text{mono}}(t)$ into the complex plane. If however, neither $A(t)$ nor $\phi(t)$ are known[1] it is necessary to construct an approximation of $X^{(q)}_{\text{mono}}(t)$ from the Hilbert transform $\hat{H}[X_{\text{mono}}](t)$. The discrepancy between quadrature and Hilbert transform can be understood by an expansion in the small parameter ε:

$$\begin{aligned} X^{(q)}_{\text{mono}}(t) =& A_0\sin(t) + \varepsilon\Big[\tilde{A}(t)\sin(t) + A_0 q(t)\cos(t)\Big] + \frac{\varepsilon^2}{2}\Big[2\tilde{A}(t)q(t)\cos(t) - A_0 q^2(t)\sin(t)\Big] \\ & -\frac{\varepsilon^3}{6}\Big[A_0 q^3(t)\cos(t) + 3\tilde{A}(t)q^2(t)\sin(t)\Big] + \mathcal{O}(\varepsilon^4) \end{aligned} \tag{A.4}$$

On the contrary application of the Hilbert transformation and expansion in terms of ε yields

$$\begin{aligned} \hat{H}[A\cos(\phi)](t) =& A_0\hat{H}[\cos](t) + \varepsilon\hat{H}[\tilde{A}\cos - A_0 q\sin](t) \\ & -\frac{\varepsilon^2}{2}\hat{H}[A_0 q^2\cos + 2\tilde{A}q\sin](t) \\ & +\frac{\varepsilon^3}{6}\hat{H}[A_0 q^3\sin - 3\tilde{A}q^2\cos](t) + \mathcal{O}(\varepsilon^4)\ . \end{aligned} \tag{A.5}$$

From comparison of Eq. (A.4) and (A.5) it follows that in leading order, the Hilbert transform is equivalent to the quadrature even if $X_{\text{mono}}(t)$ is non-stationary. However, for higher order corrections – i.e. for congruence of both functions in all details – certain conditions

ε^1: $\mathcal{F}_{\tilde{A}}(\omega) + \mathcal{F}_q(\omega) = 0$ if $|\omega| > C$

ε^2: $\Big[\mathcal{F}_q * \mathcal{F}_q\Big](\omega) + \Big[\mathcal{F}_{\tilde{A}} * \mathcal{F}_q\Big](\omega) = 0$ if $|\omega| > C$

ε^3: $\Big[\mathcal{F}_q * \mathcal{F}_q * \mathcal{F}_q\Big](\omega) + \Big[\mathcal{F}_{\tilde{A}} * \mathcal{F}_q * \mathcal{F}_q\Big](\omega) = 0$ if $|\omega| > C$

ε^4: $\dots$

must be satisfied: If $q(t)$ and $\tilde{A}(t)$ obey a simple narrowband condition, the Hilbert transform approximates the quadrature with accuracy $\sim \varepsilon$. Second order and presumably all higher orders of reconstruction demand for even stricter conditions on the original modulation spectra as further convolutions broaden the resultant spectrum in each derived condition. Ultimately, this leads to the conclusion that the assertion[2] $\hat{H}[X](t) = X^{(q)}(t)$ is only valid if the phase modulation vanishes and if narrowband amplitude modulations are present. In the upper quadrature conditions, C is a function of the true instantaneous frequency $\dot{\phi}(t)$.

---

[1] It is $A(t) = A_0 + \varepsilon\tilde{A}(t)$, $\phi(t) = t + \varepsilon q(t)$.

[2] This property is also called *harmonic correspondence* [171].

A.5 Coupling modes and coupling constants

Here, the resulting coefficients for $\dot{\varphi}$, Eqs. (2.21-2.23) are listed. In tables A.3, A.4 and A.5 the following notation is used:

$$C_{m,k} = \frac{1+\alpha^2}{2}\frac{2c_{m,k}}{4+(\omega_m-\omega_k)^2}, \qquad D_{m,k} = \frac{1+\alpha^2}{2}\frac{(\omega_m-\omega_k)c_{m,k}}{4+(\omega_m-\omega_k)^2}\ .$$

$a^{(2)}_{1;0,0,0}$	$c_{2,1}\Big(C_{1,2}\sin(\beta_{1,2}+\beta_{2,1}) - D_{1,2}\cos(\beta_{1,2}+\beta_{2,1}) - D_{2,1}\Big)$
$a^{(2)}_{1;-2,2,0}$	$c_{2,1}\Big(C_{1,2}\sin(\beta_{2,1}-\beta_{1,2}) + D_{1,2}\cos(\beta_{2,1}-\beta_{1,2})$ $-C_{2,1}\sin(2\beta_{2,1}) + D_{2,1}\cos(2\beta_{2,1})\Big)$
$b^{(2)}_{1;-2,2,0}$	$c_{2,1}\Big(C_{1,2}\cos(\beta_{2,1}-\beta_{1,2}) - D_{1,2}\sin(\beta_{2,1}-\beta_{1,2})$ $-C_{2,1}\cos(2\beta_{2,1}) - D_{2,1}\sin(2\beta_{2,1})\Big)$
$a^{(2)}_{1;-1,2,-1}$	$c_{2,1}\Big(C_{3,2}\sin(\beta_{2,1}-\beta_{3,2}) + D_{3,2}\cos(\beta_{2,1}-\beta_{3,2})\Big)$
$b^{(2)}_{1;-1,2,-1}$	$c_{2,1}\Big(C_{3,2}\cos(\beta_{2,1}-\beta_{3,2}) - D_{3,2}\sin(\beta_{2,1}-\beta_{3,2})\Big)$
$a^{(2)}_{1;-1,0,1}$	$c_{2,1}\Big(-D_{3,2}\cos(\beta_{2,1}+\beta_{3,2}) + C_{3,2}\sin(\beta_{2,1}+\beta_{3,2})\Big)$
$b^{(2)}_{1;-1,0,1}$	$c_{2,1}\Big(D_{3,2}\sin(\beta_{2,1}+\beta_{3,2}) + C_{3,2}\cos(\beta_{2,1}+\beta_{3,2})\Big)$

Table A.3: Coupling coefficients of the first SL oscillator.

$a^{(2)}_{3;0,0,0}$	$c_{2,3}\Big(C_{3,2}\sin(\beta_{3,2}+\beta_{2,3}) - D_{3,2}\cos(\beta_{3,2}+\beta_{2,3}) - D_{2,3}\Big)$
$a^{(2)}_{3;0,2,-2}$	$c_{2,3}\Big(C_{3,2}\sin(\beta_{2,3}-\beta_{3,2}) + D_{3,2}\cos(\beta_{2,3}-\beta_{3,2})$ $-C_{2,3}\sin(2\beta_{2,3}) + D_{2,3}\cos(2\beta_{2,3})\Big)$
$b^{(2)}_{3;0,2,-2}$	$c_{2,3}\Big(C_{3,2}\cos(\beta_{2,3}-\beta_{3,2}) - D_{3,2}\sin(\beta_{2,3}-\beta_{3,2})$ $-C_{2,3}\cos(2\beta_{2,3}) - D_{2,3}\sin(2\beta_{2,3})\Big)$
$a^{(2)}_{3;-1,2,-1}$	$c_{2,3}\Big(C_{1,2}\sin(\beta_{2,3}-\beta_{1,2}) + D_{1,2}\cos(\beta_{2,3}-\beta_{1,2})\Big)$
$b^{(2)}_{3;-1,2,-1}$	$c_{2,3}\Big(C_{1,2}\cos(\beta_{2,3}-\beta_{1,2}) - D_{1,2}\sin(\beta_{2,3}-\beta_{1,2})\Big)$
$a^{(2)}_{3;1,0,-1}$	$c_{2,3}\Big(-D_{1,2}\cos(\beta_{2,3}+\beta_{1,2}) + C_{1,2}\sin(\beta_{2,3}+\beta_{1,2})\Big)$
$b^{(2)}_{3;1,0,-1}$	$c_{2,3}\Big(D_{1,2}\sin(\beta_{2,3}+\beta_{1,2}) + C_{1,2}\cos(\beta_{2,3}+\beta_{1,2})\Big)$

Table A.4: Coupling coefficients of the third SL oscillator.

$a^{(2)}_{2;0,0,0}$	$\Big(C_{2,1}c_{1,2}\sin(\beta_{2,1}+\beta_{1,2}) - D_{2,1}c_{1,2}\cos(\beta_{2,1}+\beta_{1,2}) - D_{1,2}c_{1,2}$ $+C_{2,3}c_{3,2}\sin(\beta_{3,2}+\beta_{2,3}) - D_{3,2}c_{3,2} - D_{2,3}c_{3,2}\cos(\beta_{3,2}+\beta_{2,3})\Big)$
$a^{(2)}_{2;2,-2,0}$	$\Big(C_{2,1}c_{1,2}\sin(\beta_{1,2}-\beta_{2,1}) + D_{2,1}c_{1,2}\cos(\beta_{1,2}-\beta_{2,1})$ $-C_{1,2}c_{1,2}\sin(2\beta_{1,2}) + D_{1,2}c_{1,2}\cos(2\beta_{1,2})\Big)$
$b^{(2)}_{2;2,-2,0}$	$\Big(C_{2,1}c_{1,2}\cos(\beta_{1,2}-\beta_{2,1}) - D_{2,1}c_{1,2}\sin(\beta_{1,2}-\beta_{2,1})$ $-C_{1,2}c_{1,2}\cos(2\beta_{1,2}) - D_{1,2}c_{1,2}\sin(2\beta_{1,2})\Big)$
$a^{(2)}_{2;0,-2,2}$	$\Big(C_{2,3}c_{3,2}\sin(\beta_{3,2}-\beta_{2,3}) + D_{2,3}c_{3,2}\cos(\beta_{3,2}-\beta_{2,3})$ $-C_{3,2}c_{3,2}\sin(2\beta_{3,2}) + D_{3,2}c_{3,2}\cos(2\beta_{3,2})\Big)$
$b^{(2)}_{2;0,-2,2}$	$\Big(C_{2,3}c_{3,2}\cos(\beta_{3,2}-\beta_{2,3}) - D_{2,3}c_{3,2}\sin(\beta_{3,2}-\beta_{2,3})$ $-C_{3,2}c_{3,2}\cos(2\beta_{3,2}) - D_{3,2}c_{3,2}\sin(2\beta_{3,2})\Big)$
$a^{(2)}_{2;-1,2,-1}$	$\Big(D_{3,2}c_{1,2}\cos(\beta_{1,2}+\beta_{3,2}) - C_{3,2}c_{1,2}\sin(\beta_{1,2}+\beta_{3,2})$ $-C_{1,2}c_{3,2}\sin(\beta_{3,2}+\beta_{1,2}) + D_{1,2}c_{3,2}\cos(\beta_{3,2}+\beta_{1,2})\Big)$
$b^{(2)}_{2;-1,2,-1}$	$\Big(D_{3,2}c_{1,2}\sin(\beta_{1,2}+\beta_{3,2}) + C_{3,2}c_{1,2}\cos(\beta_{1,2}+\beta_{3,2})$ $+C_{1,2}c_{3,2}\cos(\beta_{3,2}+\beta_{1,2}) + D_{1,2}c_{3,2}\sin(\beta_{3,2}+\beta_{1,2})\Big)$
$a^{(2)}_{2;1,0,-1}$	$\Big(-D_{3,2}c_{1,2}\cos(\beta_{1,2}-\beta_{3,2}) - C_{3,2}c_{1,2}\sin(\beta_{1,2}-\beta_{3,2})$ $-C_{1,2}c_{3,2}\sin(\beta_{3,2}-\beta_{1,2}) - D_{1,2}c_{3,2}\cos(\beta_{3,2}-\beta_{1,2})\Big)$
$b^{(2)}_{2;1,0,-1}$	$\Big(D_{3,2}c_{1,2}\sin(\beta_{1,2}-\beta_{3,2}) - C_{3,2}c_{1,2}\cos(\beta_{1,2}-\beta_{3,2})$ $+C_{1,2}c_{3,2}\cos(\beta_{3,2}-\beta_{1,2}) - D_{1,2}c_{3,2}\sin(\beta_{3,2}-\beta_{1,2})\Big)$

Table A.5: Coupling coefficients of the second SL oscillator.

Table A.6 presents the correction hierarchy of coupling modes up to ε^4 for the SL oscillator.

	1 and 3	2 and 4	3	4	5
1	(-1,1,0)	(0,0,0) (-2,2,0) (-1,0,1) (1,-2,1)	(-3,3,0), (0,-1,1) (-1,3,-2), (-2,3,-1) (-1,-1,2), (-2,1,1)	(-4,4,0), (0,-2,2) (-2,0,2), (2,-4,2) (-1,-2,3), (3,-2,-1) (-1,4,-3),(-3,4,-1)	(0,3,-3), (5,-5,0), (4,-3,-1) (2,-5,3), (3,-5,2), (1,3,-4) (3,-1,-2), (2,1,-3) (1,-5,4), (4,-5,1)
2	(1,-1,0) (0,-1,1)	(0,0,0) (2,-2,0) (0,-2,2) (-1,0,1) (1,-2,1)	(-3,3,0), (0,3,-3) (-1,3,-2), (-2,3,-1) (-1,-1,2), (-2,1,1)	(-4,4,0), (0,4,-4) (-2,0,2), (2,-4,2) (-1,-2,3), (3,-2,-1) (-1,4,-3), (-3,4,-1) (2,-5,3), (3,-5,2)	(5,-5,0), (0,5,-5), (2,-5,3) (3,-1,-2), (1,2,-3), (3,-5,2) (1,3,-4), (4,-3,-1) (4,-5,1), (1,-5,4)
3	(0,1,-1)	(0,0,0) (0,2,-2) (1,0,-1) (1,-2,1)	(0,3,-3), (1,-1,0) (-1,3,-2), (-2,3,-1) (-1,-1,2), (-2,1,1)	(0,4,-4), (2,-2,0) (2,0,-2), (2,-4,2) (-1,-2,3), (3,-2,-1) (-1,4,-3), (-3,4,-1)	(3,-3,0), (0,5,-5), (4,-3,-1) (3,-5,2), (2,-5,3), (1,3,-4) (3,-1,-2), (2,1,-3) (1,-5,4), (4,-5,1)

Table A.6: Tabulated are coupling terms that appear in different orders (columns) and for all three oscillators (rows). Terms present up to ε^2 are also found in orders $\varepsilon^{3,4}$ but are not listed.

Osc	ε	ε^2
1	8 modes: (1,-1,0), (1,1,0), (3,-1,0), (3,1,0), (1,3,0), (1,-3,0), (3,-3,0), (3,3,0)	47 modes: (2,-2,0), (2,0,0), (0,2,0), (1,-2,1), (1,2,-1), (1,0,-1), (1,0,1), (2,2,0), (1,-2,-1), (1,2,1), (2,-4,0), (1,-4,1), (1,4,-1), (0,4,0), (4,-2,0), (2,4,0), (3,-2,1), (3,2,-1), (3,-2,-1), (3,0,1), (1,4,1), (3,-4,1), (4,2,0), (4,-4,0), (3,0,-1), (1,-4,-1), (3,-4,-1), (4,0,0), (3,2,1), (3,4,-1), (4,4,0), (1,2,-3), (1,0,-3), (1,-2,3), (3,4,1), (1,0,3), (1,2,3), (1,-2,-3), (3,-2,-3), (3,-4,-3), (3,-2,3), (1,1,-4), (3,0,-3), (1,4,3), (3,2,-3), (1,-4,-3), (3,2,3)
2	15 modes: (0,1,-1), (1,1,0), (0,1,1), (1,-1,0), (3,1,0), (3,-1,0), (0,3,1), (0,1,-3), (0,1,3), (1,3,0), (1,-3,0), (3,-3,0), (0,3,-3), (3,3,0), (0,3,3)	56 modes: (0,2,0), (2,-2,0), (1,-2,1), (0,2,-2), (2,0,0), (1,0,1), (1,0,-1), (1,-2,-1), (0,0,2), (1,2,-1), (1,2,1), (2,2,0), (4,-2,0), (0,2,2), (4,0,0), (4,2,0), (0,2,-4), (3,0,1), (3,0,-1), (0,0,4), (1,-4,1), (1,-2,3), (3,2,-1), (1,2,-3), (1,4,-1), (1,-2,-3), (1,0,-3), (0,4,-2), (0,2,4), (1,-4,-1), (3,-2,1), (2,4,0), (3,-2,-1), (1,-4,3), (0,4,0), (1,4,1), (1,2,3), (1,0,3), (2,-4,0), (3,4,-1), (4,-4,0), (0,4,2), (3,2,1), (3,-4,1), (3,0,-3), (3,-2,-3), (0,4,-4), (4,4,0), (1,4,-3), (3,-2,3), (3,0,3), (1,-4,-3), (0,4,4), (1,4,3), (3,-4,-3), (3,2,3)
3	8 modes: (0,1,1), (0,1,-1), (0,3,1), (0,3,-1), (0,1,3), (0,1,-3), (0,3,-3), (0,3,3)	50 modes: (0,2,-2), (0,0,2), (1,0,-1), (1,0,1), (1,-2,-1), (1,-2,1), (0,2,0), (1,2,1), (1,2,-1), (0,2,2), (0,4,-2), (1,-4,-1) , (1,-4,1), (0,4,0), (1,4,1), (1,4,-1), (0,4,2), (3,-2,-1), (3,-4,-1), (1,0,3), (3,-2,1), (3,-4,1), (1,0,-3), (1,-2,-3), (1,-2,3), (0,2,-4), (1,2,3), (1,-4,3), (1,2,-3), (0,2,4) , (3,2,1), (3,2,-1), (3,0,-1), (0,0,4), (3,0,1), (1,4,-3), (1,-4,-3), (1,4,3), (3,-2,-3), (0,4,-4), (3,4,1), (3,-2,3), (0,4,4), (3,4,-1), (3,-4,3), (3,0,3), (3,2,3), (3,2,-3), (3,0,-3), (3,4,3)

Table A.7: All modes revealed in orders ε and ε^2 for a network of VdP oscillators.

Osc	modes
1	Modes: (0,0,0), (0,j,0), (1,$-j$,0), (1,j,0), (2,-3,0), (2,-2,0), (2,-1,0) (1,0,0), (2,-4,0), (2,0,0), (2,k,0), (3,2,0), (3,-3,0), (3,-2,0), (3,-1,0), (4,-4,0), (3,1,0), *(3,-4,0)*, *(4,-3,0)*, *(4,1,0)*, *(0,2,2)*, *(0,3,1)*, *(1,-2,-2)*
2	(0,0,0), (0,0,j), (0,1,$-j$), (0,1,j), (0,2,j), (j,-1,0), (j,0,0), (j,1,0), (j,2,0), (0,1,0), (0,2,0), (0,3,0), (0,2,-1), (1,-2,0), (0,2,-4), (0,2,-3), (0,2,-2), (2,-2,0), (3,-2,0), (4,-2,0), (0,4,0), *(0,3,-4)*, *(0,3,-3)*, *(0,3,1)*, *(0,3,2)*, *(1,3,0)*, *(2,3,0)*, *(3,-3,0)*, *(3,4,0)*, *(4,-3,0)*
3	(0,0,0), (0,1,-2), (0,j,-1), (0,j,0), (0,j,1), (0,1,2), (0,2,-2), (0,2,2), (2,2,-1), (2,2,0), (0,3,-2), (0,3,2), (0,0,2), (0,4,-2), (0,4,2), (3,2,-1), (2,2,1), (0,1,-3), (0,2,-3), (0,4,-4), **(0,0,1)**, *(0,1,4)*, *(0,3,-4)*, *(0,3,-3)*, *(1,3,-1)*, *(1,3,0)*, *(3,1,-1)*, *(2,3,0)*, *(2,3,-1)*

Table A.8: All modes recovered from the data driven reconstruction for the ML network. $j \in [1, 2, 3, 4]$. Highlighting indicates false-negative occurrence of a mode in step 1, 1+20, **20** and false positive occurrence in step 1, 1+20, *20* of the IHTE phase, compared to the direct reconstruction.

A.6 Source code

iterative Hilbert transform embedding (IHTE)	A `C`-code implementation featuring calculations of phases $\psi^{(a,b,c,d)}(t)$, phase modulations and frequencies from IHTE-DPT transformations as well as estimates for the error measures $\mathrm{Err}_n^{\star,*}$, STD_n^{ψ}
data-based iPRC estimation	A `C`-code implementation of a kernel-density fit for the pairwise phase-coupling function and an implementation of the iterative scheme for reconstruction of the iPRC.
direct construction of iPRC and isochrones	`C`-code implementations of an iPRC construction based on the state-space dynamics and a reconstruction scheme for the isochronic structure. In this method randomly placed initial condition are evolved in the unperturbed system.
effective network reconstruction	A `C`-code implementation of phase-network reconstruction based on Fourier fitting
data generation	A `C`-code implementation of several useful tools for data simulation including Runge-Kutta methods of order 1 to 4 (classical RK4 method) as well as a stochastic Runge-Kutta scheme of order 2 and a direct estimation method for $\varphi(t)$ and $\dot{\varphi}(t)$

Table A.9: Listing of source code related to this text, available at `https://gitlab.com/IUFRGMP/`.

Appendix B

Miscellaneous

The cover picture of the book is an artist representation of several key issue of non-linear dynamics but it also symbolises the power of the human mind to overcome obstacles.

First, the figure shows a projection of the sphere to the plane. This symbolises periodicity and phenomena in phase-based analysis. Second, lines of evolving colour – presumably – never end but continue on and on across the edge of the picture which is one pole of the sphere. In a two-dimensional world however, a trajectory finally has to intersect with itself. In the picture this never happens as there seem to evolve different layers on top of each other such that uniqueness of the flow is guaranteed. This symbolises that the mind finds solutions where no solutions are assumed to exist. Third, the flow develops turbulent vortices that whir into and out of the deep and who carry blue particles with them. Where are they going? This aspect of the figure symbolises deterministic chaos and its sensitivity to small changes in initial conditions. The human mind is attracted to the idea that visual lines ascend from left to right. Thus, the unconscious probably tells that the blue band flows from bottom left to the upper right. However, in this case the two turbulent vortices seem to evolve into the wrong direction. Finally, every reader is invited to interprete separately: What is the meaning of our perception?

Appendix C

Correction remarks

This monograph contains minor changes of the text compared to the initially submitted version. Changes are mainly added for clarity. Below these changes are listed for transparency reasons.

p.3	In Eq. (1.1) the capacity is added while in the initial version normalised quantities are used. This does not touch simulation results for which the listed parameter values are employed correctly.
p.12	The Floquet multiplier $\Lambda_k = \exp(\lambda_k T)$ is an eigenvalue of $\mathbf{D}(T)$. In the first version it is mentioned that it is an eigenvalue of $\mathbf{D}(mT)$. In fact, this operator has eigenvalue $\exp(m\lambda_k T)$.
p.24	The *largest* non-vanishing functional interaction scales as ε^2. In the first version it is written *smallest*.
p.39	In footnote no. 4, using the spectrum of real signals $\mathcal{F}_X(\omega)$, in fact leads to vanishing odd moments. This was not clearly written in the initial text.
p.51	In the iterative scheme the step *Phase estimate* mentions the mapping $\psi_{n+1} = \Theta^{-1}(\theta_{n+1})$. In the previous version, the inversion was not mentioned, indicating a slightly different definition of the protophase-to-phase mapping.
p.77	Columns two ($n = 1$), three ($n = 15$) and four ($n = 15$) in figure 6.9 show results for DPT (black) and FPT (red). In the initial version it is mentioned that column two shows results only for DPT and results for FPT are shown in column three. Moreover, in the original versions, the residue of instantaneous frequencies is shown while in fact the difference of phases is depicted.
p.79	In Eq. (7.1) The capacity is added similar to p.3
p.81	The observed true perturbation according to the expansion mentioned in the text is $\hat{M}'[\mathbf{y}^{(0)}]\delta\mathbf{y}(t)$. In the initial version it is denoted by $\hat{M}'[\delta\mathbf{y}(t)]$